INTERNATIONAL ATOMIC ENERGY AGENCY
UNITED NATIONS EDUCATIONAL SCIENTIFIC AND CULTURAL ORGANIZATION

INTERNATIONAL CENTRE FOR THEORETICAL PHYSICS
34100 TRIESTE (ITALY) - P.O.B. 586 - MIRAMARE - STRADA COSTIERA 11 - TELEPHONES: 224*1/2/3/4/5/6
CABLE: CENTRATOM - TELEX 460392-1

SMR/115 - 33

WINTER COLLEGE ON LASERS, ATOMIC AND MOLECULAR PHYSICS

(21 January - 22 March 1985)

Topical Meeting on the Free Electron Laser

THE LELA EXPERIMENT

Description of the LELA Experiment
(S. SOLIMENO)

Characterization of High Reflectivity Mirrors
(M.R. MASULLO)

Nonlinear Optical Problems in Free Electron Lasers
(A. CUTOLO)

S. SOLIMENO
Istituto Nazionale di Fisica Nucleare
Sezione di Napoli
Mostra d'Oltremare, Pad. 20
80125 Napoli
Italy

A Reprint from the

PROCEEDINGS

SPIE Volume 453

Free-Electron Generators of Coherent Radiation

26 June-1 July 1983
Rosario Resort, Orcas Island, Washington

Gain measurement and optimization of the energy extraction from the electrons of the Frascati-ADONE FEL

M. Biagini, R. Boni, S. De Simone, S. Guiducci, M. Preger, M. Serio, S. Tazzari, F. Tazzioli, S. Trillo, M. Vescovi
I.N.F.N., Laboratori Nazionali di Frascati

M. Ambrosio, G. C. Barbarino, M. Castellano, N. Cavallo, F. Cevenini, M. R. Masullo, P. Patteri, R. Rinzivillo, S. Solimeno
I.N.F.N., Sezione di Napoli and Istituto di Fisica Sperimentale, Napoli

Gain measurement and optimization of the energy extraction from the electrons of the Frascati-ADONE FEL

M. Biagini, R. Boni, S. De Simone, S. Guiducci, M. Preger,
M. Serio, S. Tazzari, F. Tazzioli, S. Trillo, M. Vescovi

I.N.F.N., Laboratori Nazionali di Frascati

M. Ambrosio, G.C. Barbarino, M. Castellano, N. Cavallo,
F. Cevenini, M.R. Masullo, P. Patteri, R. Rinzivillo,
S. Solimeno

I.N.F.N., Sezione di Napoli and Istituto di Fisica Sperimentale, Napoli

Abstract

Recent results on optical gain measurements on the ADONE FEL are reported and discussed. In addition, the results of a computer analysis of the Rayleigh length which optimizes the extraction of energy from the ADONE beam are discussed together their implications on the configuration of the optical cavity to be used for the FEL oscillator. These simulations have been based on a suitable extension of the Madey's theorem and on a representation of the electron work against the field of a gaussian beam by means of the far field radiated by the single electron. In turn, the accuracy of the calculated far field has been tested by comparison with the measured patterns of the spontaneous radiation.

Introduction

In the years since Madey and co-workers developed the first free-electron laser, experiments have been set-up in some laboratories[1] to investigate the operation of a FEL in a storage ring used as electron source. These experiments have now made considerable progress. Recently, the laser built on the ACO storage ring has oscillated for half an hour[2], thus proving the feasibility of devices exhibiting a gain as low as $6 \cdot 10^{-4}$. The experiment in preparation at Frascati on the ADONE ring differs from the Orsay-Stanford one for the larger size of the electron machine and the higher energy of the beam. Both these factors imply the use of a long optical cavity (17 m), the remote control of the system and the acquisition of data via a remotely located computer. While these characteristics encumber the Frascati FEL with a heavier load of technical requirements, it will be possible to extend the analysis of the mechanisms which would be determining the evolution of the optical field inside the resonator. In addition, it will be easy to scan the ultraviolet region of the spectrum with the fundamental of the spontaneous radiation, thus making possible the accurate testing of the mirrors for a better understanding of the UV damage mechanisms.

After the installation of the 20 period undulator and the preliminary measurement of the gain reported at the Bendor conference[3], an accurate analysis of the maximum gain which can be achieved with the ADONE ring has been carried out during the last few months. In the meanwhile, the cavity radiofrequency of the ring has been elevated to 51.4 MHz, thus allowing the circulation of electron bunches as short as a few hundred picoseconds. In addition, the chromatism of the ring in correspondence of the undulator has been eliminated. As a consequence of these steps a peak gain of $2.4 \cdot 10^{-3}$ has been measured, which contrasts with the initially reported value of 10^{-3} (see ref. 3).

In the near future an optical cavity will be installed by using as design parameter the condition that the Rayleigh length of the fundamental mode should be close to one- half the undulator length. This criterion has emerged from a computer analysis of the optimal gain for an e-beam having assigned cross-section and divergence, and replaces the generally accepted condition of maximizing the filling factor of a gaussian beam.

The experimental apparatus

The Frascati-ADONE FEL uses a storage ring as a source of electron (see Figure 1). The 20 period undulator[4], with two half poles for correcting the electron trajectory, is a normal electromagnet, having a factor $K = \frac{e}{2\pi mc^2} B\lambda = 3.412$ and a period of 11.6 cm, designed for generating a radiation of 5145 Å with a beam energy of 625 MeV. In its present configuration the electromagnet operates as a uniform undulator; however, it can be rewired for being transformed into a two-stage optical klystron.

An evacuated optical channel has been built by prolongating on both sides the straight section of the ring vessel passing through the undulator. This channel is ∿ 18 m long and

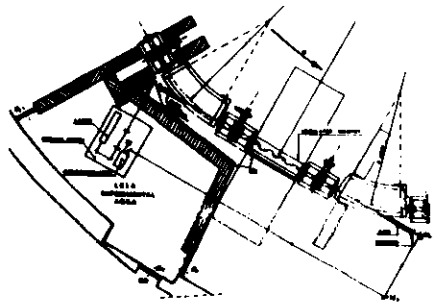

Figure 1. Layout of the FEL section of the ADONE ring and the gain measurement system.

terminates with two quartz windows allowing the passage of the spontaneous radiation and the argon laser beam used for measuring the gain.

Beside the optical channel it has been arranged a radiation-safe room containing the Ar laser and the detection system. The data are transmitted via a voltage-to-frequency converter to a computer located outside the storage ring hall.

New ADONE lattice and measurement of the electron bunch length

In order to increase the laser gain the beam optics of the ring has been modified together with the radio frequency, which has been increased from 8.66 MHz to 51.4 MHz (180 kV) by installing a new RF cavity. The new parameters of the ADONE lattice are collected in Table I. In particular, the e-beam chromatism in correspondence of the undulator central section has been eliminated by reducing to zero the off-energy function. This improvement has been obtained by doubling the number of independent quadrupole families. In addition, the momentum compaction (variation of the orbit length with the energy) has been reduced to 0.014. The new radial betatron wavelength has a minimum at the undulator center and the associated Twiss coefficients α and γ are respectively equal to 0 and 0.5 m^{-1}. The radial envelope corresponds to an emittance $\varepsilon_x = 2\pi\sigma_x^2/\beta = 3.4 \cdot 10^{-4}$ mm mrad, while the divergence is equal to $\sigma'_x = \varepsilon_x \times (2\pi\sigma_x)^{-1} = 0.17$ mrad.

Table I . Old and new ADONE latticem

	Old electron optics	New optics
Radial betatron tune ν_x	3.2	5.25
Vertical betatron tune ν_z	3.15	3.1
Off-energy function η (m)	2	0
Momentum compaction α_c	0.064	0.014
Betatron wavelength β_x (m)	9	2.1
Radial beam envelope σ_x (mm)	1.18	0.37
Vertical beam envelope σ_z (mm) †	0.23	0.21

† 0.1 coupling factor between vertical and radial betatron oscillations

It is noteworthy that the e-beam divergence obtained with the new optics is much less than the angular width (∿0.6 mrad) of the spontaneous radiation pattern emitted by the undulator. Consequently, the non-homogeneous broadening of the gain line-width due to the divergence can be neglected. This property has been verified by calculating numerically the standard deviations of the radiation pattern.

With the new radio frequency electron bunches as short as 300 psec have been obtained.

The pulsewidth has been measured with a fast vacuum photodiode (ITL-TF 1850) having a rise time of 100 psec. A digital oscilloscope with a sampling head has been used for recording and averaging several bunch waveshapes. By measuring the bunch lengths for different values of the ring current, the Chao-Gareyte scaling law[6,7] with exponent 1/3 has been verified,

$$\sigma_y \text{ (ns)} = 1.38\ \xi^{1/3} \qquad (1)$$

where

$$\xi = \frac{2\pi i}{heV\cos\phi} \quad \text{(mA/kV)} \qquad (2)$$

(see Figure 2). In Eq.(2) V = 180 kV is the RF cavity voltage, i is the bunch current and

$$\phi = \arctan\frac{\alpha_c W}{\nu_s \theta} \qquad (3)$$

being W=energy deviation of a particle, ν_s=single particle synchrotron frequency/revolution frequency, θ=longitudinal coordinate of a particle in radians. With negligible error $\cos\phi$ can be put equal to unity. Finally, h is the harmonic number of the RF system (h=3 for 8.56 MHz and h= 18 for 51.4 MHz).

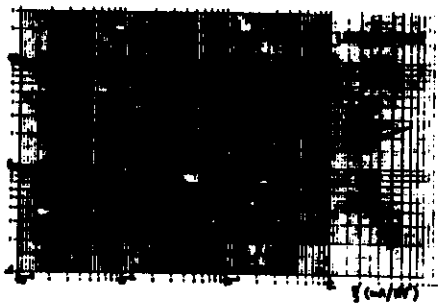

Figure 2. Experimental plot of the bunch length vs. ξ

Gain measurement

The experimental apparatus has been illustrated elsewhere[1]. It consists of a linear polarized CW argon laser operating at 5145 Å, which emits a beam propagating along the FEL active region and is focused to a waist w_0 = 0.35 mm located in the center of the undulator. The radiation emerging from the optical channel is focused onto the entrance slit of a monochromator which rejects most of spontaneous radiation. The gain is observed through a fast photodiode coupled to a resonant active load, which transforms the radiation filtered by the monochromator into an RF signal which is, in turn, amplified (30 dB) and, then, downconverted by mixing it with the ADONE RF frequency. The low frequency signal is filtered at 900 Hz with a pass-band filter and sent to an EG&G-PAR mod. 5206 lock-in amplifier slaved to a chopper placed in front of the argon laser and working at a frequency of 933 Hz. In this way the signal provided by the lock-in is practically free of the spontaneous radiation contribution.

For measuring an average gain of 10^{-8} with a signal-to-noise ratio unity, it has been necessary to get rid of the fluctuations of the laser beam intensity. This result has been achieved by dividing the lock-in output by a signal derived from a voltage divider in the photodiode supplier circuit, which is proportional to the incoming laser power.

In the preliminary gain measurements a solid state photodiode (PND 100 EG&G) was chosen in view of its high sensitivity. Unfortunately, it was observedthat the heavy loading produced by the spontaneous radiation, induced an intermodulation which reduced notably the noise figure of the detection apparatus. Successively, the solid-state photodiode has been replaced by a vacuum photodiode (ITL-TF 1850) having a rise-time of 100 ps, a sensitivity of 0.3 μA/mW at 5145 Å and equipped with a UV window. In the present condition the detection system introduces a noise equivalent to an average gain of 10^{-8}.

The gain has been measured by collecting the signals relative to the two lock-ins, the ring current and the electron energy with a data logger interfaced withe HP9825 computer. Four typical gain curves are plotted in Figure 3. Figures 3a to 3c represent the measured gain versus the electron energy for ring currents of 25, 8 and 13 mA respectively. The relative pulse lengths derived from Figure 2, are equal to 1.3, 0.36 and 0.40 ns respectively. Consequently, the peak gain averaged over the transverse area of the laser beam is equal to $2\cdot10^{-4}$, $2.4\cdot10^{-4}$ and $2.22\cdot10^{-4}$ for the three cases respectively. It is noteworthy that a gain of $2.4\cdot10^{-4}$ has been obtained with a current of only 8 mA, while an analogous gain was measured on the ACO FEL with a much higher current (~50 mA)(see ref. 7, table 6). This fact benefits the UV damage of the mirrors.

Figure 3d refers to the third harmonic measured by reducing the energy to 180 MeV. The relative parameters are: current = 10 mA, pulse length = 1 ns, average gain = $4.5\cdot10^{-7}$, peak gain = $6.7\cdot10^{-5}$.

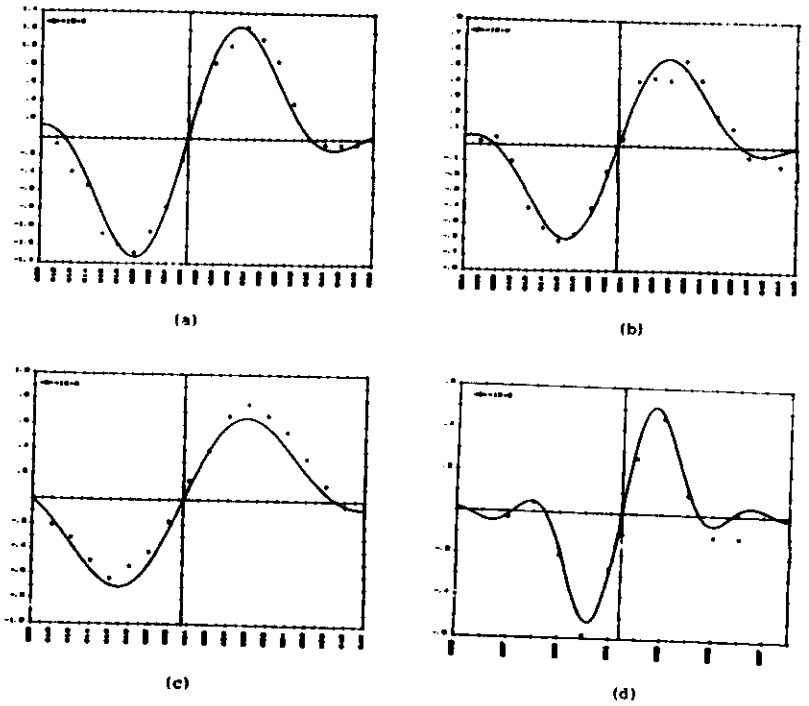

Figure 3 Gain vs. energy for the Frascati-ADONE FEL

Flux of UV radiation hitting the cavity mirrors

Due to the large value of K, the spontaneous radiation spectrum is extremely rich in harmonics. Consequently, it is expected that the damage of the mirrors due to the UV radiation will be one of the major problems with the FEL cavity. Accordingly, it is worth comparing the photon fluxes relative to the harmonics radiated by the Frascati undulator with those of the Orsay-Stanford FEL. For a mean distance of 8 m from the cavity mirrors to the center of the ADONE undulator, the formulae of ref. 1 (see also ref. 7) give = photon flux per unit surface and unit circulating current equal respectively to:

I_1(fundamental) = $10^8\ \gamma^2$ photons/sec/cm^2/mA ,

I_3(third harmonic) = $7\cdot10^7\ \gamma^2$ photons/sec/cm^2/mA ,

I_5(fifth harmonic) = $5.6\cdot10^7\ \gamma^2$ photons/sec/cm^2/mA .

For γ = 1127 (corresponding to the wavelength of 6328 A^o used at ACO), I_1+I_5 = $1.6\cdot10^{14}$ (photons/sec/cm^2/mA), while for the ACO undulator working at the same freqdency with K=2.2, $I_3+I_5 \simeq 5\cdot10^{14}$ (see ref. 7, Figure 24). On the other hand, the ring current circulating through the ACO ring is almost five times the current used in ADONE for obtaining the same gain of $\sim 10^{-4}$ (see ref. 7, table 6 and above section of this paper). Consequently, it seems reasonable to expect for the mirrors which will be installed on the Frascati FEL the same order of magnitude of UV radiation measured on ACO.

Small-signal gain for a gaussian beam

The gain of a FEL active medium depends in general on the spatial and temporal characteristics of the laser beam and the electron bunches. In particular, the growth of the laser pulses bouncing back and forth in an optical cavity and interacting with a series of micro and macro pulses has been analyzed recently by several authors (see f.i. refs. 8-13). The mode structures of FEL stable and unstable oscillators have also been analyzed[14].

The problem of the extraction of energy from an e-beam for an incident gaussian beam has been initially addressed by Colson and Ellaume by using the Colson-Gapanov-Miller pendulum model. They have observed a shift of the resonance parameter to a higher value when the relative value z_R/L_w of the rayleigh length z_R with respect to the undulator length L_w decreases from infinity (plane wave) to zero (spherical wave). For a filamentary e-beam they have found that the gain of a uniform undulator peaks for $L_w = 3\ z_R$. For thicker e-beams the gain peaks for larger values of z_R/L_w, thus implying that thicker e-beams work better in laser beams having a larger waist.

When the analysis is limited to the small-signal gain the equation of motion of the electrons can be solved perturbatively by using as a smallness parameter the laser beam amplitude. To this end it is worth using a Hamiltonian description of the motion, as originally pointed out by Vinokurov[15]. The main advantage of this approach lies in the possibility of relating the spectral intensity of the spontaneous radiation to the stimulated one. In addition, it becomes very simple to relate the second order variation of the electron energy to the first order one, as shown in ref. 16.

In ref. 17 it is shown that

$$\langle \gamma^{(2)} \rangle = \frac{\partial}{\partial \gamma^{(1)}} \langle \gamma^{(1)2} \rangle + \langle \underline{p}_t^{(1)} \frac{\partial \gamma^{(1)}}{\partial \underline{p}_t^{(1)}} \rangle \quad , \tag{4}$$

where $\langle \ldots \rangle$ denotes the average with respect to the phase of the electron measured with respect to the gaussian beam at the undulator entrance. $\gamma^{(1)}$ and $\gamma^{(2)}$ are the first and second order variations (with respect to the laser field amplitude) of the electron energy. Note the presence of the second term on the RHS of Eq.(4), which is missing from the Madey's theorem: in fact, this term marks the difference with the plane wave case, since in the latter case the energy is independent of the transverse momentum $\underline{p}_t$. However, it can be shown[17] that the above term is negligible when $(z_R/L_w)^2 \times \underline{t}^2 \rangle / \lambda L_w$, $\underline{t}$ being the transverse displacement of the electron. Since this condition is fulfilled for most practical cases, except for laser beams with large angular divergence, Eq.(4) can be used for calculating the gain $G \propto \langle \gamma^{(2)} \rangle$ by neglecting the term in $\underline{p}_t$.

Calculation of $\gamma^{(1)}$ by means of spontaneous radiation field

The first order energy variation $\gamma^{(1)}$ can beeasily calculated by using the integral relation

$$\gamma^{(1)} = \frac{e}{\zeta} \iint_{4\pi} \hat{\underline{E}}_L^{*}(\hat{n},\omega) \cdot \hat{\underline{E}}_e(\hat{n},\omega)\, d\Omega + c.c. \quad , \tag{5}$$

where ζ = 120 π ohm, $\hat{\underline{E}}_L = \lim_{R\to\infty} R\underline{E}_L$ as $R\to\infty$ and $d\Omega$ is the differential solid angle pointing along the direction $\hat{n} \triangleq \underline{R}/R$. $\underline{E}_L$ and $\underline{E}_e$ represent respectively the laser field, supposed monochromatic of frequency ω, and the field radiated by the electron moving in the undulator field. Equation (5) can be justified starting from the following form of the Maxwell equation reciprocity theorem,

$$\underline{j}_1 \cdot \underline{e}_2 = -\frac{\partial}{\partial t}\left(\epsilon\, \underline{e}_1 \cdot \underline{e}_2 + \mu\, \underline{h}_1 \cdot \underline{h}_2\right) - \nabla \cdot (\underline{e}_1 \times \underline{h}_2 + \underline{e}_2 \times \underline{h}_1) \quad , \tag{6}$$

for two fields 1 and 2, one of which (2) is sourceless (gaussian beam) and the other one is sustained by the current $\underline{j}_1$ (electron undulating in the wiggler). Small letters have been used for indicating the field components to distinguish quantities depending on time t from the Fourier components (f.i. $\underline{E}(\hat{n},\omega)$) which appear in Eq.(5).

The electron phase appears in Eq.(5) as a fluctuating phase factor which multiplies the integral calculated for a particular phase. Consequently, the average value of $\langle \gamma^{(1)2} \rangle$ is given by the simple formula

$$\langle \gamma^{(1)2} \rangle = \frac{2e^2}{\zeta^2} \left| \iint_{4\pi} \hat{\underline{E}}_L(\hat{n},\omega) \cdot \hat{\underline{E}}_e(\hat{n},\omega)\, d\Omega \right|^2 \quad . \tag{7}$$

The field $\underline{E}_e$ has been calculated by expanding the field integral

$$\underline{I}(\hat{n},\omega) = \int_0^T \hat{n} \times (\hat{n} \times \underline{\beta}_e) \exp i\omega(t - \hat{n}\cdot \underline{r}_e/c)\, dt \quad , \tag{8}$$

into a series of products of Bessel and sin(x)/x functions, as originally shown by Alferov. The presence of the half poles has been explicitely considered by representing the undulator vector potential $\underline{A} = \hat{x} A_x$ in the form [18]

$$A_x = \begin{cases} \eta(1 - \cos\zeta) & \text{(half poles)} \\ 2\eta - 1 - \cos\zeta & \text{(undulator)} \end{cases} , \tag{9}$$

where $\zeta = 2\pi y/\lambda_w$ and η is a parameter measuring the relative strength of the two half poles. For a perfectly compensated undulator $\eta = (N-1)/(2N-1)$, N being the number of periods.

The field computed numerically has been compared with the measured pattern, which is shown in Fig. 4. The agreement between the two patterns has been excellent, even by neglecting in the numerical calculations the divergence of the electron beam. In order to clarify this circumstance, the spontaneous radiation pattern has been calculated for different values of the bem divergence. As can be seen from Figure 5a, for a divergence of 0.05 mrad the angular pattern is indistiguishhble from that of an electron entering the undulator axially. On the opposite, for a divergence of 0.5 mrad (Figure 5b) the pattern modifications

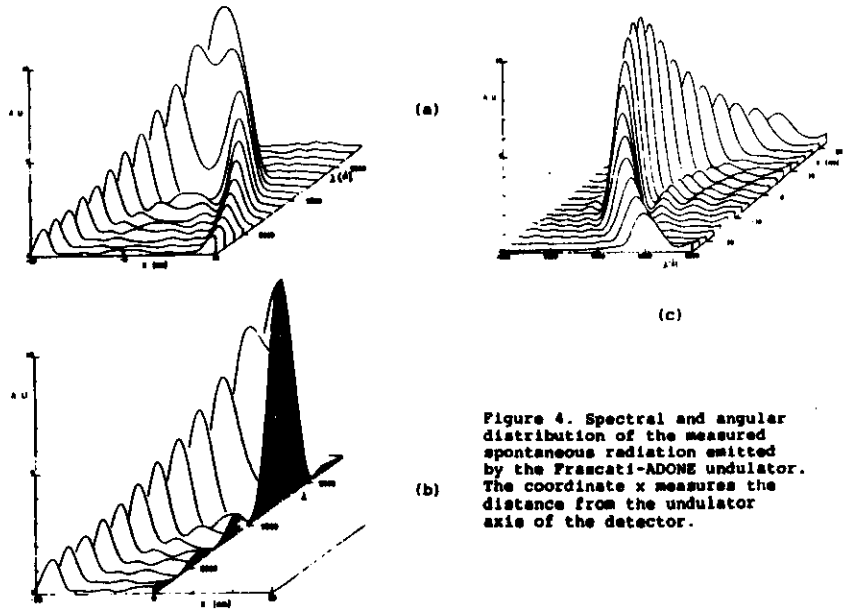

Figure 4. Spectral and angular distribution of the measured spontaneous radiation emitted by the Frascati-ADONE undulator. The coordinate x measures the distance from the undulator axis of the detector.

become quite evident.

The gain of the Frascati FEL has been calculated by means of Eqs. (4) and (7) by using the computer generated field. The peak gain so obtained has been plotted in Figure 6 versus the Rayleigh length or, equivalently, the laser beam angular aperture. Figure 6a refers to a filamentary eletron beam, while Figure 6b applies to the ADONE beam having an envelope of almost 0.3 mm. Note that the maximum gain is obtained for $z_R = 1$ m, which corresponds to a beam waist of 0.45 mm for $\lambda = 6328$ Å. The relative half-apex angular aperture is $\sim$ 0.3 mrad, that is it is almost equal to the aperture of the radiation pattern of the undulator.

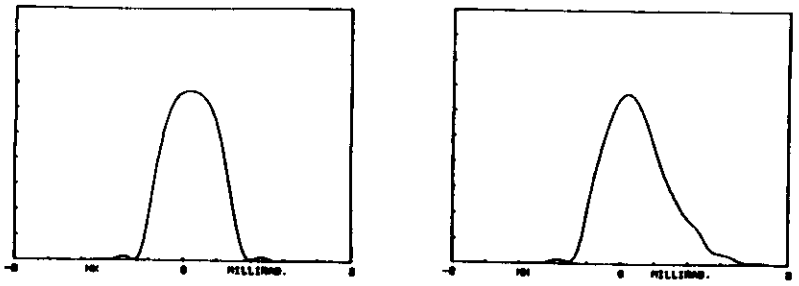

(a) (b)

Figure 5. Angular pattern of the Frscati undulator for a divergence of 0.05 (a) and 0.5 mrad.

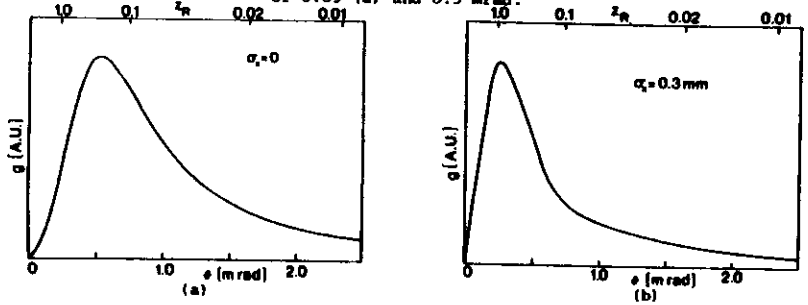

(a) (b)

Figure 6. Maximum gain vs. z_R(m) for a filamentary (a) and the ADONE beam (b).

Acknowledgments

Some of the authors are indebted to M. Velghe and D. Deacon for fruitful discussions, to G. Prisco for the help provided in calculating the gain curves and to A.N. Skrinsky for the preprints of the Novosibirsk group.

References

1. D.A.G. Deacon, Nucl. Instrum. Meth. 208, 171 (1983).
2. P. Ellaume et al., results communicated at the East Sound Conf. on F.E.L. (1983).
3. R. Barbini et al., J. de Physique 44, C1-1 (1983)
4. R. Barbini, A. Cattoni, B. Dulach, C. Sanelli, M. Serio and G. Vignola, Nucl. Instr Instrum. Meth. 190, 159 (1981).
5. A.W. Chao and J. Gareyte, SPEAR-197 PEP-224 (1976).
6. S. Tazzari, LNF Int. Memorandum T-93
7. M. Billardon et al., J. de Physique 44, C1-29 (1983).
8. W.B. Colson and P. Ellaume, Appl. Phys. B29, 1 (1982).

9. W.B. Colson and R.A. Freedman, Phys. Rev. A27, 1399 (1983).
10. J.C. Goldstein and W.B. Colson, Proc. of the 1981 Int. Conf. on Lasers, New Orleans (Dec. 1981).
11. B.J. Coffey, M. Lax and C.J. Elliott, IEEE J. Quantum Electron. QE-19, 297 (1983).
12. J.C. Goldstein, 1983 Los Alamos Conf. on Optics, Santa Fe, N.M., April 1983 (Los Alamos Rept. LA-UR-83-12224).
13. C-M Tang and P. Sprangle, in "Physics of Quantum Electron." eds. S.F. Jacobs et al., Addison-Wesley, Reading, MA (1982), vol. 9, p. 267.
14. D.C. Quimby and J. Slater, IEEE J. Quantum Electron. QE-19 , 800 (1983).
15. N.A. Vinokurov, On the classical analog of the Einstein relations between spontaneous emission, stimulated emission and absorption (in Russian), preprint no. 81-02, Inst. of Nuclear Physics, Novosibirsk (1980).
16. S. Krinsky, J.M. Wang and P. Luchini, J. Appl. Phys. 53, 5453 (1982).
17. P. Luchini, G. Prisco and S. Solimeno, Optimizations of the gain of a FEL for a gaussian beam, these proceedings.
18. R. Barbini et al., Experimental and theoretical analysis of the radiation emitted by the ADONE linear undulator at finite distance (submitted to Nuovo Cimento).

Broadband optical cavities for infrared free electron lasers: analysis and preliminary experimental results

Antonello Cutolo, Butrus T. Khuri-Yakub, and John M. J. Madey

In this work we describe the complete design of a broadband optical cavity for a new IR free electron laser under construction at Stanford using the first section of the Mark III linac. Although the numerical results apply specifically to the Mark III FEL, the general scheme is applicable to any tunable free electron laser. In the last section, some preliminary experimental results for the acoustooptic output coupler are reported and discussed.

I. Introduction

One major advantage of the free electron laser (FEL) is the capability for broadband tuning through variation of either the wiggler magnetic field strength or the electron energy. But, as in any laser system, the practical attainment of broadband tunability requires broadband optical feedback. In an earlier publication we concluded that, in the IR, broadband optical feedback could best be accomplished through use of metallic mirrors in a stable optical cavity configuration.[1]

The main disadvantage of this cavity configuration is the output coupling problem. As a solution to this problem, we have proposed use of an intracavity acoustooptic output coupler. In particular, we have described several different possible configurations for the output coupler in the wavelength range of $2\ \mu m < \lambda < 10\ \mu m$ and have evaluated the possible materials for the acoustic device. We have also conducted an extensive analysis of the self-induced thermal effects and the effects of finite bandwidth. The aim of the present paper is to describe the complete design of the 2–10-μm optical cavity for the Mark III FEL.

The structure of the paper is as follows: In Sec. II we describe the optical cavity; in Sec. III we discuss the acoustooptic output coupler together with the acoustic transducer, the switching time, and cavity length shift due to the intracavity output coupler. In Sec. IV we analyze the cavity losses, and finally in Sec. V we report the performances of a prototype of Ge acoustooptic coupler.

II. Optical Coupler

In Ref. 1 we analyzed several different possible configurations for introduction of an acoustooptic output coupler in a metal-mirror optical cavity. After evaluating the advantages and disadvantages of each scheme, we selected the design shown schematically in Fig. 1. The output laser beam is diffracted by the acoustooptic device in a plane normal to the plane of oscillation of the electron beam. We have chosen this scheme because it introduces the lowest insertion losses and offers the possibility to satisfy both the polarization conditions on the acoustic and optical waves in the crystal and the Brewster condition. Inspection of the configuration in Fig. 1 also indicates that the optical losses in the coupler will be independent of the position at which the radiation enters the crystal, thus preserving the basic structure of the optical modes in the resonator.

The optimization of FEL performance requires careful choice of the basic geometrical quantities listed in Fig. 1. First, the synchronization of the electron bunches generated by the accelerator-injector and the optical radiation stored in the cavity requires that the cavity length $l \equiv l_1 + l_2 + 2l_M + l_0$ satisfy the condition

$$l = mc\tau/2 = m \cdot 5.252\ \text{cm}, \tag{1}$$

where c is the velocity of light *in vacuo*, m is any positive integer number, and $\tau = 1/f = 350$ psec ($f \equiv$ accelerator operating frequency = 2.856 GHz in the Mark III) is the time separation between the bunches in the electron beam. Moreover, the cavity length should be as short as possible. Given the undulator length, $l_0 \simeq 1.3$ m, and the bending magnet lengths, $l_M = 5$ cm, $l_1 \gtrsim 10$ cm, $l_2 \gtrsim 10$ cm, the final cavity length should be 178 cm ($m = 34$).

All authors are with Stanford University, Stanford, California 94305; B. T. Khuri-Yakub is in the E. L. Ginzton Laboratory, the other authors are in the High Energy Physics Laboratory.

Received 6 December 1983.
0003-6935/84/172935-09$02.00/0.

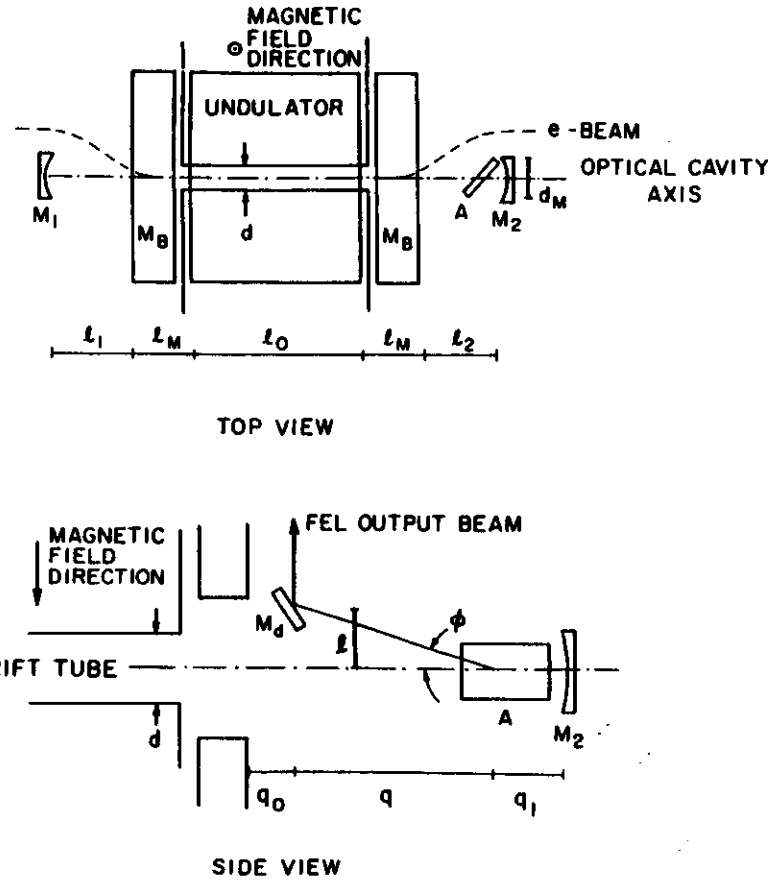

Fig. 1. Top and side view of the vacuum chamber of the Mark III FEL with the optical cavity and the acoustooptic output coupler A. M_B designates the bending magnets. M_1 and M_2 are the metal cavity mirrors, and M_d is a deflecting mirror to extract laser beam.

Since the maximization of the small signal gain requires an optimization of the filling factor, we have chosen the Rayleigh parameter Z_R of the cavity to minimize the volume of the optical mode integrated over the undulator length, i.e., $Z_R = l_0/\sqrt{12}$. Assuming a maximum error for $Z_R \simeq 1\%$ we obtain $R_1 = R_2 = 78 \pm 3$ cm, where R_1 and R_2 are the curvature radii of the two cavity mirrors M_1 and M_2. With such a cavity the $1/e$ radius of the electric field in the laser mode at the mirrors varies from ~2.2 mm (at $\lambda = 10\ \mu m$) to ~1 mm (at $\lambda = 2\ \mu m$). With these values of the laser spot size, the requirement that the diffraction losses be lower than 10^{-3} (at $\lambda = 10\ \mu m$) indicates that the mirror radii must be 6.35 mm (0.25 in.) or larger.

The choice of the e$^-$-beam drift-tube diameter d is somewhat more involved due to the conflicting requirements of low diffraction losses and high magnetic field. High small signal gain requires a high undulator magnetic field in the interaction region and hence a short distance between the undulator poles. On the other hand, low diffraction losses require a large drift-tube diameter. In the Mark III FEL, a drift-tube inside diameter $d = 6$ mm (Fig. 2) allows a maximum K^2 value of 1.7 while maintaining diffraction losses below 5% at $\lambda = 10\ \mu m$.

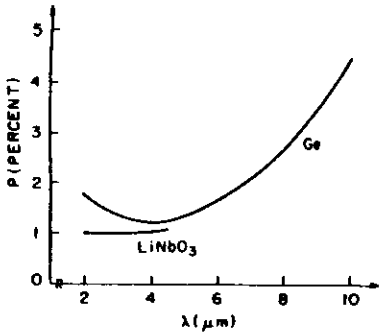

Fig. 2. Total losses of the cavity P including diffractioin losses, absorption losses, insertion losses due to the acoustooptic coupler. A Ge crystal 3 mm thick is assumed with $LiNbO_3$ coupler and ballast thickness of 4.5 and 0.7 mm.

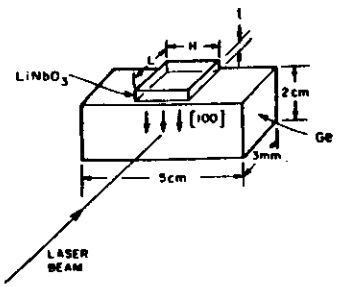

Fig. 3. Schematic of the prototype Ge crystal with the $LiNbO_3$ transducer attached. The shear-mode acoustic waves propagate in the 100 direction as indicated by the arrow in the figure. The dimensions of the prototype $LiNbO_3$ transducer were: $L = 2.8$ mm, $H = 1.5$ cm, $t = 31$ μm.

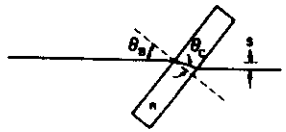

Fig. 4. Acoustooptic crystal inserted at Brewster angle $\theta_B = t_g^{-1}(n)$ and $\theta_B + \theta_c = 90°$. n is the reflective index seen by the incident laser beam. The electric field is assumed to be polarized in the plane of the figure.

III. Output Coupler

The general design considerations for the acoustooptic intracavity output coupler include

(1) a prescribed diffraction efficiency (≈5–10%) depending on the available small signal gain,

(2) a diffraction angle (≈90 mrad) large enough to permit the practical extraction of the diffracted beam from the optical cavity (see Fig. 1),

(3) low insertion losses,

(4) short switching time for cavity-dumping or high-time resolution studies,

(5) minimum deflection of the optical mode position and small change of the optical path length in the cavity due to the dispersion properties of the material used for the output coupler.

Our objective in this section is to review these conditions and the solutions we have developed for the Mark III FEL. To analyze the first two conditions we note that the diffraction efficiency η and the diffraction angle ϕ_c are given, respectively, by[2,3]

$$\begin{cases} \eta = \sin^2\left(\frac{\pi}{2}\sqrt{\frac{2}{\lambda^2}\frac{L}{H}MP_{ac}}\right), & (2) \\ \phi_c = \frac{\lambda}{nV_s}f_{ac}, & (3) \end{cases}$$

where λ is the optical wavelength *in vacuo*; L is the interaction length of the optical beam with the acoustic wave; H is the transverse dimension of the acoustic transducer (see Fig. 3); P_{ac} is the acoustic power delivered into the crystal; n, V_s, and M are the refractive index, velocity of the sound, and figure of merit of the host crystal, respectively; and f_{ac} is the acoustic frequency. To avoid confusion, we recall that ϕ_c is defined as the angle between the incident and the diffracted optical wave vectors inside the crystal. We explicitly observe that Eq. (2) is based on the complete phase matching condition. The influence of this factor together with the problems caused by self-induced thermal gradients and linewidth effects have been carefully discussed in prior publications.[1,4]

To minimize the reflection losses without using antireflection coatings, we decided to insert the acoustooptic device at the Brewster incidence angle (Fig. 4). While several configurations are possible, in principle, we have chosen the configuration shown in Fig. 1 because it minimizes absorption losses switching times. Moreover, in this configuration the Brewster plate thickness is constant so that absorption losses in the acoustooptic element are independent of transverse position, thus minimizing mode distortion.

Initially, we considered the use of a Ge crystal over the full (2–10-μm) range because of its high figure of merit (Appendix) and low insertion loss. However, two-photon absorption may be a problem in Ge at $\lambda <$ 4-μm wavelengths at the power levels expected in the Mark III FEL. Using the two-photon absorption data reported in the literature[5,6] for nanosecond pulses in the 2–3-μm range, we compute an absorption coefficient $\alpha > 10\ cm^{-1}$ at the maximum power of the Mark III FEL. This would be prohibitively large. Although the actual two-photon absorption in the Mark III FEL will probably be smaller than this number since the optical pulses will be picoseconds, rather than nanoseconds, long, it is clear that there will be some power level beyond which Ge cannot be used. As an alternative to Ge in the 2–4-μm band at high power, we have developed a second coupler for the Mark III FEL using $LiNbO_3$. Although $LiNbO_3$ does not have as high a figure of merit as Ge it is the next best material[2,7] and does not suffer two-photon absorption.

By simple optical considerations it is easy to verify that the external diffraction angle (ϕ, see Fig. 1) is given by

$$\phi = n\phi_c = \frac{\lambda}{V_s}f_{ac}. \quad (4)$$

A. Acoustic Transducer

In our acoustooptic system, we cannot use any intracavity focusing system which would increase insertion losses. Thus we need an acoustic transducer with a large area (~0.5 cm^2) and a fairly low geometrical factor $[L/H \approx 0.2\text{–}0.5$, see Eq. (2) and Fig. 3].

The acoustic transducer is required to have a fairly wide bandwidth to accommodate an interaction with the laser beam over a wavelength range of 2–10 μm. To secure this broadband match, we must in principle be concerned with two matching problems: the acoustic match of the transducer and the crystal used as the output coupler, and the electrical match of the transducer and the generator used to drive it. Fortunately, the acoustic match is straightforward. The acoustic impedance[8,9] defined as the ratio between the velocity of the sound and the density has nearly the same value for the transducer and the acoustic device in both our configurations. Practically, we must use $LiNbO_3$ as the transducer material for the Ge coupler because it is able to excite the acoustic shear waves we need (Table I). But, given the technological limitations in making this acoustic transducer with a large area (~0.5 cm^2), we decided to avoid designs requiring transducers polished to a final thickness below 20 μm, corresponding to a central frequency $f_{ac} \approx 90$ MHz. (The thickness is equal to half of the acoustic wavelength at the center frequency.) For the $LiNbO_3$ coupler, which requires a thinner transducer, we have specified a ZnO transducer because ZnO can be fabricated in films thinner than 20 μm using a sputtering technique, and the $LiNbO_3$ coupler can be driven by a longitudinal acoustic wave. Unfortunately, transducers built using a sputtering technique are able to excite only longitudinal waves[10] and cannot be used to drive the Ge coupler in our configuration.

With regard to the electric matching problem, we observe that equivalent input impedance of a transducer Z_{eq} has a resistive and a capacitive part. Both components are roughly proportional to the quantity t/Af_{ac} (t is the thickness of the transducer). In the acoustic transducers A is a few square millimeters, and the couplers are designed to work only at one wavelength. Under these conditions it is easy to get $|Z_{eq}|$ close to 50 Ω, and the capacitive part can be compensated by using an appropriate inductor. This can easily provide a nearly perfect electrical match. For our purposes this reactive matching cannot be used because the bandwidth of the transducer shunt capacitance and the matching inductor would be too small.

We have designed acoustic transducers for each regime of operation of the Ge and $LiNbO_3$ output couplers. The optic and acoustic data for the materials used in the two transducer configurations we propose are shown in Table I.

The coupling efficiency η_{ac} (the ratio between the acoustic power inside the crystal and the electric power delivered by the rf amplifier) for the transducer with a Ge crystal covering the whole optical frequency range as shown in Fig. 5. The coupling efficiency η_{ac} is plotted in Fig. 6 for a $LiNbO_3$ crystal in the 2–4-μm optical range.

In the first case (only a Ge crystal) it is possible to get a diffraction angle of $\sim 8 \times 10^{-2} \approx 4.5°$. In the second case (Ge and $LiNbO_3$ crystals) the diffraction angle is a little lower $6.5 \times 10^{-2} \approx 3.7°$. This difference is due to the fact that in the design of the $LiNbO_3$ acoustooptic coupler we cannot use acoustic frequencies higher than 210 MHz without strongly reducing the coupling efficiency.

B. Switching Times

The switching time of the acoustic coupler, defined as the time needed to diffract 90% of the total diffracted power, can be estimated according to

$$\tau_c = (2W_t)/V_s,$$

Table I. Main Properties of Ge and $LiNbO_3$[11,12] Useful for Designing the Output Couplers

Crystal	Index of refraction[a]	Optical absorption coefficient	Acoustical absorption coefficient[c] (at f = 500 MHz) (dB/sec)	Optical wave polarization and direction	Acoustic wave polarization and direction	Figure of merit M (m^2/W)	Velocity of sound (cm/sec)
Ge	~4	0.039 cm^{-1} (at λ = 10 μm)	4.2 0.8	∥	Long. (111) Trans. (100)	810×10^{-18} 290×10^{-18}	5.5×10^5 3.5×10^5
$LiNbO_3$	~2.2	10^{-3} cm^{-1} ($\lambda \approx$ 0.5–6.5 μm)		∥ or ⊥ [b]	[b]	7×10^{-18}	6.6×10^5

[a] See Appendix for more detailed information.

[b] To get the highest figure of merit using a $LiNbO_3$ crystal[11] the acoustic wave must be longitudinal and propagate along the x axis. The optical beam must be extraordinarily polarized and make an angle of 35° with the y axis.

[c] Acoustic attenuation is proportional to the square of the frequency.

Note: We could not use Ge in the high figure of merit configuration because it was not possible to satisfy at the same time the polarization requirements imposed by the Brewster condition and by this table. Here the optical E field is assumed polarized in the plane formed by the acoustic and optical wave vectors.

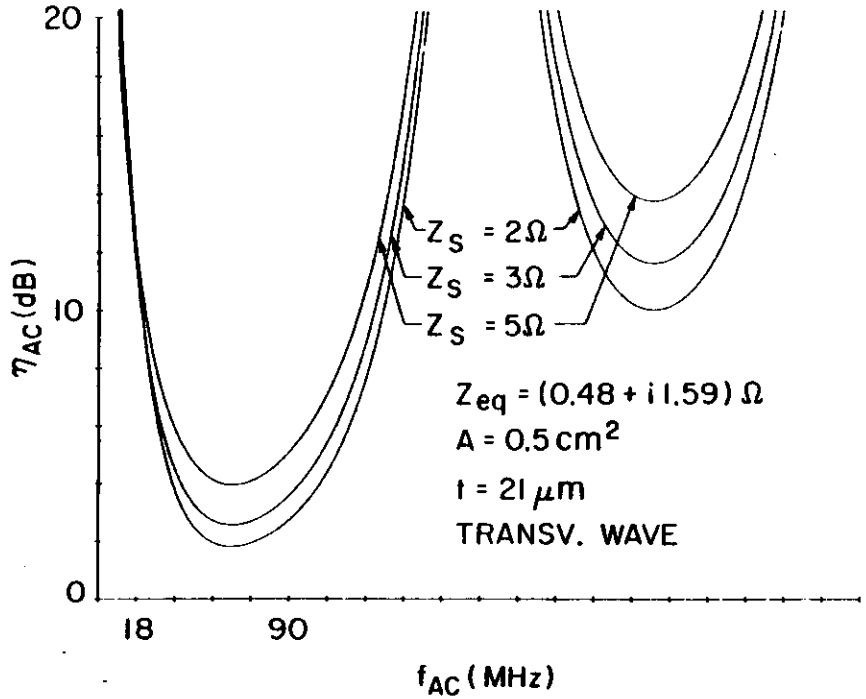

Fig. 5. Plot of $\eta_{ac} = P_{ac}/P_{rf}$ as a function of the acoustic frequency for a $LiNbO_3$ transducer. P_{ac} is the acoustic power in the crystal, and P_{rf} is the electric power delivered by the rf amplifier. This transducer was designed to provide transverse acoustic waves propagating in the [100] direction of a Ge crystal. The acoustic range should be between 27 MHz (λ_{opt} = 10 μm) and 135 MHz (λ_{opt} = 2 μm) to generate a diffraction angle $\phi = 8 \times 10^{-2}$ rad ≈ 4.5°. Z_{eq} is the equivalent impedance of the transducer.

where $W_I = W_A/\sqrt{2}$ is the intensity profile spot size, W_A is the amplitude spot size, and V_s is the velocity of the sound in the acoustic device. Using the results of the previous section, and the data reported in Table I, we obtain the results listed in Table II.

C. Beam Translation and Cavity Length Shift

Because of the different refractive indices of Ge and $LiNbO_3$ ($n \approx 4$ in Ge and $n \approx 2.1$ in $LiNbO_3$), the change from the Ge to the $LiNbO_3$ acoustic crystal will both translate the optical beam and change the effective cavity lengths (Fig. 7). These problems can be solved by exploiting the low absorption coefficient of $LiNbO_3$ and a device developed by Byer and Bennett.[11] The final configuration of the two (Ge and $LiNbO_3$) acoustic couplers is shown in Fig. 7. Assuming the Brewster condition for both elements, it is an easy matter to obtain (Fig. 7)

$$s = t \cdot \frac{n^2 - 1}{n\sqrt{n^2 + 1}} \qquad p = t\sqrt{n^2 + 1}, \tag{5}$$

where p is the variation of the optical cavity length and s is the beam translation due to the insertion of an intracavity material of refractive index n and thickness t at the Brewster angle. The conditions for equal beam translation and optical path are

$$p(\mathrm{Ge}) \approx p(\mathrm{LiNbO_3}) \qquad s(\mathrm{Ge}) \approx s(\mathrm{LiNbO_3}). \tag{6}$$

As Eqs. (5) are linear in the crystal thickness we refer all the results to a 1-mm Ge crystal. In Eqs. (6) we used ≈ instead of = because, given the dispersion properties of Ge and $LiNbO_3$, the two equations can be exactly satisfied only at one wavelength. Solving Eqs. (6), we obtain

$$t_1 = \tfrac{1}{2}\left(\frac{n_2^2 - 1}{n_2\sqrt{n_2^2 + 1}} \cdot \frac{n_1\sqrt{n_1^2 + 1}}{n_1^2 - 1} + \frac{\sqrt{n_2^2 + 1}}{\sqrt{n_1^2 + 1}}\right)$$
$$t = \tfrac{1}{2}\left(\frac{\sqrt{n_1^2 + 1}}{\sqrt{n_1^2 + 1}} - \frac{n_2^2 - 1}{n_2\sqrt{n_2^2 + 1}} \cdot \frac{n_1\sqrt{n_1^2 + 1}}{n_1^2 - 1}\right). \tag{7}$$

By choosing as reference wavelengths 10 μm for Ge and 4 μm for $LiNbO_3$ we get the results plotted in Fig. 8. From these results we can see that for a 3-mm thick

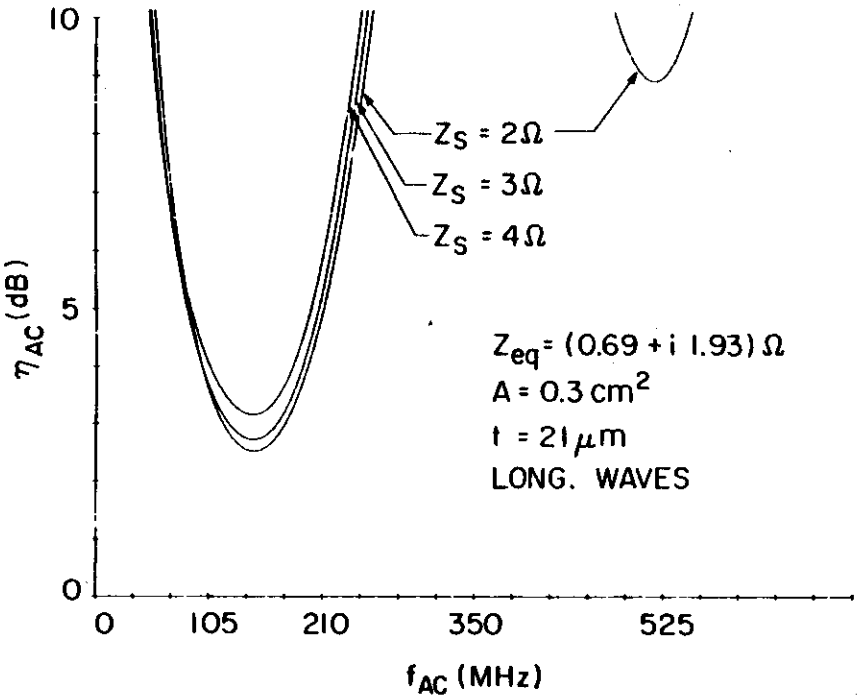

Fig. 6. Plot of $\eta_{ac} = P_{ac}/P_{rf}$ against the acoustic frequency for several values of the rf source output impedance z_s for the $LiNbO_3$ transducer. P_{ac} is the acoustic power inside the crystal, and P_{rf} is the electric power supplied by the rf amplifier. This transducer has been designed to generate longitudinal waves in the $LiNbO_3$ crystal.

Table II. Values of the Switching Time τ_s (in microseconds) Calculated using Eq. (4) for the Ge and $LiNbO_3$ Output Couplers; the Optical Wavelength λ is Expressed in Microns

λ	2	4	6	8	10
Ge	0.6	0.85	1.05	1.21	1.35
$LiNbO_3$	0.33	0.46	—	—	—

Ge crystal (the thickness of the Mark III FEL output coupler) the largest deflection expected when changing couplers would be ~70 μm, while the difference of the optical path lengths for the two crystals would be ~0.4 μsec. This residual $\Delta\rho$ will have to be compensated for by changing the resonator length.

The main effect of the deflection of the mode will be a small wavelength-dependent shift in the direction of the output beam. We can get an estimate of the magnitude of the effect by writing $\Delta\theta \approx \Delta S/R \approx 70 \times 10^{-3}/70 \times 10 \approx 0.1$ mrad. (We have assumed R = 78 cm.) We note that the effect could be suppressed if a small curvature were introduced in the output mirror (M_4 in Fig. 1). But note that for the proposed Mark III

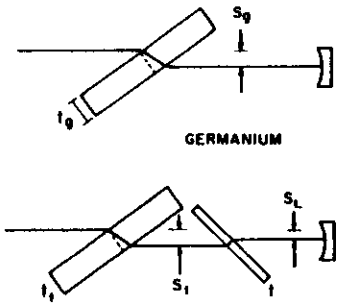

Fig. 7. Insertion of $LiNbO_3$ acoustooptic coupler and of a ballast $LiNbO_3$ crystal in a configuration giving approximately the same transverse deflection and total optical path as in the single Ge crystal.

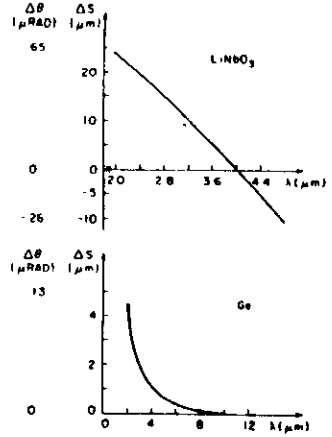

Fig. 8. Plot of the relative steering ΔS for the $LiNbO_3$ short-wavelength coupler plus a ballast $LiNbO_3$ crystal and for the long-wavelength Ge coupler due to their dispersion properties. We assume reference wavelengths of 10 μm for Ge and for 4 μm for $LiNbO_3$. The data reported in this figure are for a Ge coupler 1 mm thick, a 1.54-m thick $LiNbO_3$ output coupler, and a 0.24-mm thick $LiNbO_3$ ballast crystal. The angular deviation due to ΔS is $\Delta\theta \approx 2\Delta S/R$ (R is the radius of curvature of the mirrors). A radius R = 78 cm is assumed.

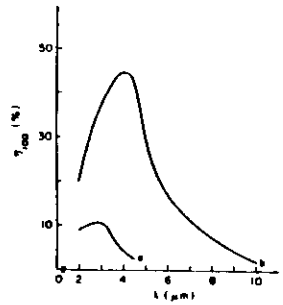

Fig. 9. Plot of the diffraction efficiencies η_{100} for a 100-W rf amplifier. This plot takes into account the coupling of the rf amplifier with the acoustic transducer (Figs. 5 and 6). Curve *a* is for a $LiNbO_3$ coupler with an acoustic transducer designed for the 2–4-μm wavelength range. Curve *b* is for a Ge coupler with the acoustic transducer designed for the 2–10-μm wavelength range.

FEL, the maximum value of $\Delta\theta$ is at most only one-fourth of the angular divergence of the output beam and should prove negligible for most applications.

IV. Cavity Losses

The total losses for a complete round trip are given by the formula

$$P = 2A + 2D + 2l, \tag{8}$$

where P is the total losses, A is the absorption coefficient of each mirror, D is the diffraction losses introduced by the e-beam drift tube (Fig. 9), and l is the insertion losses caused by the acoustic output coupler. Evidently, p will be a function of λ. The variation of A with the wavelength can be neglected compared with the other losses, and we may estimate $A \approx 0.5\%$. The diffraction term D can be estimated as

$$D = 1 - \frac{\int_0^{d/2} r \exp[-2r^2/w^2(\lambda)]dr}{\int_0^{\infty} r \exp[-2r^2/w^2(\lambda)]dr} = \exp[-d^2/2w^2(\lambda)], \tag{9}$$

where d is the diameter of the e-beam pipe (Fig. 1) and $w(\lambda)$ is the spot radius of the mode calculated at the exit of the e-beam drift tube. In our case we can write $[w(\lambda) \approx (2\lambda l_0/\pi\sqrt{3})]^{1/2}$. Finally, the insertion loss can be written as

$$l = \alpha(\lambda) \cdot t, \tag{10}$$

where α is the absorption coefficient of the acoustic material, and t is the path inside the crystal. In Fig. 2 we have plotted the total loss of the cavity against wavelength for a 3-mm Ge crystal and for corresponding $LiNbO_3$ configuration for which, assuming the results of Sec. V, we should get t = 4.7 mm and t_1 = 0.73 mm.

V. Experimental Performance of the Acoustooptic Couplers

In the previous sections we discussed the basic problems encountered in the design of a wideband optical cavity to exploit the tunability attainable in a free electron laser. In Sec. III, in particular, we described an acoustooptic modulator for use as the output coupler in an infrared FEL. In this section we review the experimental performance of a prototype Ge acoustooptic coupler at λ = 3.4 μm.

The prototype was made by a 2-cm × 5-cm × 3-mm Ge crystal (Fig. 5). On its top, a 31-μm thick $LiNbO_3$ acoustic transducer was mounted to excite shear-mode acoustic waves propagating along the [100] direction in the Ge crystal. The Ge crystal and the $LiNbO_3$ transducer were bonded with an indium–chrome–gold alloy.

Experimentally, the bonding process is the most crucial step in the fabrication process. Any scratch or dig on the indium bonding alloy can result in breakage of the acoustic transducer, while variations in the thickness of the indium can result in thickness variations or pinholes in the transducer if the transducer is ground or polished after mounting. This is a particular problem in the case of thin (<40-μm) large area transducers (>0.2 cm^2) such as used in this experiment. Experimentally, these defects can produce both a shift in the resonant frequency of the transducer and a reduction in the effective area (Fig. 10). Fortunately, longitudinal mode transducers do not suffer these problems since the preferred material, ZnO, can be

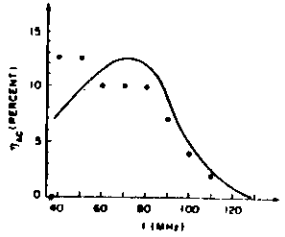

Fig. 10. Theoretical and experimental results for the acoustic responsivity η_{ac} for the prototype Ge acoustooptic coupler (Fig. 3).

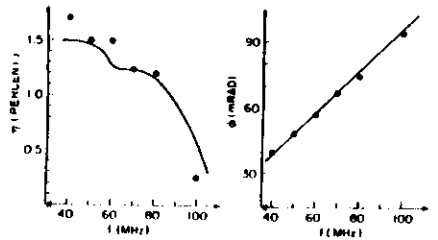

Fig. 11. Diffraction efficiency and diffraction angle for the same devices reported in Fig. 3. The data were taken using a He–Ne laser with λ = 3.39 μm. The diffraction angle $\phi = \lambda/\Lambda$, is the angle between the input and the diffracted beam outside the crystal. The theoretical curves have been normalized using the experimentally observed acoustic responsivity shown in Fig. 10.

applied to the acoustooptics crystal as a uniform thickness layer using a sputtering technique.

To test the performance of the shear-mode $LiNbO_3$ transducer we first measured its acoustic responsivity η_{ac}, defined as the ratio between the acoustic power effectively coupled to the germanium and the electric power delivered by the rf amplifier, by measuring the relative amplitude of the signal induced in the transducer by the acoustic wave reflected from the back surface of the crystal.

In Fig. 10 both theoretical and experimental values of η_{ac} have been reported for the transducer. No impedance matching was attempted in the experiment between the transducer (input impedance $|z_i| \approx 1\ \Omega$) and the power amplifier output impedance (≈50 Ω).

In Fig. 11 we compare the theoretical and experimental results for the diffraction efficiency and the diffraction angle of the prototype coupler normalizing the data for the experimentally measured values of η_{ac}:

$$\eta = \sin^2\left(\frac{\pi}{2}\sqrt{\frac{2}{\lambda^2}\cdot\frac{L}{H}\cdot M\cdot\eta_{ac}\cdot P_{el}}\right), \tag{11}$$

where P_{el} is the electric power delivered by the rf amplifier (28 W in this experiment). As expected, the agreement between the normalized theoretical and experimental values of η and the diffraction angle is excellent. Given the experimental difficulties in bonding the transducer to the crystal, the principal difficulty for these couplers is clearly the acoustic responsivity of the transducer. Our experimental results with the prototype coupler, as indicated in Fig. 10, provide good evidence that these difficulties are solvable.

Helpful discussions with G. Kino are warmly appreciated. This work was supported in part by the Office of Naval Research under contract N00014-78-C-0403 and by the Consiglio Nazionale Delle Ricerche of Italy. The permanent affiliation of Antonello Cutolo is I.N.F.N. and G.N.E.Q.P., Istituto Elettrotechnico, Napoli.

John M. J. Madey also holds an appointment in the Department of Electrical Engineering.

Appendix: Dispersion Relations for Ge and $LiNbO_3$

We report, in this Appendix, the main properties (Table I) of Ge (single crystal) and $LiNbO_3$ useful to design an acoustooptic device.

The dispersion relations are given by:

For Ge (2 μm < λ < 20 μm) (Ref. 12)

$$n(\lambda) = 3.99931 + 0.391707q + 0.163492q^2 - 6\times10^{-6}q^3 + 5.3\times10^{-5}q^4 \text{ at } T = 300\text{ K},$$

$$q = (\lambda^2 - 0.028)^{-2}\ \lambda \text{ expressed in microns}, \tag{A1}$$

$$dn/dT = (1.5 \pm 0.2)\times10^{-4}\ K^{-1}.$$

For $LiNbO_3$ (Ref. 13)

$$n_o^2 = 4.913 + \frac{1.173\times10^5 + 1.65\times10^{-2}T^2}{\lambda^2 - (212 + 2.7\times10^{-5}T^2)^2} - 2.78\times10^{-5}\lambda^2,$$

$$n_e^2 = 6.5567 + 2.605\times10^{-7}T^2 + \frac{0.97\times10^5 + 2.7\times10^{-2}T^2}{\lambda^2 - (201 + 5.4\times10^{-5}T^2)^2} - 2.24\times10^{-5}\lambda^2, \tag{A2}$$

where T is the absolute temperature in Kelvin and λ is the wavelength in nanometers. Equations (A2) can be considered a good approximation in the 0.4-μm < λ < 4-μm range.

References

1. A. Cutolo and J. M. J. Madey, "Acoustooptic Output Coupler for Free Electron Lasers," in *Free-Electron Generators of Coherent Radiation* Proc. Soc. Photo-Opt. Instrum. Eng. xx, 75 (1984).
2. A. Yariv, *Quantum Electronics* (Wiley, New York, 1975).
3. R. W. Dixon, "Acoustic Diffraction in Anisotropic Media," IEEE J. Quantum Electron. QE-3, 85 (1967).
4. A. Cutolo and J. M. J. Madey, "Self-induced Thermal and Linewidth Effects in Nonlinear Optical Interactions," submitted to IEEE J. Quantum Electron.
5. A. F. Gibson, C. B. Hatch, P. N. D. Maggs, D. R. Tilley, and A. C. Walker, "Two-Photon Absorption in Indium-Antimonide and Germanium," J. Phys. C 9, 3259 (1976).
6. C. Y. Leung and M. O. Scully, "Direct Free-Hole Absorption and Transient Optical Properties of the Solid State Plasma in Ge," Phys. Rev. B 23, 6796 (1981).
7. D. A. Pinnow, "Guidelines for the Selection of Acoustooptic Materials," IEEE J. Quantum Electron. QE-6, 223 (1970).
8. G. S. Kino, *Acoustic Devices and Analog Signal Processing* (Prentice-Hall, Englewood Cliffs, N.J., 1984).

10. B. T. Yakubi, J. G. Smith, and T. Barbee, "Reactive Magnetron Sputtering ZnO," J. Appl. Phys. 52, 7 (1981).
11. K. Bennet and R. L. Byer, "Computer-Controllable Wedged-Plate Optical Variable Attenuator," Appl. Opt. 19, 2048 (1980).
12. W. L. Wolfe and G. J. Zissis, *The Infrared Handbook* (Office of Naval Research, Department of the Navy, Washington, D.C., 1978).
13. F. Zernike and J. E. Midwinter, *Applied Nonlinear Optics* (Wiley, New York, 1972).
14. R. W. Dixon and M. G. Cohen, "A New Technique for Measuring Magnitudes of Photoelastic Tensors and its Applications to Lithium Niobate," Appl. Phys. Lett. 8, 205 (1966).
15. R. L. Abrams and D. A. Pinnow, "Acoustooptic Properties of Crystalline Germanium," J. Appl. Phys. 41, 2765 (1970).

Meetings Calendar continued from page 2930

1984
October

6–10 NSF Regional Conf.: Minimal Surfaces & Their Applications to Low-Dimensional Topology, Oklahoma State U., Stillwater *NSF, Math. Sciences, Wash., D.C. 20550*

8–11 Digital Image Processing & Applications course, Wash, D.C. *Cont. Eng. Educ. Program, Geo. Wash. U., Wash., D.C. 20052*

8–12 Semiconductor Lasers course, Elmsford, N.Y. *Educ. Dir., Laser Inst. of Amer., 5151 Monroe St., Suite 118W, Toledo, Ohio 43623*

9–12 European Conf. on Optics, Optical Systems & Applications, Amsterdam *J. Langelaar, Lab. Physical Chemistry, Lieuwe Achtergracht 127, 1018 WS Amsterdam, The Netherlands.*

9–12 37th Ann. Gaseous Electronics Conf., Boulder *E. Beaty, Mail Stop 524.11, NBS, Boulder, Colo. 80303*

10–12 9th European Specialist Workshop on Active Microwave Semiconductor Devices, Veldhoven *P. Hoyng, Astronomical Inst. at Utrecht, Space Res. Lab., Beneluxlaan 21-3527 HS, Utrecht, The Netherlands*

15–17 16th Ann. Symp. on Optical Materials for High Power Lasers, Boulder *S. Rivera, Electro-Magnetic Tech. Div., 724.02, NBS, 325 Broadway, Boulder, Colo. 80303*

15–17 Polymer Phase Diagrams Symp., Gaithersburg *I. Sanchez, B210 Polymers Bldg., NBS, Wash., D.C. 20234*

15–17 2nd Int. Conf. on the Future of Optical Memories, Videodisks, & Compact Disks to the Year 2000, New York *Rothchild Consultants, Tech. Opportunity Conf., P.O. Box 14817, San Francisco, Calif. 94114*

15–19 Laser Applications in Materials Processing course, San Jose *Laser Inst. of Am., 5151 Monroe St., Suite 118W, Toledo, Ohio 43623*

15–19 Laser Safety course, Wash., D.C. *Eng. Tech., Inc., P.O. Box 8859, Waco, Tex. 76714*

16–18 Int. Symp. on Electromagnetic Compatibility, Tokyo *T. Takagi, Dept. of Electrical Communications, Faculty of Engineering, Tohoku U., Sendai, Miyagi 980, Japan*

16–19 Thermal Imagers course, Kent *Sira, Ltd. Conf. Unit, South Hill, Chislehurst, Kent BR7 5EH, U.K.*

18 11th ANACHEM Symp., Troy *P. Beckwith, Detroit Edison Co., 6100 W. Warren, Detroit, Mich. 48210*

19 5th Ann. Strock Sem., Boston *V. Meyer, GTE Lighting Products, Sylvania Lighting Ctr., Danvers, Mass. 01923*

21–25 Cambridge Symp. on Optical & Electro-Optical Eng.: Integrated Optical Circuit Eng., Cambridge *SPIE, P.O. Box 10, Bellingham, Wash. 98227*

21–25 Cambridge Symp. on Optical & Electro-Optical Eng.: Analog Optical Processing & Computing, Cambridge *SPIE, P.O. Box 10, Bellingham, Wash. 98227*

21–26 Cambridge Symp. on Optical & Electro-Optical Eng.: Optical Systems Eng. IV, Cambridge *SPIE, P.O. Box 10, Bellingham, Wash. 98227*

22–23 Technology Past, Present, & Future Mtg., Melbourne *Ex. Officer, Australian Academy of Technological Sciences, Clunies Ross House, 191 Royal Parade, Parkville, Victoria 3052, Australia*

22–26 9th Int. Conf. on Infrared & Millimeter Waves, Osaka *K. Button, Gen. Chairman, MIT Natl. Magnet Lab., Cambridge, Mass. 02139*

22–26 Fiber & Integrated Optics course, Seattle *Geo. Wash. U., Cont. Eng. Educ., Wash., D.C. 20052*

24–25 Frequency Measurements Sem., Boulder *M. Lombardi, Div. 524, NBS, Boulder, Colo. 80303*

26–29 SILMO, Paris *Int. Trade Exhibitions in France, 8 W. 40th St., New York, N.Y. 10018*

28–2 Nov. Factors Influencing Photographic Sensitivity Fast-West Symp., Kaanapali, Haw. *R. Wood, SPSE, 7003 Kilworth Lane, Springfield, Va. 22151*

29–2 Nov. OSA Annual Mtg., San Diego *OSA Mtgs. Dept., 1816 Jefferson Pl., N.W., Wash., D.C. 20036*

30–31 7th Newport Conf. on Fiberoptic Markets, Newport *Kessler Marketing Intelligence, 22 Farewell St., Newport, R.I. 02840*

30–2 Nov. Advances in Remote Sensing Retrieval Methods Interactive Workshop, Williamsburg *A. Deepak, IFAORS, P.O. Box P, Hampton, Va. 23666*

November

4–6 Computer-Aided Testing & Analysis Mtg., Milwaukee *SESA, 14 Fairfield Dr., Brookfield Ctr., Conn. 06805*

4–8 Electronic Imaging—24th Fall Symp., Arlington *SPSE, 7003 Kilworth Lane, Springfield, Va. 22151*

continued on page 2949

Precise measurements of high reflectivity dielectric mirrors

G.C. Barbarino, C. Magna, M.R. Masullo
Istituto di Fisica Sperimentale Università di Napoli
Istituto Nazionale di Fisica Nucleare Sezione di Napoli
Mostra D'Oltremare Pad. 20 80125 NAPOLI

Riassunto: Il problema di caratterizzare con estrema precisione la riflettività di specchi dielettrici è particolarmente significativo nel caso di cavità ottiche con basso guadagno, G.

Il metodo qui descritto per misurare alte riflettività richiede l'utilizzazione di un fascio laser modulato che attraversa una cavità contenente gli specchi. La misura è basata sullo sfasamento dell'intensità del fascio trasmesso rispetto a quello di ingresso, dovuto al tempo di vita media dei fotoni nella cavità.

Introduction

In optical resonators with very low gain (G) it is particulary important to minimize losses. Thus, one has to test continually the mirror reflectivity (R), when its possible variation can be the principal source of losses. One finds a similar situation in Free Electron Laser (FEL) on storage rings for electrons, where the present maximum gain available is about $10^{-3} \div 10^{-4}$. Two examples of accelerator machines, where these feasibility experiments are under way at ACO (ORSAY laboratory - PARIS) and ADONE (national lab. of FRASCATI - INFN Italy).

What is a FEL?

A tune modulated beam of free electron bunches, passing through the magnetic field of an ondulator, emittes synchrotron radiation (spontaneous).

The emitted photons are reflected between two mirrors placed at the end of the undulator (see figure 1). During a round trip this radiation is amplified by the coherent interaction with the free electrons (active medium) passing again through the magnetic field during the following trips. The laser gain is proportional to N^3, where N is the number of periods of the magnet (undulator).

Two important characteristics of FEL are:

a) the high efficency, due to the energy transfer between laser beam and ricirculating electrons;

b) the tunability (from ultraviolet to millimiter waves); namely changing the electrons energy or the magnetic field of the undulator, the frequency of the laser emission varies.

Because of the low gain of these optical oscillators one needs to minimize all possible losses. This is accomplished by using ultra-high vacuum vessels ($10^{-9} \div 10^{-10}$ Torr) and working with highly reflecting dielectric mirrors ($R \geq 99.97\%$).

In the ADONE FEL cavity SiO_2 - TiO_2 dielectric mirrors are used. The mirrors reflectivity curve is shown in fig.2. Two important problems are connected with this kind of optics: a) precise measurements of R and b) controlling the stability of R during the time, because the mirror degradation, due to the UV component of the incident radiation, varies R.

Figure 3 shows the radiation intensity, I, emitted on the undulator axis, as a function of the harmonic number.

Measurement principle

In order to determine high reflectancies, i.e. near unity, the classical method, based on the comparison between the incident and the reflected flux, is quite inaccurate; on the other side a messurement of the photon lifetime[1], τ, in an optical cavity gives an indirect way which is the more sensitive, the higher R is.

A laser beam, optically or mechanically modulated, passing through a testing resonator, is shifted in phase (ϕ), because of the trapping time of the light between the two mirrors.(Fig.5)

So a measure of ϕ, giving us an estimate of the energy dissipated in the cavity, allows the determination of the reflectivity R.

Let the intensity of the incident beam:

$$I_{in}(t) = I_0 \sin^2 \omega t = \frac{I_0}{2}\left(1 + \sin(\omega t + \phi_1)\right) \qquad (1)$$

For the output signal one has

$$I_{out}(t) = \frac{T I_0}{2(1-R)} + \frac{T I_0 \sin(2\omega t + \phi)}{2(1 - 2R\cos\omega\tau' + R^2)^{1/2}} \qquad (2)$$

where ϕ_i has been put equal to zero, T is the mirror trasmissivity, R the reflectivity, $\tau' = \frac{2L}{c}$ and L the cavity lenght.

For the phase shift between the two waves (incoming and outgoing) one has:

$$\tan\phi = \frac{R \sin\omega\tau'}{1 - R\cos\omega\tau'} \qquad (3)$$

Choosing opportunally the lenght, L, and the frequency ω, $\omega\tau'$ results less than 1 ($\omega\tau' \ll 1$) and the formulas (2) (3) become simpler:

$$I_{out}(t) = \frac{T I_0}{2(1-R)}\left[1 + \sin(2\omega t + \phi)\right] \qquad (4)$$

$$\tan\phi = \frac{R\omega\tau'}{(1-R)} \qquad (5)$$

A comparison between 1) and 4) shows the amplitude and phase differences between the two signals.

If we replace R by its expression as function of τ', $R = \exp(-\tau'/\tau)$(6) with $\tau = n\tau'$, it follows

$$\tan\phi = 2\omega\tau \qquad (7)$$

The last expression shows how a determination of ϕ is linked to τ and so to the losses, that are given by:

$$\Gamma = \frac{1}{Q} = \frac{\tau'}{\tau} = \frac{2L}{c}\left(\frac{1}{\tau_s} - \frac{1}{\tau_a}\right) \qquad (8)$$

where τ_s takes into account the presence of the mirror, while τ_a is referred to the air absorption in the resonator.

Modulation

To obtain a modulated beam, we have used a Pockels' cell (optical modulation).

As is well known[2] this kind of cell is formed by a crystal, which using the change of birefringence due to an external electric field, E, causes a rotation of the polarization of the incident light.

In this situation it is possible to define a transfer function T for the set cell + polarizer

$$T = \frac{I_{OUT}}{I_{IN}} = \sin^2\frac{\Gamma}{2} = \sin^2\left(\frac{\pi}{2}\frac{V}{V_\pi}\right) \qquad (9)$$

where V_π is the applied voltage and V_π gives the value for which the polarization is rotated by 90°.

If the modulation is

$$\Gamma = \Gamma_m \sin(\omega_m t)$$

from (9) we obtain:

$$T = \sin^2\left(\frac{\Gamma_m}{2}\sin(\omega_m t)\right) \qquad (11)$$

In a low-signal regime, $\Gamma_m \ll 1$, expression (11) gives, (by expanding in Bessel Functions):

$$\frac{I_{OUT}}{I_{IN}} \simeq \left(\frac{\Gamma_m}{2}\right)^2 \sin^2\omega_m t \qquad (12)$$

that is analogous to formula (9).

Fig.4 shows what we have described here.

Measurement apparatus

The experimental apparatus is shown in fig.6. A modulated laser source (λ = 6328 Å) enters the testing cavity. Placing the cell in different positions (1 and 2), or, using two different detectors with cell in position 1 we obtain two signals, which are fed into a lock-in amplifier, in order to measure the phase-difference.

The measured intensities are given by expressions 1) and 4). Before analyzing the obtained results, we want to underline two points:

a) one uncorrected alignment between the cell and the laser beam can cause a considerable change of the transfer function, thus changing the output signal.(Figs. 7 and 8)

b) we use a lens of focal lenght, f, showed in fig.6, for the mode matching between the structure of the gaussian laser beam and that of the testing cavity.

Here we write the formulas for the lense distances d_1 and d_2 from the two waists to be matched.

$$d_1 = f \pm \frac{\omega_{o,1}}{\omega_{o,2}} \sqrt{f^2 - f_o^2}$$

$$d_2 = f \pm \frac{\omega_{o,2}}{\omega_{o,1}} \sqrt{f^2 - f_o^2} \qquad (13)$$

where $f_o = \frac{\pi}{\lambda} \omega_{o,1} \cdot \omega_{o,2}$

and $\omega_{o,1}$, $\omega_{o,2}$ are respectively the laser waist and the cavity one.

The sensitivity of the method

Writing expression 3), $\tan\phi = 2\omega n \tau'$ for the modulation frequency, f, in kHz and L in cm, we obtain

$$\tan\phi = 0.37 \times 10^{-7} \cdot f \cdot L \cdot n \qquad (14)$$

where $n = \frac{1}{\ln(\frac{1}{R})}$ (15)

In this way we can estimate the accuracy of this method, knowing that the error on the phase measured by the lock-in is about ± 0.1 degrees. As an example we report in fig. 9 points calculated for f = 50 kHz and L = 30 cm.

By an analysis of formula (14) and of the obtained data, we deduce that it is possible to obtain very good accuracy when

a) R is high, i.e. > 99%

b) L = cavity lenght is also high (50 ÷ 500 cm)

c) one uses sufficient modulation frequencies (50 ÷ 100 kHz).

Experimental results

In fig. 10 we report the phase-shift values versus the cavity lenght. In this way utilizing eq.(14), we determine the value of the mirrors reflectivity from the angular coefficient of:

$$\tan\phi = cost \cdot f \cdot \left(\frac{1}{\ln 1/R}\right) \cdot L \qquad (16)$$

Furthermore we are able to measure the cavity losses, plotting the same data versus 1/L

$$\frac{1}{\tau} = \frac{1}{\tau_0} + \left(\frac{\Gamma_c}{2}\right)\frac{1}{L} \qquad (17)$$

so giving also the air absorption, τ_a - Fig. 11.

One has $R_1 = R_2 = R = 99.42 \pm 0.01\%$ and $\Gamma = 1.36 \times 10^{-3}$.

At the beginning we have said that the interest in this method arised from the need of controlling the mirror damage and, thus, the variation of R.

In conclusion we have tried to understand the obtainable sensivity of this method.

In fig. 12 we report the phase-shift versus the mirror reflectivity, that we have supposed being damaged, after its inserction in the cavity.

Figs. 12 and 10 show that it is possible to verify the damage ($R \rightarrow 99.93\%$) with a precision of 10^{-3}.

References

(1) J.M. Herbelin, et al.
"Sensitive measurement of photon lifetime and time reflectances in an optical cavity by a phase-shift method". - Applied Optics 19, 144 (1980)

(2) A. Yariv:
Quantum Electronics (Wiley, New York - 1982)

Fig.1 Scheme of a FEL cavity on a storage ring

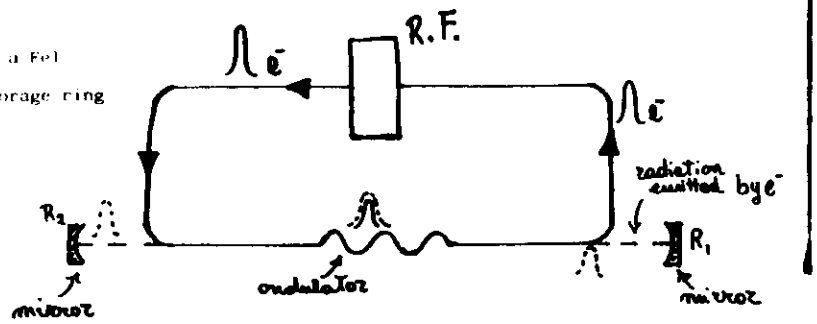

Fig.2 Reflectivity curve for λ_0 =6600 Å - dielectric mirrors (23 strates of SiO_2-TiO_2)

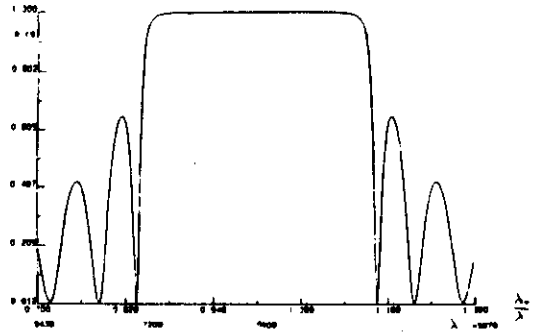

Fig. 4 -Pockels cell :
a) the transfer function
b) the applied modulation voltage
c) the trasmitted intensity

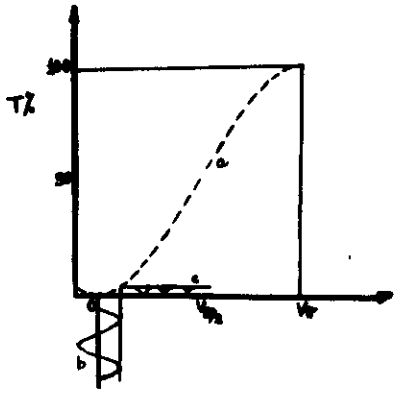

Fig. 5 -Optical cavity: incoming and out of phase exit intensities

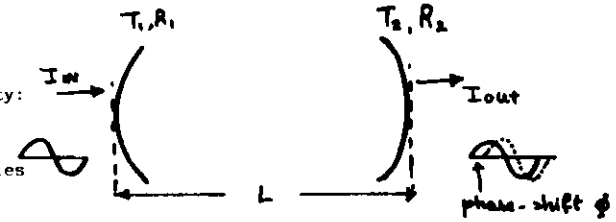

Fig. 6- Measurement apparatus

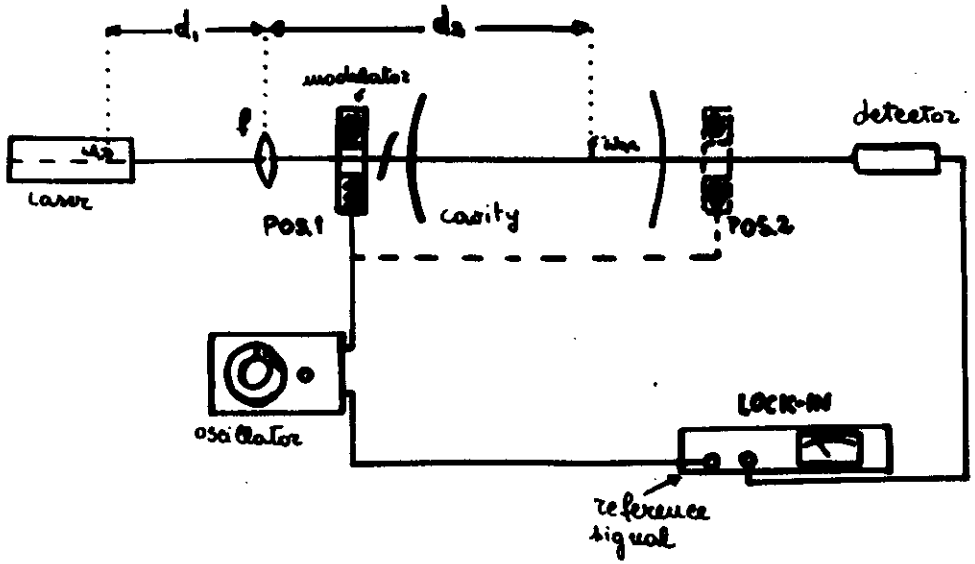

Fig.3 On axis spontaneous radiation intensity versus harmonic number

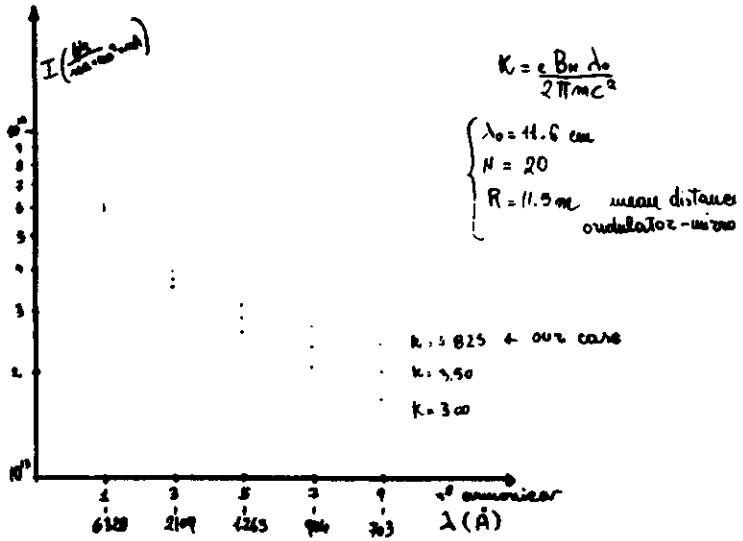

Fig. 7 -Oscilloscope: input voltage into the cell and output signal from the detector

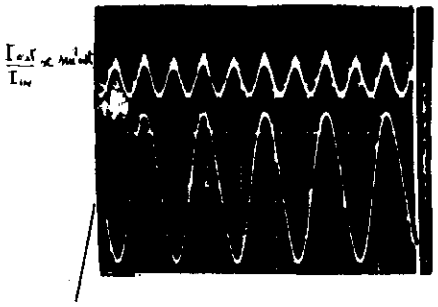

Fig. 8 -Cell response in two cases :good and bad alignment

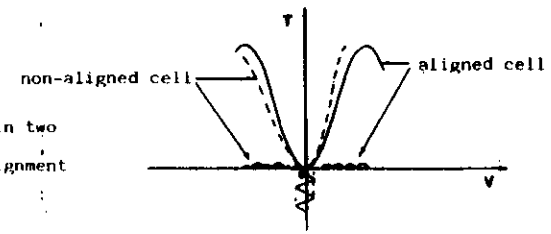

Fig. 9 -Phase-shift versus reflectivity R in a particular configuration. It is shown precision on R measurements.

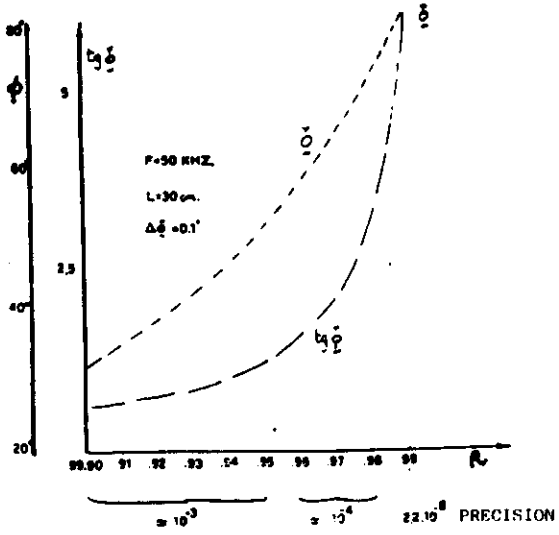

Fig. 10 -Tan ϕ as a function of the cavity lenght,L

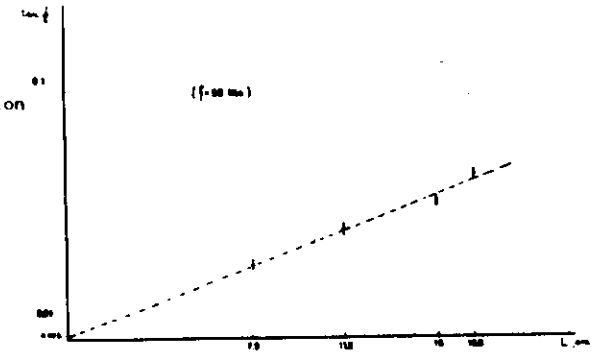

Fig. 11- Reciprocal of time-life versus the inverse of L

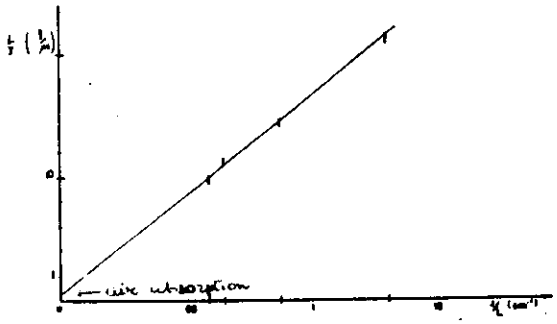

Fig. 12 - Phase-shift as function of damaged mirrors reflectivity

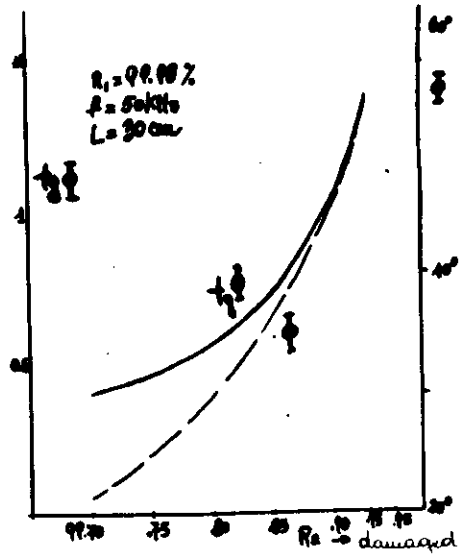

JOURNAL DE PHYSIQUE
Colloque C1, supplément au n°2, Tome 44, février 1983

PRELIMINARY RESULTS OF THE ADONE STORAGE RING FEL EXPERIMENT, LELA

R. Barbini[1+], G. Vignola[1+], S. Trillo[1], R. Boni[2], S. De Simone[2], S. Faini[2], S. Guiducci[2], M. Preger[2], M. Serio[2], B. Spataro[2], S. Tazzari[2], F. Tazzioli[2], M. Vescovi[2], A. Cattoni[3], C. Sanelli[3], M. Castellano[4], N. Cavallo[4], F. Cevenini[4], M.R. Masullo[4], P. Patteri[4], R. Rinzivillo[4], A. Cutolo[5] and S. Solimeno[5]

[1] *INFN, Laboratori Nazionali di Frascati, Frascati, Italy*
[2] *INFN, Laboratori Nazionali di Frascati, Accelerator Division, Frascati, Italy*
[3] *INFN, Laboratori Nazionali di Frascati, Engineering Division, Frascati, Italy*
[4] *INFN, Sezione di Napoli and Istituto di Fisica Sperimentale dell'Università di Napoli, Napoli, Italy*
[5] *Istituto Elettrotecnica dell'Università di Napoli, Napoli, Italy*

Résumé - On donne une courte description de l'expérience LELA (Laser à électrons libres sur Adone). On discute aussi les résultats des mesures de distribution en angle et en énergie de la radiation spontanée et on donne des résultats préliminaires sur les mesures de gain optique.

Abstract - A short description of the LELA (Free Electron Laser on Adone) experiment is given. Results on the spontaneous radiation angle and energy spectra and preliminary results on optical gain measurements are also discussed.

I - INTRODUCTION

LELA (Laser ad Elettroni Liberi in Adone) is a FEL on a storage ring feasibility experiment and it has been described in some detail elsewhere[1),2)]. The relevant parameters are:

Radiation wavelength	5145 Å
Electron energy	625 MeV
Undulator period	11.6 cm
Number of periods	20
Undulator strength (K_{RMS})	3.5

The undulator, a normal conducting electromagnet[3)], has been commissioned in June 1982; spontaneous radiation measurements were first performed in July. In this paper we report on the latter measurements and also on the preliminary measurements of gain on the first harmonic, carried out at the beginning of September. Evidence of gain on the third harmonic is also given.

II - THE SPONTANEOUS EMISSION

The spontaneous radiation produced in the undulator has been measured with the apparatus shown in Fig. 1. A more detailed discussion of the spontaneous radiation results will appear in a separate paper.

A Jobin Yvon H25 monochromator, 24 m downstream from the undulator center, and having a wavelength resolution of 10 Å (FWHM) and an angle acceptance of $\sim .17\ (\mu rad)^2$, was mounted on a support equipped with computer controlled horizontal and vertical movements, and used to scan through the spontaneous radiation angular wavelength distributions. Fig. 2 shows the result of a radial scan through the typical[4),5)] annular radiation pattern, while the first harmonic wavelength distribution is plotted in Fig. 3.

+ On leave from ENEA, Centro di Frascati, Frascati, Italy

33

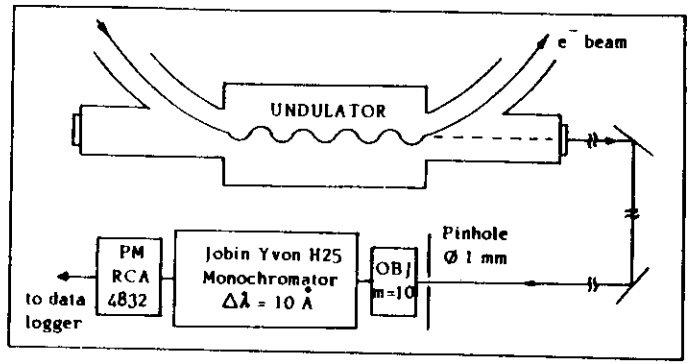

Fig. 1 - Optical setup for spontaneous radiation measurement.

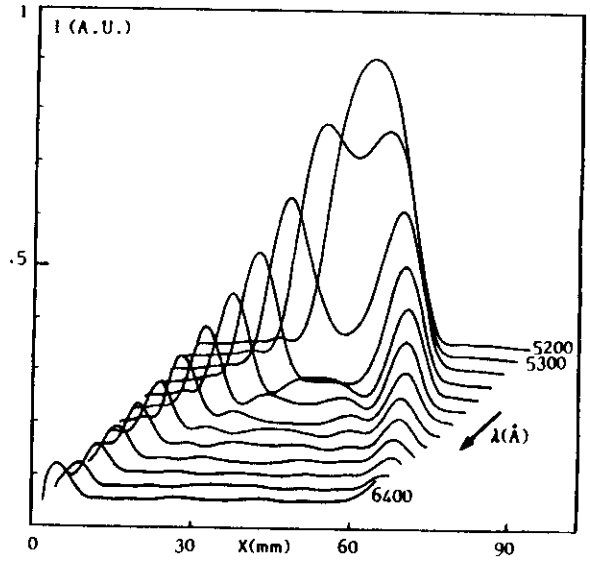

Fig. 2 - First harmonic measured spectral distribution vs. wavelength λ and pinhole position, X, in the radial plane.

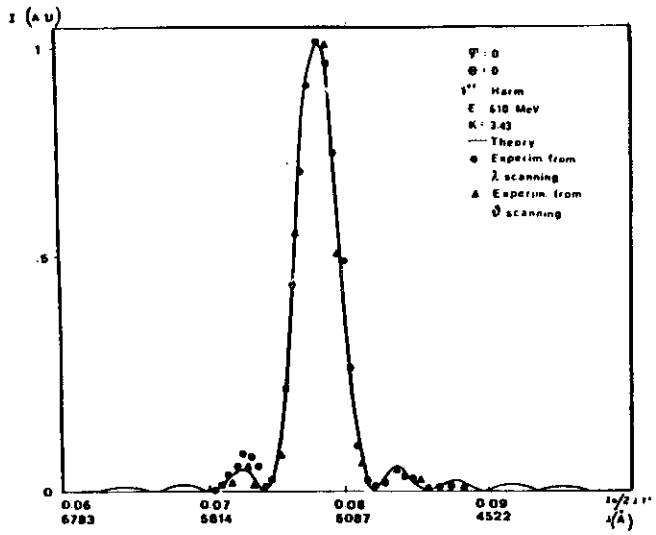

Fig. 3 - First harmonic intensity distribution on the undulator axis, vs. wavelength λ.

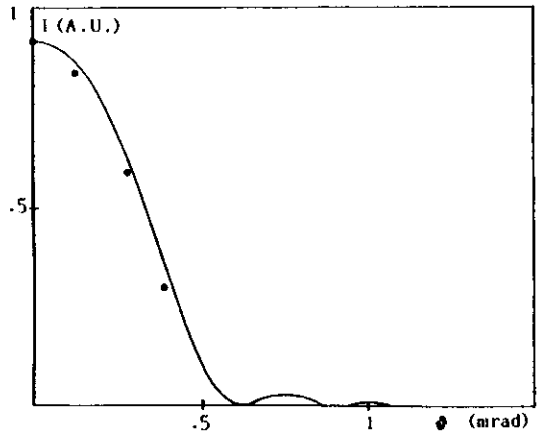

Fig. 4 - First harmonic intensity distribution vs. angle ϑ in the radial plane at $\lambda = 5145$ Å.

Experimental data are well fitted by the theoretical Liénard Wiechert radiation formula[5], and the resulting FWHM is consistent with a pure homogeneously broadened line. From this type of data we can deduce that neither the undulator vertical field gradient nor any electron beam trajectory distortion, nor the e-beam emittance and energy spread affect the spontaneous radiation first harmonic linewidth appreciably.

A first harmonic angular distribution in the radial plane is shown in Fig. 4; a good agreement between theory and experimental points is again apparent. We remark here that the FWHM of spontaneous radiation is very close to that of the laser used to perform the gain measurements (see below); in our case therefore to try to discriminate between the two by means of irises is rather ineffective.

III - THE GAIN MEASUREMENTS

The stimulated radiation produced in the interaction between an external laser beam and the electron bunch stored in Adone has been measured as a function of electron beam energy at $\lambda = 5145$ Å, $K_{RMS} = 3.5$, with a double demodulation system similar to the one in use at ACO[6),7)]. We recall briefly its main characteristics.

A CR-12 laser beam, chopped at a frequency $f_o \sim 900$ Hz, is focussed to a waist $w_o = .35$ mm at the undulator mid point by means of a mode matching telescope (Fig. 5). The overall radiation emerging from the undulator is then collected and brought back onto the optical table; it is then spatially and frequency filtered by means of an iris giving a rejection factor of ~ 1.5, and a high resolution monochromator giving a rejection factor of 250. The optical signal detected by a photodiode is then processed by the electronics sketched in Fig. 6. The current from a fast photodiode (either solid-state or vacuum) is converted into voltage in a resonant active load, tuned to the revolution frequency of the e^- bunch ($f_R = 2.856$ MHz), then narrow band amplified and mixed to a L.O. signal with proper phase relationship with the RF accelerating voltage in order to shift the sidebands at the chopping frequency f_o around f_R (which contain

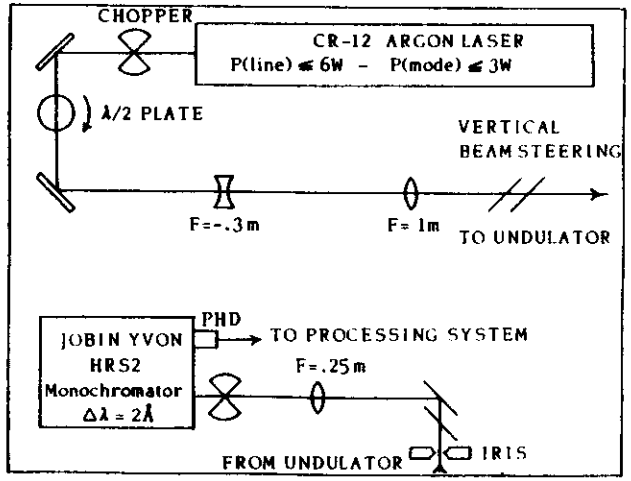

Fig. 5 - Layout of the optics for the gain measurements.

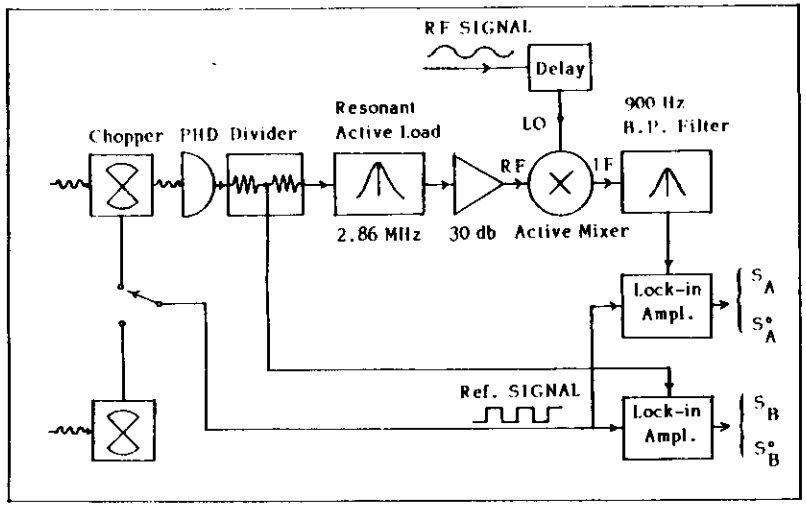

Fig. 6 - Block diagram of the signal processing system.

the stimulated emission information) down to around DC. After further band pass filtering at f_o the signal is fed to a lock-in amplifier, giving a DC signal, S_A, proportional to the average power of stimulated radiation.

A second signal, derived from a voltage divider in the diode supply circuit is directly fed to a second lock-in amplifier and provides the signal S_B proportional to the incoming laser power. The two channels can be intercalibrated by moving the chopper downstream from the undulator, switching the laser off and measuring signals S_A° and S_B° analogous to S_A and S_B but proportional to the spontaneous radiation power only.

The average gain, defined as the ratio between the stimulated power and the laser beam power is given by:

$$\langle G(E) \rangle \simeq \frac{S_A(E)}{S_B} \cdot \frac{S_B^\circ}{S_A^\circ} \qquad (1)$$

The ratio S_B°/S_A° and the signal S_B are practically independent from energy and depend only on the electronics. In our measurements the ratio S_B°/S_A° has a value of $\sim 5\ 10^{-5}$.

The equivalent noise level in our demodulation system corresponds to an average gain in the range from $5\ 10^{-9}$ to 10^{-8}.

During the first set of measurements, reported here, the ratio of stimulated to spontaneous radiation was rather small and the feedthrough[6] of spontaneous radiation into the demodulated channel, due to the modulation of the photodiode transfer characteristics by the high power laser beam, produced an important background to the experiment. The unwanted signal ΔW_{sp} produced by the combined action of the laser radiation and the spontaneous radiation has in fact the same time structure as the stimulated radiation. In the frequency domain this background signal appears in the sidebands around f_R, which should, in principle, contain solely

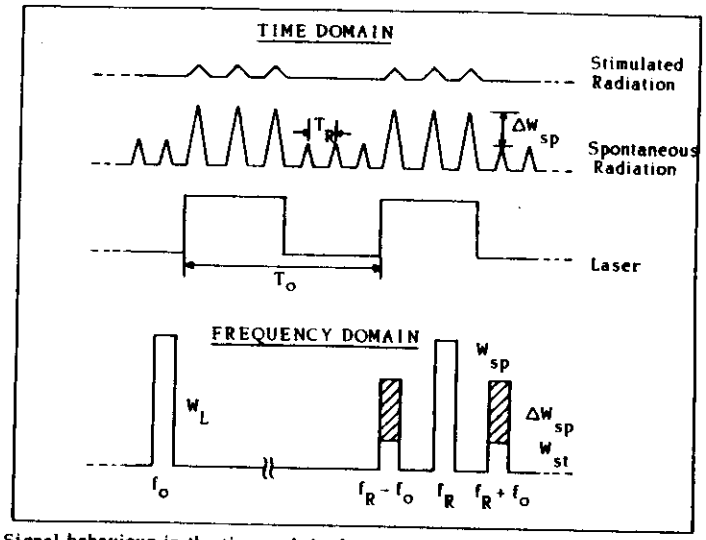

Fig. 7 - Signal behaviour in the time and the frequency domains.

the information from the stimulated power (see Fig. 7). However, the different symmetry of spontaneous and stimulated power with respect to the resonance energy allows the gain to be extracted as a difference between the two curves $S_A(E)$ and $S_A^\circ(E)$. The gain formula (1) must be modified as follows:

$$\langle G(E) \rangle \simeq \frac{S_A(E) - S_A^\circ(E) \left[S_A(E_r) / S_A^\circ(E_r) \right]_{max}}{S_B} \cdot \frac{S_B^\circ}{S_A^\circ} \qquad (2)$$

where the ratio $\alpha = \left[S_A(E_r)/S_A^\circ(E_r) \right]_{max}$ is evaluated at the resonance energy corresponding to the maximum of the spontaneous radiation curve.

The measured signals, S_A and S_A° are plotted vs. beam energy in Fig. 8, and the result of formula (2), corresponding to the same data is shown in Fig. 9. The solid curve in Fig. 9 is a fit to the data using the energy derivative of the spontaneous radiation curve S_A°. The peak gain per pass in this run is:

$$G_{peak} = (.7 \pm .1) \times 10^{-5}$$

having used the measured bunch length.

A number of gain measurements has been performed at various beam currents, as shown in Fig.10. The upper curve is the theoretical small signal gain one would obtain in the hypothesis of maximum filling factor and taking into account the anomalous bunch lengthening in the storage ring and the consequent increase in the beam horizontal dimension due to the fact that, in the lattice configuration so far used, a 2 m dispersion exists in the undulator straight section.

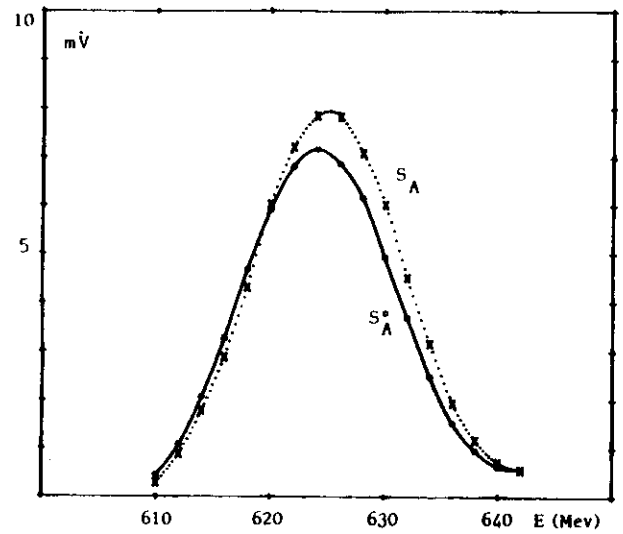

Fig. 8 - Experimental values S_A (laser on) and S_A° (laser off). Electron beam current i = 18 mA in one bunch. The statistical error is not visible on this scale.

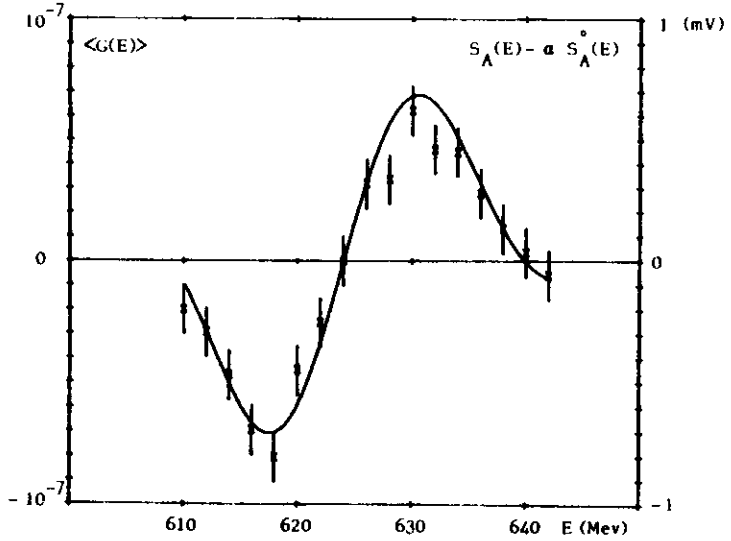

Fig. 9 - Gain signal as obtained from (2), using signals S_A and S_A° of Fig. 8. The solid curve is a fit to the energy derivative of the spontaneous radiation curve S_A°. Errors on the experimental points are purely statistical.

The first data points, shown in Fig. 10, are actually rather scattered and considerably lower than the theoretical curve. A possible explanation, consistent with the accuracy with which it was possible during the present experimental runs to align the laser beam on the circulating electron beam, is that a vertical misalignment between the laser and the e-beam centerlines, of the order of 0.5 to 1 mm, existed. This hypothesis will have to be further investigated. The measurements were performed with a single-mode laser power of .5 ÷ 1 W.

A few runs have been carried out on the third harmonic, λ = 5145 Å and K_{RMS} = 3.5, by lowering the electron resonance energy down to 360 MeV. These data points are also plotted in Fig. 10.

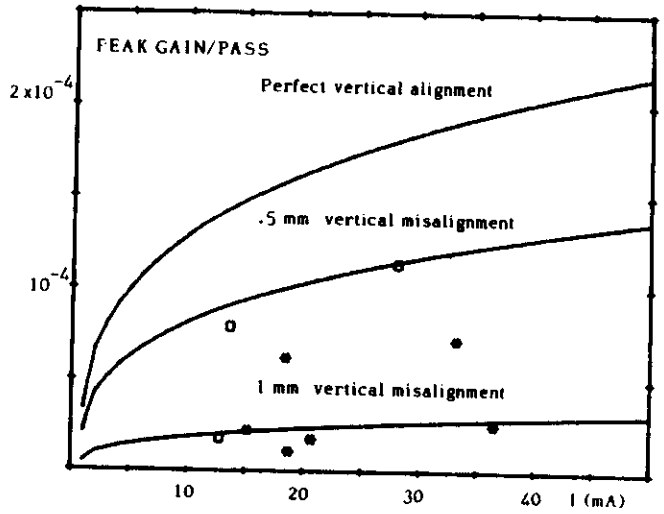

Fig. 10 - Solid curves: Theoretical small signal peak gain/pass for various e-beam and laser beam alignments, on the first harmonic. Stars are experimental points on the first harmonic (K_{RMS} = 3.5, resonance energy E_r = 624 MeV); squares are experimental points on the third harmonic (K_{RMS} = 3.5, E_r = 360 MeV).

The uncertainty in the overlap between the electron and the laser beams, prevents us, at the present stage, from drawing quantitative conclusions on the expected [2),8)] gain increase relative to the first harmonic.

IV - FURTHER DEVELOPMENTS

A number of improvements are foreseen in order to overcome the experimental difficulties encountered in this set of runs; namely:

- To increase the stimulated-to-spontaneous power ratio at the detector input by adding a Fabry-Perot interferometer having a narrow passband around the stimulated frequency.

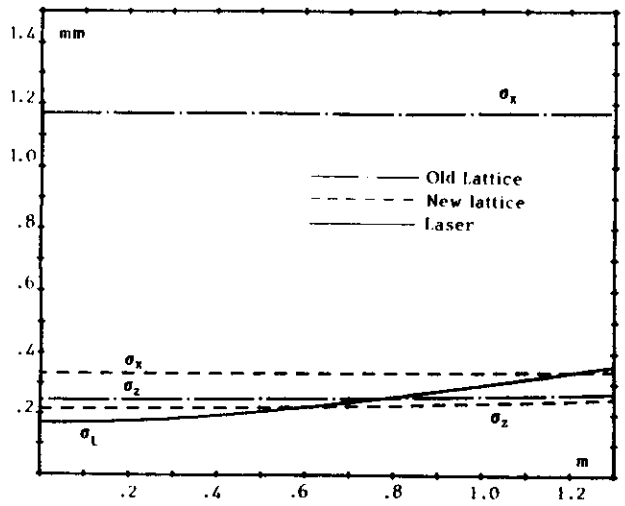

Fig. 11 - Laser beam and electron beam envelopes in the old and the new machine lattice starting from the undulator center.

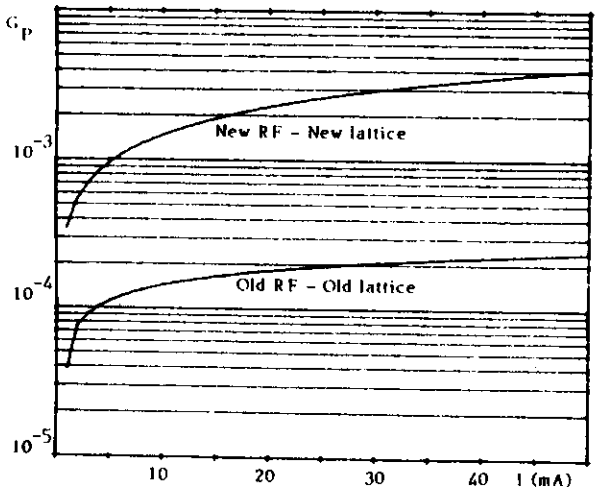

Fig. 12 - Expected peak gain/pass vs. average current on the first harmonic at E_r = 625 MeV, λ = 5145 Å.

We estimate that an additional factor of the order of 20 can be obtained in the spontaneous radiation rejection:

- Improved electron beam and laser beam steering and additional diagnostics are being installed to achieve a more precise alignment between the e-beam and the laser;

- To increase the laser power;

- A new machine lattice[1] with vanishing dispersion in the undulator straight section is being commissioned. The laser and the e-beam envelopes are expected to become those shown in Fig. 11, and to yield a net increase in the filling factor and therefore in the gain figure of the order of a factor of five;

- A 51.4 MHz, 180 kV RF cavity already installed and operating in Adone, but temporarily unavailable during the one week shift in which the present work was carried out, is expected to improve the peak gain by a factor of the order of 2 ÷ 3 (see Fig. 12);

- Other minor improvements on windows giving access to the storage ring vacuum chamber, on the detector circuit, the optics and the accelerator controls for this experiment, are in the works.

In conclusion a gain of some units in 10^{-3}, hopefully sufficient for the operation of an oscillating optical cavity, is expected in the next stage of the experiment.

REFERENCES

1) R. Barbini and G. Vignola, LELA: A free electron laser experiment in Adone, Frascati internal report LNF-80/12 (1980).

2) R. Barbini and G. Vignola, Physics of Quantum Electronics, Vol. 8, p. 235, eds. S.F. Jacobs, G.T. Moore, M.S. Pilloff, M. Sargent III, M.O. Scully and R. Spitzer (Addison-Wesley), 1982.

3) R. Barbini, A. Cattoni, B. Dulach, C. Sanelli, M. Serio and G. Vignola, Nucl. Instr. & Meth. 190, 159 (1981).

4) C. Bazin, M. Billardon, D. Deacon, Y. Farge, J.M. Ortega, J. Pérot, Y. Petroff and M. Velghe, J. Physique-Lettres 41, (1980).

5) R. Barbini et al.: Rivista del Nuovo Cimento, Vol. 4, n. 8 (1981).

6) G. Bazin, M. Billardon, D.A.G. Deacon, P. Elleaume, Y. Farge, J.M.J. Madey, J.M. Ortega, Y. Petroff, K.E. Robinson, M. Velghe, Ref. 2, p. 89.

7) R. Barbini, M. Serio, F. Tazzioli and G. Vignola, Apparato sperimentale per la misura del guadagno ottico nell'esperimento LELA con tecniche di demodulazione sincrona, Frascati internal report LNF-81/70 (1981).

8) W.B. Colson, IEEE J.Q.E., QE-17, 1417 (1981).

IL NUOVO CIMENTO Vol. 81 B, N. 1 11 Maggio 1984

Analytical and Experimental Analysis of the Undulator Radiation at Finite Distance as a Function of the e-Beam Parameters (*).

M. Castellano, N. Cavallo, F. Cevenini, M. R. Masullo
P. Patteri, R. Rinzivillo and S. Solimeno

Istituto Nazionale di Fisica Nucleare, Sezione di Napoli
Istituto di Fisica Sperimentale dell'Università - Napoli

A. Cutolo

Istituto Nazionale di Fisica Nucleare, Sezione di Napoli
Dipartimento di Elettronica dell'Università - Napoli

(ricevuto il 10 Ottobre 1983)

Summary. — The radiation emitted by the linear undulator installed on a straight section of the ADONE storage ring is studied both experimentally and theoretically. In particular, expressions are provided for the field at finite distance, based on the complex Fresnel integral. In addition, several expressions are derived for the average intensity pattern as a function of the electron beam divergence and energy spread. These formulae are used for analysing the spectral and angular patterns of the radiation measured from a distance of 20 m from the undulator origin. The excellent quality of the undulator and the negligible influence on the pattern of the electron beam divergence are confirmed by the satisfactory agreement of the measured radiation field with the computer-generated one.

PACS. 42.55. – Lasing processes.

1. – Introduction.

The importance of studying the spontaneous radiation emitted by bunches of electrons passing through an undulator was recognized soon after the first

(*) Work done in co-operation with the Accelerator Division of I.N.F.N. Adone Facility.

generation of microwaves achieved by MOTZ at Stanford in (1) 1952. Since then, measurements of undulator radiation spanning from microwaves (2) to X-rays (3) have been reported by several groups (4-6). In the years since MADEY and co-workers measured an optical gain by passing a laser beam through the axis of a helical undulator installed on the Stanford SCA accelerator, new interest in the spectral and angular characteristics of these radiation sources sprung up from the necessity of analysing the factors contributing to the reduction of the gain of the free-electron lasers.

Magnetic imperfections in the undulator (*i.e.* deviations from the sinusoidal profile of the magnetic field) can increase the homogeneous line width of the radiation spectrum through electron orbit distortions, thus leading to a reduction of the optical gain when these devices are used for providing the active medium of a FEL oscillator or amplifier. On the other hand, a high gain necessitates a careful design of the electron transport optics for minimizing the deviations in angle and energy of the electrons entering the undulator. These fluctuations induce a change of the average radiation pattern, which can be taken as a measure of the above imperfections of the beam itself. In addition, when the wiggler (used in this paper as a synonym of undulator) is not well designed, the electron trajectory can exhibit some amount of lateral drift which, in turn, produces a dissymmetry of the pattern and a consequent reduction of the gain. The imperfections due to all these factors can be partially removed by finding a good compromise which brings the radiation pattern as close as possible to the ideal one. Reversely, when the magnetic imperfections are practically absent, the angular pattern can be used for measuring the divergence of an electron beam, as originally suggested by ALFEROV and BASHMAKOV (4).

Most FEL oscillators use optical cavities having dimensions comparable with the undulator length, hereafter indicated with L_w. This means that the distribution of the radiation hitting the mirrors depends on the distance from the wiggler centre and, in general, is different from the far-zone pattern. The knowledge of these distributions is essential for studying the steady-state

(1) H. MOTZ, W. THON and R. N. WHITEHURST: *J. Appl. Phys.*, **24**, 826 (1953).
(2) I. A. GRISHAEV, V. I. KOLOSOV, V. I. MYOKOTA, V. I. BELOGLASOV and B. V. YAKIMOV: *Dokl. Akad. Nauk SSSR*, **131**, 61 (1960).
(3) A. I. ALIKHANYAN, S. P. ESIN, K. A. ISPIRYAN, S. S. KAUKANYAN, N. A. KORKHMAZYAN, A. G. OGANESYAN and A. G. TAMANYAN: *JEPT Lett.*, **15**, 142 (1972).
(4) D. F. ALFEROV, YU. BASHMAKOV, K. A. BELOVINZEV, E. G. BESSONOV, P. A. CHERENKOV: *JETP Lett.*, **26**, 385 (1977).
(5) D. A. G. DEACON, K. E. ROBINSON, J. M. J. MADEY, C. BAZIN, M. BILLARDON, P. ELLAUME, Y. FARGE, J. M. ORTEGA, Y. PETROFF and M. F. VELGHE: *IEEE Trans. Nucl. Science*, NS-**28**, 3142 (1981).
(6) D. F. ALFEROV and YU. A. BASHMAKOV: *Spectral-angular features of the radiation of relativistic charged particle beams in undulators*, preprint No. 77, Lebedev Institute (Moscow, 1983) (in Russian).

configuration of the field inside the cavity as a result of the back and forth bouncing of the radiation pulses emitted by the single electron bunches. Consequently, it is important to measure and/or to calculate the field distribution in proximity of the undulator itself. On the other hand, it is worthy noting that for measuring the far field it is necessary in some cases to place the detector at a distance of some hundred metres or in the focus of a mirror: while the former condition cannot be easily satisfied, the latter method is particularly delicate and requires great accuracy in the positioning and scanning of the detector. In these cases it becomes preferable to measure the radiation pattern at finite distance as, by the way, we have done for the Frascati undulator. Finally, the mirror damage by the UV radiation is one of the major problems with the cavities for FEL operating in the visible range. In particular, it is necessary to know the intensity distribution for the higher harmonics at distances corresponding to the resonator mirrors. These examples explain the great interest in the analysis of the undulator radiation at finite distances R_0. This problem has been addressed in ref. (7) by neglecting the effects of the finite distance on the phase distribution of the contributions of the different sections of an undulator. In the present paper it is shown that these phase variations play a major role in modifying the near field along off-axis directions, namely for Fresnel numbers $N_w = \pi L_w^2 \theta^2 / \lambda R_0$ of the undulator seen under the angle θ larger than 0.1. A field representation valid for small and large angles is provided in terms of the complex Fresnel integral.

The present paper reports part of the preliminary work carried out for obtaining laser action from a linear undulator, of the electromagnet type, installed on the ADONE storage ring (8). Almost nothing is said to illustrate the parallel work done for improving the quality of the electron beam (reduction of the beam envelope, shortening of the current bunches, change of the cavity radio frequency from 8.56 MHz to 51.4 MHz, etc.), except for some references to the machine characteristics necessary for evaluating the electron trajectories in the undulator. The undulator comprises 20 periods of 11.6 cm with a gap height of 4 cm and a transverse width of 34.8 cm. It terminates with two half-poles used to adjust the electron trajectories in such a way that there is no net deviation in position and in angle of the electrons at the output of the device. The effective vertical magnetic field on the axis is $B_v = 4950$ G corresponding to a factor $K = 4.82$.

The paper is organized in six sections. The undulator is described in sect. 2, where the electron trajectories are derived analytically. The third section is

(7) Y. HIRAI, A. LUCCIO and L. YU: *J. Appl. Phys.*, **55**, 25 (1984).
(8) R. BARBINI, G. VIGNOLA, S. TRILLO, R. BONI, S. DE SIMONE, S. FAINI, S. GUIDUCCI, M. PREGER, M. SERIO, B. SPATARO, S. TAZZARI, F. TAZZIOLI, M. VESCOVI, A. CATTONI, C. SANELLI, M. CASTELLANO, N. CAVALLO, F. CEVENINI, M. R. MASULLO, P. PATTERI, R. RINZIVILLO, A. CUTOLO and S. SOLIMENO: *J. Phys.* (*Paris*), **44**, C1-1 (1983).

dedicated to the calculation of the radiation pattern in the near zone. The effects due to the electron beam divergence and the energy spread are discussed in sect. 4, where simple formulae are provided for the average intensity per unit frequency and solid angle. The presence of aberrating elements placed on the optical path of the radiation, as, for example, windows separating the storage ring from outside, is analysed in sect. 5. The paper terminates with a description of the spontaneous-radiation measurements in sect. 6.

2. – Undulator characteristics and electron trajectories.

The undulator installed on a straight section of the ADONE storage ring (see fig. 1) has 20 periods with the first and last half-poles excited with a lower current for keeping the electrons at the exit aligned with the machine axis. The main characteristics of this device (see fig. 2) are described in detail in ref. (*) and summarized in table I. It has been designed to have the smallest period ($\lambda_w = 11.6$ cm) to reach short wave-lengths and to give a maximum vertical field $B_y = 4950$ G.

TABLE I.

Undulator period	$\lambda_w = 11.6$ cm
Number of periods	$N = 20$
Length (with clamps)	$L_w = 2.412$ m
Maximum magnetic field on axis	$B_y = 4.95$ kG
Field parameter	$K = 4.825$
Pole height	6.5 cm
Pole length	2.9 cm
Pole width	34.8 cm

The accurate measurement of the magnetic field along the axis and across some sections has shown that the modulus of the integral of the vertical component B_y along the z-axis is less than 1 G × metre when $B_{y(\mathrm{peak})} = 4950$ G. This compensation has been obtained by regulating the excitation of the terminal half-poles and trimming the strength of the single poles. Unfortunately, the undulator becomes rapidly uncompensated when the excitation current is slightly changed.

Since $\boldsymbol{B}$ must satisfy simultaneously the equations $\nabla \times \boldsymbol{B} = \nabla \cdot \boldsymbol{B} = 0$, it is nonuniform on the transverse sections and has a nonvanishing component along

(*) R. BARBINI, A. CATTONI, B. DULACH, C. SANELLI, M. SERIO and G. VIGNOLA: *Nucl. Instrum. Methods*, **190**, 159 (1981).

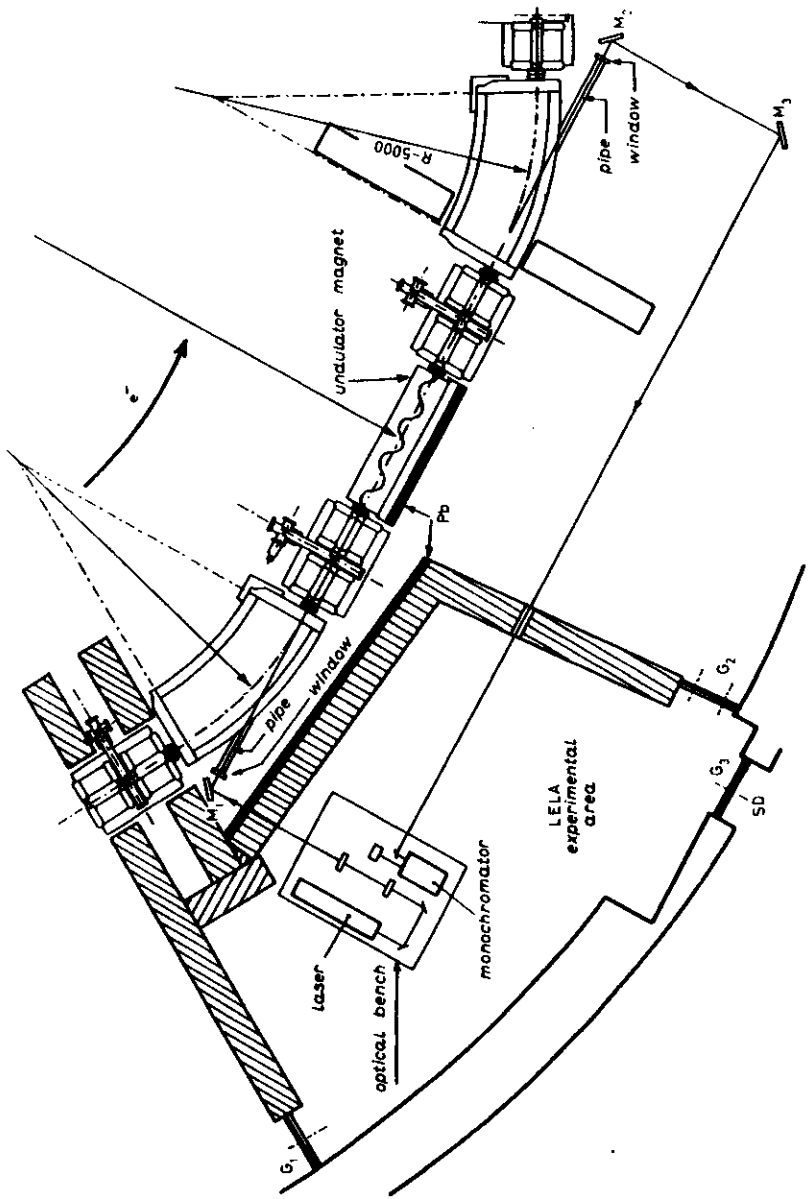

Fig. 1. – Layout of the undulator section of the ADONE storage ring.

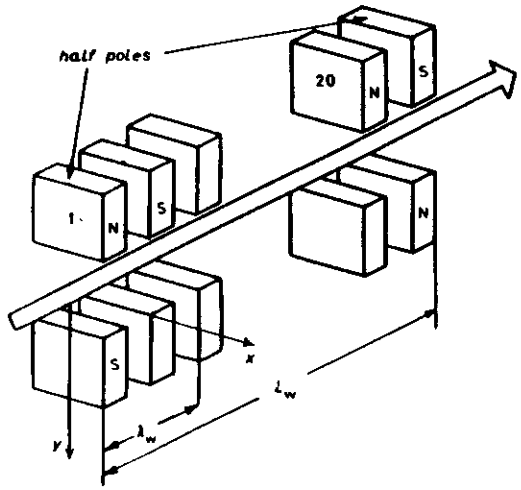

Fig. 2. – Schematic of the 20 periods linear undulator installed on ADONE.

the z-axis. The physically realizable fields cause slow betatron oscillations, which can result in a change of the radiation spectrum with the appearance of side bands. In proximity of the undulator axis (z-axis) the field can be represented with good accuracy by

$$B_x \propto 2Sxy \cos\zeta\,, \tag{1a}$$

$$B_z \propto -\frac{2\pi}{\lambda_w} y \sin\zeta\,, \tag{1b}$$

$$B_y \propto \left\{1 + S(x^2 - y^2) + \frac{1}{2}\left(\frac{2\pi}{\lambda_w}\right)^2 y^2\right\} \cos\zeta\,, \tag{1c}$$

where $\zeta = 2\pi z/\lambda_w$ and S is the sextupole coefficient. The quadrupole coefficient Q can be neglected in view of the extension of the poles in the x-direction. Note that we have oriented the y-axis vertically, parallel to the main component of the magnetic field. This contrasts with the usual convention adopted for the ADONE ring, where the axial co-ordinate is called y and the vertical one z. From the values of B_y measured [8] at different heights y we have inferred that the residual sextupole coefficient is less than $3\cdot10^{-4}$ mm^{-2}.

With good approximation the electron undulates sinusoidally on the (x, z)-plane by describing a trajectory of period λ_w and amplitude $x_m = \sqrt{2}\,\alpha\lambda_w/2\pi$, $\alpha = K/\gamma$ being the maximum deflection angle of an electron of energy γ with $K = eB_y\lambda_w/2\pi mc^2$ the so-called *field parameter*.

Due to the presence of the term Sx^2 in the expression of B_y, the average distance $\langle x_0\rangle$ of the electron from the axis tends to increase with z, namely

$$\langle x_0\rangle = \langle x_0\rangle \cosh\left(\alpha z\sqrt{S}\right)\,. \tag{2}$$

In the present case, $\gamma \simeq 1300$, $K = 4.82$, $z_{out} - z_{in} \simeq 2$ m and $\langle x_0\rangle \simeq \sigma_x = 0.8$ mm (see table II); consequently, the displacement of the electron from the axis at the undulator exit is ~ 4 μm, a quantity which can be neglected in the calculation of the spontaneous radiation.

TABLE II.

Electron energy	E = 625 MeV
Momentum compaction	α_c = 0.064
Fractional energy spread	σ_E = $2.3\cdot10^{-4}$
Averaged invariant	H_M = 0.38 m
Radial emittance	A_x = 0.25 mm mrad
Radial betatron tune	ν_x = 3.2
Vertical betatron tune	ν_y = 3.15
Betatron wave-length	β = 9 m
Off-energy function	η = 2 m
Radial-beam envelope	σ_x = 0.75 mm
Vertical-beam envelope	σ_y = 0.2 mm
Radial divergence	σ_x' = 0.075 mrad
Vertical divergence	σ_y' = 0.08 mrad
Damping partition numbers	$J_z = 2J_x = 2J_y = 1$
Revolution frequency	f_0 = 2.856 MHz
RF frequency	f_{RF} = 8.56 MHz
Number of bunches	n_b = 3

In the y-direction the particles execute betatron types of orbits due to the axial component of the magnetic field which interacts with the oscillations along x. If a particle enters the interaction region, which begins according to the present conventions at $z = 0$, with transverse co-ordinate y_0 and initial velocity β_{0y}, the y-co-ordinate at ζ will read (see, for instance, ref. [10])

$$y_0(\zeta) = y_0\cos\alpha\zeta + \frac{\beta_{0y}\lambda_w}{2\pi\alpha\beta_{0z}}\sin\alpha\zeta \equiv y_0 + \frac{\beta_{0y}\lambda_w}{2\pi\beta_{0z}}\zeta + \delta y_0\,, \tag{3}$$

α being the maximum deflection angle defined above. For $\alpha \simeq 3\cdot10^{-3}$ and $\zeta_w \simeq 40$ ($= 2\pi L_w/\lambda_w$ with L_w the undulator length), we can approximate

[10] C. M. TANG and P. SPRANGLE: in *Physics of Quantum Electronics*, edited by S. F. JACOBS, G. T. MOORE, H. S. PILLOFF, M. SARGENT III, M. O. SCULLY and R. SPITZER, Vol. 9 (Reading, Mass., 1982), p. 267.

eq. (3) with

$$y_s(\zeta) = y_0\left(1 - \frac{1}{2}\alpha^2\zeta^2\right) + \frac{\beta_{0y}z_0}{\beta_{0z}}\left(1 - \frac{\alpha^2\zeta^3}{6}\right). \tag{4}$$

Accordingly, the final displacement induced by B_z is given by

$$\delta y_s = -\frac{1}{2}\alpha^2\zeta_w^2\left(y_0 - \frac{\beta_{0y}L_w}{3\beta_{0z}}\right) \simeq -20\ \mu\text{m}, \tag{5}$$

a quantity much smaller than the oscillation amplitude x_m. We will see in the following that these betatron oscillations give rise to side bands in the spectrum of the spontaneous radiation. However, due to the small value of their amplitude (see eq. (3)), the intensity of these side bands can be practically neglected.

Finally, the effective value of B_y, which determines the amplitude of the x-co-ordinate oscillations, depends on the initial value y_0, the variation being in the Frascati undulator of the order of 10^{-4}. For a discussion of these fluctuations the reader is referred to sect. 4, eq. (50).

On account of the above considerations we can represent the effective field with the linear polarized vector potential $A = \hat{x}A_x$ which depends on ζ as

$$A_x(\zeta) = \frac{\gamma mc^2}{e}a(\zeta) = \frac{\gamma mc^2}{e}\begin{cases} \alpha\eta(1-\cos\zeta) & \text{(half-poles)}, \\ (2\eta-1)\alpha - \alpha\cos\zeta & \text{(undulator)}, \end{cases} \tag{6}$$

η being a parameter accounting for the different strength of the two terminal half-poles with respect to the rest of the undulator (hereafter referred to, for the sake of brevity, as the «undulator»). For a wiggler perfectly compensated (*i.e.* $a(0) = a(\zeta_w) = 0$ and $\int a(\zeta)\,d\zeta = 0$) the coefficient η is equal to $\eta = (N-1)/(2N-1)$, N being the total number of periods (including the half-poles). Equation (6) ensures the continuity of B_y for $\zeta = \pi$ and $\zeta = (2N-1)\pi$, that is at the interfaces of the two half-poles with the undulator. In addition, A_x vanishes identically outside the wiggler: this approximation is justified by the experimental result that the fringe field produced by the Frascati undulator drops to zero so rapidly as to be practically negligible (see the plot of the field along the axis reported in ref. (9)). Note that this approximation is not valid for the undulators built with permanent magnets, where the tail of the fringe field affects notably the electron trajectory (see, for instance, ref. (11)). In the following, we will treat η as a parameter in order to develop expressions of the radiation field valid also for undulators not perfectly compensated. In addition, α will be treated as a fluctuating quantity (independent of γ) in such a way as to account for the effects produced by the random distribution (Gaussian) of the initial values of y_0, which, in turn, slightly modifies the value of the magnetic field in accordance with eq. (1*b*).

(11) A. LUCCIO and S. KRINSKY: in *Physics of Quantum Electronics*, edited by S. F. JACOBS, G. T. MOORE, H. S. PILLOFF, M. SARGENT III, M. O. SCULLY and R. SPITZER. Vol. 8 (Reading, Mass., 1982), p. 181.

2*a*. *Electron trajectories.* – Electrons execute complicated trajectories in three dimensions, which can be conveniently represented analytically by using as independent variable the co-ordinate ζ. In the following, we will derive in the order $t = t(\zeta)$, $x = x(\zeta)$ and $y = y(\zeta)$.

The function $t = t(\zeta)$ can be obtained by integrating the equation (12)

$$\Omega t = \left(1 + \frac{1}{2\gamma^2} + \frac{\beta_{0x}^2 + \beta_{0y}^2}{2}\right)\zeta + \frac{1}{2}\int_0^\zeta a^2(\zeta')\,d\zeta' - \beta_{0x}\int_0^\zeta a(\zeta')\,d\zeta', \tag{7}$$

since $\Omega = 2\pi c/\lambda_w$ and having assumed, without loss of generality, equal to zero the time at which the electron enters the undulator. Now, inserting the r.h.s. of eq. (6) into (7), we obtain

$$\Omega t = C_1(\zeta)\sin\zeta + C_2(\zeta)\sin 2\zeta + C_3(\zeta)\zeta + C_4(\zeta), \tag{8}$$

where the $C_i(\zeta)$ are stepwise functions which remain constant along each half-pole and the undulator. In particular,

$$\left\{\begin{aligned}
C_1 &= \begin{cases} \alpha\eta\beta_{0x} - \alpha^2\eta^2 & \text{(half-poles)}, \\ \alpha\beta_{0x} + \alpha^2(1-2\eta) & \text{(undulator)}, \end{cases} \\
C_2 &= \begin{cases} \frac{1}{8}\alpha^2\eta^2 & \text{(half-poles)}, \\ \frac{1}{8}\alpha^2 & \text{(undulator)}, \end{cases} \\
C_3 &= \begin{cases} 1 + \frac{1}{2\gamma^2} + \frac{\beta_{0x}^2+\beta_{0y}^2}{2} - \alpha\beta_{0x}\eta + \frac{3}{4}\alpha^2\eta^2 & \text{(half-poles)}, \\ 1 + \frac{1}{2\gamma^2} + \frac{\beta_{0x}^2+\beta_{0y}^2}{2} - \alpha\beta_{0x}(2\eta-1) + \frac{\alpha^2}{2}\left[(2\eta-1)^2 + \frac{1}{2}\right] & \text{(undulator)}, \end{cases} \\
C_4 &= \begin{cases} 0 & \text{(1st half-pole)}, \\ -\alpha\pi\beta_{0x}(1-\eta) - \frac{\alpha^2}{2}\pi\left[(2\eta-1)^2 + \frac{1}{2} - \frac{3}{2}\eta^2\right] & \text{(undulator)}, \\ 2(N-1)\pi\left\{\alpha\beta_{0x}(1-\eta) + \frac{\alpha^2}{2}\left[(2\eta-1)^2 + \frac{1}{2} - \frac{3}{2}\eta^2\right]\right\} & \text{(2nd half-pole)}. \end{cases}
\end{aligned}\right. \tag{9}$$

(12) P. LUCHINI, C. H. PAPAS and S. SOLIMENO: *Appl. Phys. B*, **28**, 15 (1982).

Since the undulator field does not vary along the x-direction, we can use the constant of motion

$$p_x - \frac{e}{c} A_x = \text{const} = p_x^{(i)}, \tag{10}$$

where p_x is the x-component of the electron momentum, $p_x^{(i)}$ its initial value and e (> 0) the electron charge, for writing the equation

$$\frac{\mathrm{d}x_e}{\mathrm{d}\zeta} = c(\beta_{ex} - a)\frac{\mathrm{d}t}{\mathrm{d}\zeta} = \frac{c}{\Omega}(\beta_{ex} - a)\left(1 + \frac{1}{2\gamma^2} + \frac{\beta_{ex}^2 + \beta_{ey}^2}{2} + \frac{a^2}{2} - \beta_{ex} a\right). \tag{11}$$

If we retain only those terms of eq. (11) containing combinations of the small quantities β_{ex}, a and γ^{-1} of order not larger than two, we can assume $\mathrm{d}t/\mathrm{d}\zeta = \Omega^{-1}$, so that

$$\frac{\Omega}{c}\{x_e(\zeta) - x_0\} = \beta_{ex}\zeta - \int_0^\zeta a(\zeta')\,\mathrm{d}\zeta' = X_1(\zeta)\sin\zeta + X_3(\zeta)\zeta + X_4(\zeta), \tag{12}$$

where the X_i are stepwise functions constant along each half-pole and the undulator, where they take the following values:

$$\left|\begin{array}{l} X_1 = \begin{cases} \alpha\eta & \text{(half-poles)}, \\ \alpha & \text{(undulator)}, \end{cases} \\ X_3 = \begin{cases} -\alpha\eta + \beta_{ex} & \text{(half-poles)}, \\ (1-2\eta)\alpha + \beta_{ex} & \text{(undulator)}, \end{cases} \\ X_4 = \begin{cases} 0 & \text{(1st half-pole)}, \\ -\alpha\pi(1-\eta) & \text{(undulator)}, \\ -2(N-1)(1-\eta)\alpha\pi & \text{(2nd half-pole)}. \end{cases} \end{array}\right. \tag{13}$$

Finally, $y_e(\zeta)$ is given by eq. (3).

3. – Field radiated by the undulator.

The radiation emitted by relativistic electrons passing through an undulator has been studied by several authors [13-17]. The far-zone pattern relative to a uniform wiggler without half-poles was originally calculated by ALFEROV *et al.* [13] by expressing the Lienard-Wiechert vector potential by means of a series containing Bessel functions and the function $\mathrm{sinc}(x) = \sin\pi x/\pi x$. On the other hand, NIKITIN *et al.* [16,17] have expressed the field by means of the incomplete cylindrical functions.

The radiation of the Frascati undulator is observed from a distance of about 24 m, so that the far-zone formulae cannot be used for a careful representation of the field. In alternative, we have developed an analytic representation in which the function $\mathrm{sinc}(\cdot)$ is replaced by the Fresnel complex integral $F(\cdot)$. Formally, these near-field expressions coincide with those relative to the far field of a tapered undulator [18]. In fact, a uniform wiggler seen from a finite distance looks like a tapered one for what concerns the dependence of the optical path connecting the field point with an electron, on the axial coordinate of the electron itself.

The near-field calculation has been attempted in ref. [7] by manipulating in a suitable way the radiation integral, which contains as integrand a phase factor times a vector function. In particular, these authors have assumed that the phase be proportional to $\hat{n}_0 \cdot r_e$, $\hat{n}_0$ being the unit vector connecting the undulator origin with the field point r and the position vector r_e of the electron. The effects of the finite distance are accounted for by the variation of the vector

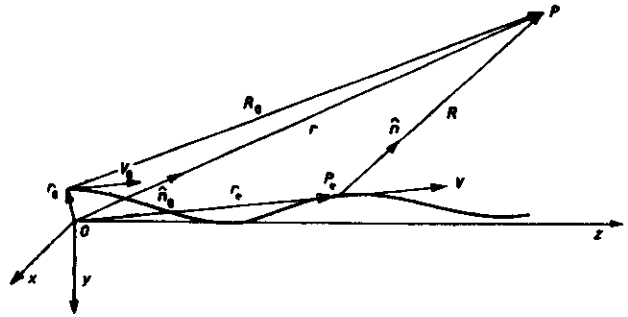

Fig. 3. – Geometry relative to the calculation of the radiation integral.

(13) D. F. ALFEROV, YU. A. BASHMAKOV and E. G. BESSONOV: *Sov. Phys. Tech. Phys.*, **18**, 1336 (1974).
(14) A. HOFFMAN: *Nucl. Instrum. Methods*, **152**, 17 (1978).
(15) C. BAZIN, M. BILLARDON, D. A. G. DEACON, P. ELLAUME, Y. FARGE, J. M. J. MADEY, J. M. ORTEGA, Y. PETROFF, K. E. ROBINSON and M. VELGLIE: in *Physics of Quantum Electronics*, edited by S. F. JACOBS, G. T. MOORE, H. S. PILLOFF, M. SARGENT III, M. O. SCULLY and R. SPITZER, Vol. 8 (Reading, Mass., 1982), p. 89.
(16) M. M. NIKITIN, A. F. MEDVEDEV, M. B. MOISSEEV and V. YA. EPP: *Sov. Phys. Tech. Phys.*, **26**, 350 (1981).
(17) M. M. NIKITIN, A. F. MEDVEDEV, M. B. MOISSEEV, V. YA. EPP and G. K. RASINA: *Sov. Phys. Tech. Phys.*, **26**, 355 (1981).
(18) C. C. SHIH and M. Z. CAPONI: *Phys. Rev. A*, **26**, 438 (1982).

quantity multiplying the phase factor. In addition, in our calculations we include in the phase an additional term quadratic in r_e.

The component at frequency ω of the electric field radiated in free space by a single electron is proportional to the integral [19] (see fig. 3)

$$(14) \qquad I(r) = \frac{i}{\omega}\int_0^T \frac{\hat{n}\times[(\hat{n}-\beta)\times\dot{\beta}]}{(1-\hat{n}\cdot\beta)^2 R(t)} \exp[i\omega(t+R(t)/c)]\,dt\,,$$

having neglected terms proportional to R^{-2}. Here $R(t) = r - r_e(t)$ is the vector connecting the position occupied by the electron at the instant t with the field point r; in addition, $\hat{n}(t) = \hat{R}(t)$, T is the transit time through the undulator and $\beta(t) = \dot{r}_e(t)/c$ is the electron velocity divided by c.

Now, by generalizing eq. (14.66) of ref. [19] to the case in which the field point is at finite distance and $\hat{n}$ depends on t, we obtain with simple algebra and the help of eq. (14.10)

$$(15) \qquad \frac{\hat{n}\times[(\hat{n}-\beta)\times\dot{\beta}]}{(1-\hat{n}\cdot\beta)^2} = \frac{d}{dt}\frac{\hat{n}\times(\hat{n}\times\beta)}{1-\hat{n}\cdot\beta} - \frac{\dot{\hat{n}}\times(\hat{n}\times\beta)+\hat{n}\times(\dot{\hat{n}}\times\beta)}{1-\hat{n}\cdot\beta} - \frac{\dot{\hat{n}}\cdot\beta}{(1-\hat{n}\cdot\beta)^2}[\hat{n}\times(\hat{n}\times\beta)] =$$

$$= \frac{d}{dt}\frac{\hat{n}\times(\hat{n}\times\beta)}{1-\hat{n}\cdot\beta} + \frac{e}{R}\left[\hat{n}\hat{n}\cdot\beta + \frac{\hat{n}-\beta}{1-\hat{n}\cdot\beta} - \frac{\hat{n}-\beta}{(1-\hat{n}\cdot\beta)^2}(1-\beta^2)\right].$$

Consequently, by neglecting the term $O(1/R)$ of eq. (15), replacing the integrand of (14) with the r.h.s. of (15) and integrating by parts, we finally obtain

$$(16) \qquad I = \frac{i}{\omega}\frac{\hat{n}_f\times(\hat{n}_f\times\beta_f)}{(1-\hat{n}_f\cdot\beta_f)R_f}\exp[i\omega(T+R_f/c)] - \frac{i}{\omega}\frac{\hat{n}_0\times(\hat{n}_0\times\beta_0)}{(1-\hat{n}_0\cdot\beta_0)R_0}\exp[i\omega R_0/c] +$$

$$+\int_0^T \frac{\hat{n}\times(\hat{n}\times\beta)}{R(t)}\exp[i\omega(t+R/c)]\,dt + O(1/R^2)\,,$$

where the suffixes 0 and f label quantities referring to the entrance and exit sections of the undulator, respectively. The calculations carried out by using eq. (16) have shown that the end point contributions (the first two terms on the r.h.s. of (16)) are practically negligible. Therefore, these two terms will be omitted in the following expressions.

([19]) J. D. JACKSON: *Classical Electrodynamics* (New York, N. Y., 1962).

When the field point is at a sufficient distance from the undulator, we can approximate $R(t)$ with (see fig. 3)

$$(17) \qquad R(t) = R_0\left(1 + \frac{\tilde{r}_e^2}{R_0^2} - \frac{2}{R_0}\hat{n}_0\cdot\tilde{r}_e\right)^{\frac{1}{2}} \simeq R_0 - \hat{n}_0\cdot\tilde{r}_e + $$

$$+ \frac{1}{2R_0}[(n_{0x}^2+n_{0z}^2)\tilde{x}_e^2 + (n_{0x}^2+n_{0z}^2)\tilde{y}_e^2 + (n_{0x}^2+n_{0y}^2)\tilde{z}_e^2]\left(1+\frac{1}{R_0}\hat{n}_0\cdot\tilde{r}_e\right),$$

where $R_0 = r - \hat{x}x_0 - \hat{y}y_0$ and $\tilde{r}_e = r_e - \hat{x}x_0 - \hat{y}y_0$. For directions close to the z-axis we have

$$(18) \qquad \frac{\omega}{2R_0c}[(n_{0x}^2+n_{0z}^2)\tilde{x}_e^2 + (n_{0x}^2+n_{0z}^2)\tilde{y}_e^2] < \frac{\omega}{2R_0c}(\tilde{x}_e^2+\tilde{y}_e^2) <$$

$$< \frac{\lambda_w^2}{4\pi R_0\lambda}[3.4\alpha^2 + (2\pi N)^2(\beta_{0x}^2+\beta_{0y}^2)] \equiv \frac{1}{10}\frac{R_{min}}{R_0}\,,$$

with the help of eqs. (12) and (13). Thus, for distances R_0 larger than R_{min}, the above contribution to the phase $\varphi(t) \equiv \omega(t + R/c)$ can be neglected. For the Frascati-ADONE FEL replacing $\beta_{0x}^2 + \beta_{0y}^2$ with the squared values of the vertical and radial divergence standard deviations (see table II) and taking into account the parameters of the undulator yield $R_{min} \simeq 6$ m.

Now let us observe that

$$(19) \qquad \frac{\omega}{2R_0c}(n_{0x}^2+n_{0y}^2)x_e^2 < \frac{\pi L_w^2}{R_0\lambda}(n_{0x}^2+n_{0y}^2)_{max} \equiv \frac{1}{10}\frac{R'_{min}}{R_0}\,,$$

the suffix max indicating the maximum deviation of $\hat{n}$ from the z-axis. It is noteworthy that the quantity $N_w \equiv \pi L_w^2(n_{0x}^2+n_{0y}^2)/\lambda R_0$ represents the Fresnel number of the undulator seen from the field point. For off-axis angles less than 1.2 mrad, $L_w = 2$ m and $\lambda = 5000$ Å, we have $R'_{min} = 362$ m. Accordingly, the last contribution to the phase cannot be neglected for the ADONE undulator.

Since the vector $\hat{n}$ is almost coincident with $\hat{s}$, we can write

$$(20) \qquad \hat{n} \simeq \hat{x}\frac{x}{R} + \hat{y}\frac{y}{R} + \left[1 - \frac{1}{2}\left(\frac{x}{R}\right)^2 - \frac{1}{2}\left(\frac{y}{R}\right)^2\right]\hat{z} \simeq$$

$$\simeq \hat{n}_0 + \varepsilon\left(\hat{x}\frac{x}{R_0} + \hat{y}\frac{y}{R_0} - \hat{z}\frac{x^2+y^2}{R_0^2}\right) \simeq \hat{n}_0 + \varepsilon(\hat{x}n_{0x} + \hat{y}n_{0y}) \equiv \hat{n}_0 + \varepsilon n_\perp,$$

having put

$$(21) \qquad \frac{1}{R} = \frac{1}{R_0}(\varepsilon + 1)\,.$$

Consequently, we have

$$\hat{n}\times(\hat{n}\times\beta)=\hat{n}(\hat{n}\cdot\beta)-\beta=\hat{n}_0\times(\hat{n}_0\times\beta)+\varepsilon\{(\hat{n}_0\cdot\beta)\,n_\perp+(n_\perp\cdot\beta)\,\hat{n}_0\}\,. \tag{22}$$

In view of eqs. (12) and (13) $\varepsilon n_\perp\cdot\beta=\varepsilon(\beta_{0x}+\alpha\cos\zeta)n_{0x}+\varepsilon\beta_{0y}n_{0y}$. Since this term contains products of three small quantities, it can be dropped off. In addition, we can put $\hat{n}_0\cdot\beta=1$.

If now we introduce the polarization vectors $\hat{\sigma}=(\hat{n}_0\times\hat{y})/|\hat{n}_0\times\hat{y}|$ and $\hat{\pi}=\hat{\sigma}\times\hat{n}_0$, we can split $\hat{n}\times(\hat{n}\times\beta)$ in two components, namely

$$\begin{aligned}\hat{n}\times(\hat{n}\times\beta)=\frac{1}{\sqrt{1-n_{0y}^2}}\{&(n_{0x}\beta_x-n_{0x}\beta_x-\varepsilon n_{0x})\,\hat{\sigma}+\\&+[n_{0y}(\hat{n}_0\cdot\beta)-\beta_y+\varepsilon n_{0y}]\,\hat{\pi}\}\simeq(f_\sigma+\varepsilon g_\sigma)\,\hat{\sigma}+(f_\pi+\varepsilon g_\pi)\,\hat{\pi}\,,\end{aligned} \tag{23}$$

having put $\beta_z/\sqrt{1-n_{0y}^2}=1$ since β_z differs from unity of the quantity $1/2\gamma^2$, which in our case is of the order of 10^{-6}, while n_{0y} takes values not larger than 10^{-2}. The symbols f and g are defined by

$$\left\{\begin{aligned}&f_\sigma=n_{0x}\frac{\mathrm{d}x_0}{\mathrm{d}z_0}-n_{0x}=n_{0x}(X_1\cos\zeta+X_2)-n_{0x}\,,\\&f_\pi=n_{0y}\left(n_{0x}\frac{\mathrm{d}x_0}{\mathrm{d}z_0}+n_{0y}\frac{\mathrm{d}y_0}{\mathrm{d}z_0}+n_{0z}\right)-\frac{\mathrm{d}y_0}{\mathrm{d}z_0}=\\&\qquad=n_{0y}n_{0x}(X_1\cos\zeta+X_2)+n_{0y}n_{0z}-(1-n_{0y}^2)\frac{\beta_{0y}}{\beta_{0z}}\,,\\&g_\sigma=-n_{0x}\,,\\&g_\pi=n_{0y}\,.\end{aligned}\right. \tag{24}$$

3·1. *σ and π components of the radiation field.* – Let us now split the field integral I defined by eq. (14) into two scalar components,

$$\Omega R_0 I=I_\sigma\hat{\sigma}+I_\pi\hat{\pi}=(I_\sigma^{(\mathrm{hp})}+I_\sigma^{(\mathrm{u})})\,\hat{\sigma}+(I_\pi^{(\mathrm{hp})}+I_\pi^{(\mathrm{u})})\,\hat{\pi}\,, \tag{25}$$

where the quantities labelled hp and u refer, respectively, to the contributions of the half-poles and the undulator. If we plug the r.h.s. of eqs. (23) and (21) into the integral of eq. (16), we obtain

$$I_{\sigma,\pi}^{(\mathrm{hp})}=\left(\int_0^{\pi}+\int_{(2N-1)\pi}^{2N\pi}\right)[(1+\varepsilon)(f_{\sigma,\pi}+\varepsilon g_{\sigma,\pi})]\exp[i\varphi(\zeta)](1+i\varphi_b(\zeta))\,\mathrm{d}\zeta\,, \tag{26}$$

$$I_{\sigma,\pi}^{(\mathrm{u})}=\int_{\pi}^{(2N-1)\pi}[(1+\varepsilon)(f_{\sigma,\pi}+\varepsilon g_{\sigma,\pi})]\exp[i\varphi(\zeta)](1+i\varphi_b(\zeta))\,\mathrm{d}\zeta\,. \tag{27}$$

The phase factor $\exp[i\varphi_b]$ has been approximated with $1+i\varphi_b$ due to the smallness of φ_b, which is, in turn, defined by (cf. eq. (3))

$$\varphi_b(\zeta)=\frac{\omega}{c}n_{0y}\delta y_0\,. \tag{28}$$

On the other hand, the phase $\varphi(\zeta)$ is defined, apart from the inessential factor $(\omega/c)(r-n_{0x}x_0-n_{0y}y_0)=(\omega/c)R_0$, by

$$\begin{aligned}\varphi(\zeta)=\frac{\omega}{c}(R-r+n_{0x}x_0+n_{0y}y_0)-\varphi_b(\zeta)\simeq\\\simeq\frac{\omega}{c}\left[ct-n_{0x}x_0-n_{0y}\beta_{0y}z_0-n_{0x}z_0+\frac{z_0^2}{2R_0}(n_{0x}^2+n_{0y}^2)\right]\equiv\\\equiv\nu(\zeta)\zeta-p(\zeta)\sin\zeta+q(\zeta)\sin2\zeta+r(\zeta)+s(\zeta)\zeta^2\,,\end{aligned} \tag{29}$$

where ν, p, q, r and s are stepwise functions defined by

$$\left\{\begin{aligned}&\nu(\zeta)=\frac{\omega}{\Omega}\begin{cases}\dfrac{1}{2\gamma^2}+\dfrac{3}{4}\alpha^2\eta^2+1-n_{0z}-n_{0x}(\beta_{0x}-\alpha\eta)-n_{0y}\beta_{0y}+\\\qquad+\dfrac{\beta_{0x}^2+\beta_{0y}^2}{2}-\alpha\beta_{0x}\eta & \text{(half-poles)}\,,\\[2ex]\dfrac{1}{2\gamma^2}+\dfrac{\alpha^2}{4}[2(2\eta-1)^2+1]+1-n_{0z}-n_{0x}[\beta_{0x}+\alpha(1-2\eta)]-\\\qquad-n_{0y}\beta_{0y}+\dfrac{\beta_{0x}^2+\beta_{0y}^2}{2}-\alpha\beta_{0x}(2\eta-1) & \text{(undulator)}\,,\end{cases}\\&p(\zeta)=\frac{\omega}{\Omega}\begin{cases}\alpha^2\eta^2+\alpha n_{0x}\eta-\beta_{0x}\alpha\eta & \text{(half-poles)}\,,\\\alpha n_{0x}+(2\eta-1)\alpha^2-\beta_{0x}\alpha & \text{(undulator)}\,,\end{cases}\\&q(\zeta)=\frac{\omega}{\Omega}\begin{cases}\frac{1}{4}\alpha^2\eta^2 & \text{(half-poles)}\,,\\\frac{1}{4}\alpha^2 & \text{(undulator)}\,,\end{cases}\\&r(\zeta)=\frac{\omega}{\Omega}\pi\cdot\begin{cases}0 & \text{(1st half-pole)}\,,\\-\dfrac{\alpha^2}{4}[2(2\eta-1)^2+1-3\eta^2]+\alpha n_{0x}(1-\eta)-\alpha\beta_{0x}(1-\eta) & \text{(undulator)}\,,\\2(N-1)\left\{\dfrac{\alpha^2}{4}[2(2\eta-1)^2+1-3\eta^2]-\alpha n_{0x}(1-\eta)+\right.\\\qquad\left.+\alpha\beta_{0x}(1-\eta)\right\} & \text{(2nd half-pole)}\,,\end{cases}\\&s=\frac{1}{4\pi}\frac{\lambda_u^2}{R_0\lambda}(n_{0x}^2+n_{0y}^2)\,.\end{aligned}\right. \tag{30}$$

In the FEL theory the quantity ν is related to the detuning parameter $\mu = 2\pi(\nu - 1)(N - 1)$, which is a measure of the resonance between the laser wave and the undulator field.

3·2. *Fourier series expansion of the radiation field.* – Now, following ALFEROV *et al.* [13] we shall use the expansion

$$\exp[-ip\sin\zeta + iq\sin 2\zeta] = \sum_{n=-\infty}^{\infty} R_n(p, q)\exp[-in\zeta], \tag{31}$$

where

$$R_n(p, q) = \sum_{k=-\infty}^{\infty} J_k(q)J_{2k+n}(p), \tag{32}$$

for calculating the integrals of eqs. (26) and (27). In particular, by neglecting the small quantity φ_0 and expressing the derivatives dx_0/dz_0 and dy_0/dz_0 appearing in the definition of $f_{\sigma,\pi}$ by means of eq. (12) and eq. (3), we obtain

$$I_\sigma^{(hp)} = \{(\beta_{0x} - \alpha\eta)\hat{L}_1 - n_{0x}\hat{L}_2\} I_0^{(hp)} + \alpha\eta\hat{L}_1 I_1^{(hp)}, \tag{33}$$

$$I_\pi^{(hp)} = \{n_{0y}\hat{L}_2 - \beta_{0y}\hat{L}_1\} I_0^{(hp)}, \tag{34}$$

with the following meaning of the symbols:

$$\hat{L}_1 = 1 + \hat{D} + \hat{D}^2 + \hat{D}^3 \dots, \tag{35}$$

$$\hat{L}_2 = 1 + 2\hat{D} + 3\hat{D}^2 + \dots, \tag{36}$$

$$\hat{D} = -i\frac{\lambda_w}{2\pi R_0}\frac{\partial}{\partial\nu}, \tag{37}$$

while

$$I_0^{(hp)} = \int_{\text{half-poles}} \exp[i\varphi]\,d\zeta = \tag{38}$$

$$= \sum_{n=-\infty}^{\infty} R_n(p, q)\{T(\nu - n, s; 1, 0) + \exp[ir]\,T(\nu - n, s; 2N, 2N - 1)\},$$

where

$$T(\nu - n, s; k_1, k_2) = \int_{\pi k_1}^{\pi k_2} \exp[i(\nu - n)\zeta + is\zeta^3]\,d\zeta = \tag{39}$$

$$= \left(\frac{\pi}{s}\right)^{\frac{1}{3}} \exp\left[-i\frac{(\nu - n)^3}{4s} + i\frac{\pi}{4}\right]\left\{F\left(\pi k_2 s^{\frac{1}{3}} + \frac{\nu - n}{2s^{\frac{1}{3}}}\right) - F\left(\pi k_1 s^{\frac{1}{3}} + \frac{\nu - n}{2s^{\frac{1}{3}}}\right)\right\},$$

$F(x)$ being the complex Fresnel integral,

$$F(x) = \frac{1}{\sqrt{\pi}}\exp[-i\pi/4]\int_x^\infty \exp[it^2]\,dt = \tag{40}$$

$$\underset{x\to 0}{=} \frac{1}{2} + \frac{\exp[-i\pi/4]}{\sqrt{\pi}}\,x\left(1 + i\frac{x^3}{3} - \frac{x^4}{10} - i\frac{x^6}{42} + \dots\right) \sim$$

$$\underset{|x|\to\infty}{\sim} U(-x) + \frac{1}{2\sqrt{\pi}}\frac{1}{x}\exp[i(x^2 + \pi/4)]\left(1 + \sum_{n=1}^{\infty}\frac{3\cdot 5\cdots(2n-1)}{(2x^2 i)^n}\right)$$

with $U(-x)$ the unit step function equal to unity for $x<0$ and zero otherwise.

$I_1^{(hp)} = \int_{\text{half-poles}} \cos\varphi\exp[i\varphi]\,d\zeta$ is given by a series analogous to that of eq. (38) with R_n replaced by $(R_{n-1} + R_{n+1})/2$.

On the other hand, we have for the undulator

$$\exp[-ir^{(u)}]I_\sigma^{(u)} = \{[(1 - 2\eta)\alpha + \beta_{0x}]\hat{L}_1 - n_{0x}\hat{L}_2\} I_0^{(u)} + \alpha\hat{L}_1 I_1^{(u)}, \tag{41}$$

$$\exp[-ir^{(u)}]I_\pi^{(u)} = \{-\beta_{0y}\hat{L}_1 + n_{0y}\hat{L}_2\} I_0^{(u)} \tag{42}$$

with

$$I_0^{(u)} = \sum_{n=-\infty}^{\infty} R_n(p, q)\,T(\nu - n, s; 2N - 1, 1), \tag{43}$$

$$I_1^{(u)} = \tfrac{1}{2}\sum_{n=-\infty}^{\infty}(R_{n-1} + R_{n+1})\,T(\nu - n, s; 2N - 1, 1). \tag{44}$$

The quantities ν, p, q, r and s are defined in eq. (30). In particular, they take different values according to whether they appear in expressions referring to the half-poles or to the undulator.

The effect of the operator $\hat{D}$ on the function T can be easily calculated by taking into account the relation $F'(x) = -\exp[i(x^3 - \pi/4)]/\sqrt{\pi}$. In particular, we have

$$\hat{D}T(\nu - n, s; k_1, k_2) = i\frac{\lambda_w}{4\pi R_0 s}\{+i(\nu - n)\,T + \exp[i[\pi^3 k_2^3 s + \pi k_2(\nu - n)]] - \tag{45}$$

$$- \exp[i[\pi^3 k_1^3 s + \pi k_1(\nu - n)]]\}.$$

Analogous expressions can be easily obtained for the higher-order derivatives.

For what concerns the operators $\hat{L}_1$ and $\hat{L}_2$, the number of terms to include in their series representation depends on the ratio L_w/R_0 and on the accuracy of the field calculation. In fact, these operators are introduced for taking into account the presence of the factor ε in eqs. (26) and (27). If, for example, $L_w/R_0 = 10^{-1}$ and an accuracy of 10^{-3} is requested, the series (35) and (36) can be truncated to the third term.

Before concluding this section it is worthy reporting an expression of the function T valid for values of s such that $s\pi^2(k_2^2 - k_1^2) < 0.1$. In fact, when this condition is satisfied, we can replace the phase factor $\exp[is\zeta^2]$ appearing in the integral of eq. (39) with the expression $1 + is\zeta^2$ and we obtain

$$(46)\quad T(\nu - n, s; k_1, k_2) \simeq \pi(k_2 - k_1)\exp[i\pi(k_1 + k_2)[\nu - n + s(k_1 + k_2)\pi/4]]\cdot \cdot\left\{\operatorname{sinc}\left\{\frac{k_2 - k_1}{2}[\nu - n + \pi s(k_1 + k_2)]\right\} - is\left(\frac{k_2 - k_1}{2}\right)^2 \operatorname{sinc}''\left\{\frac{k_2 - k_1}{2}[\nu - n + \pi s(k_1 + k_2)]\right\}\right\},$$

where $\operatorname{sinc}'' = \mathrm{d}^2 \operatorname{sinc}(x)/\mathrm{d}x^2$.

Finally, we want to discuss qualitatively the contribution of the betatron phase φ_β, defined by eq. (28), to the radiation integrals (26) and (27). If we consider the expression of φ_β in terms of δy_β, we can write

$$(47)\quad i\varphi_\beta = \frac{\omega}{2c}\left(iy_0 + \frac{\beta_{0y}\lambda_w}{2\pi\alpha\beta_{0z}}\right)\exp[i\alpha\zeta] + \frac{\omega}{2c}\left(iy_0 - \frac{\beta_{0y}\lambda_w}{2\pi\alpha\beta_{0z}}\right)\exp[-i\alpha\zeta] - \frac{\omega}{c}\frac{\beta_{0y}\lambda_w}{2\pi\alpha\beta_{0z}}\zeta - \frac{\omega}{c}y_0 .$$

Now, when the first two terms on the r.h.s. of (47) are multiplied by $\exp[i\varphi]$, they produce a shift of the normalized frequency ν which becomes, respectively, equal to $\nu + \alpha$ and $\nu - \alpha$, a circumstance which amounts to the introduction in the spectrum of two side bands shifted by α, which cannot be isolated since they are immersed in the relatively broad line of the fundamental harmonic.

4. – Influence of the energy spread, divergence and finite cross-section on the radiation pattern.

As in other electronic devices, electrons interact most efficiently with waves when the spread in the particle parameters is small. In correspondence of the undulator the ADONE ring is characterized by a betatron wave-length of 9 m (see table II). Correspondingly, the other two Twiss parameters ([20]) are, respectively, equal to $\gamma = 0.1\ \mathrm{m}^{-1}$ and $\alpha = 0.1$. On the other hand, the radial emittance is equal to $A_x = 0.25$ mm mrad. As a consequence, the distribution function of the initial values of x_0 and β_{0x} at the undulator entrance reads, in

([20]) A. RENIERI: in *Proc. S.I.F.*, Course LXXIV, edited by C. PELLEGRINI (Amsterdam, 1981), p. 414.

the absence of energy fluctuations,

$$(48)\quad f(x_0, \beta_{0x}) = 4\exp[-12.5(0.1x_0^2 + 0.2x_0\beta_{0x} + 9\beta_{0x}^2)],$$

where we have expressed x_0 in mm and β_{0x} in mrad. In view of the small coefficient (0.2) of the term $x_0\beta_{0x}$, we can in first approximation neglect the coupling of the x_0 co-ordinate fluctuation with that of β_{0x}.

Since the off-energy function η is different from zero ($\eta = 2m$), we must take into account the energy spread contributions $\sigma_{x\beta}$ and $\sigma'_{x\beta}$ to the radial beam envelope and divergence, respectively, so that we have (see ref. ([20]), eqs. (2.97) and (2.98))

$$(49)\quad \begin{cases} \sigma^2_{x(\mathrm{tot})} = \sigma_\nu^2\left(\eta^2 + \dfrac{J_x}{J_z}H_M\beta\dfrac{1}{1+\delta}\right), \\ \sigma'^2_{x(\mathrm{tot})} = \sigma_\nu^2\left(\eta'^2 + \dfrac{J_x}{J_z}H_M\gamma\dfrac{1}{1+\delta}\right), \end{cases}$$

where σ_ν is the fractional energy spread ($\sigma_\nu = 2.3\cdot10^{-4}$), δ is the coupling coefficient between radial and vertical betatron oscillations ($\delta \simeq 0.1$), J_x and J_z are the damping partition numbers ($J_x = 2$, $J_z = 1$) and H_M is the Courant-Snyder invariant averaged along the bending magnets ($H_M = 0.38$ m). Using eq. (49a), we obtain a beam envelope $\sigma_{x(\mathrm{tot})} \simeq 0.73$ mm which agrees with the measured radial width.

The calculated radial and vertical beam divergences are almost equal to 0.085 and 0.075 mrad, respectively. Since they are much less than the angular width of the radiation pattern, which is, in turn, approximately equal to 0.6 mrad, we are inclined to expect that the beam divergence does not affect notably the radiation pattern. To test this hypothesis, we have calculated the average intensity pattern for a Gaussian distribution of the transverse velocity for different values of the divergence ranging from 0.05 to 0.5 mrad (see fig. 4). In so doing we have found that the angular and spectral patterns begin to become distorted for divergences of the order of 0.4 mrad. In addition, the relative line width of the fundamental harmonic of the undulator radiation is of the order of $1/N = 5\%$. On the other hand, the fractional energy spread of the ADONE beam is two orders of magnitude less than this value. Consequently, we expect a small influence on the radiation pattern.

The initial co-ordinate y_0 of the electron influences indirectly the radiation pattern through the variation of the parameter K. In fact, we have shown in eq. (1c) that the magnetic field B_y increases quadratically with the co-ordinate y. Consequently, a fluctuation of y_0 having variance σ_y corresponds to a standard deviation of K approximately equal to

$$(50)\quad \sigma_K = \frac{1}{2}\left(\frac{2\pi\sigma_y}{\lambda_w}\right)^2 \simeq 10^{-4}.$$

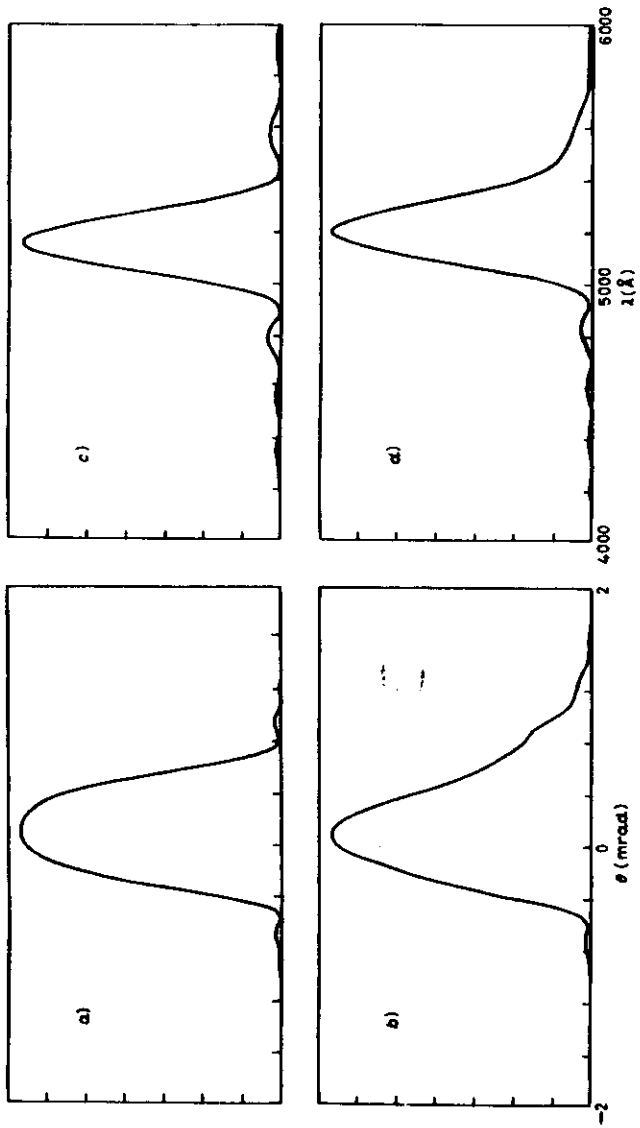

Fig. 4. – Angular (*a*), *b*)) and spectral (*c*), *d*)) intensity distribution averaged with respect to a Gaussian distribution of the transverse velocity of the electron entering the undulator. Plots *a*) and *c*) refer to a divergence of 0.05 mrad, while *b*) and *d*) are relative to a divergence of 0.5 mrad. Note that in the former case the patterns are similar to those calculated for zero divergence (see, for instance, fig. 7*a*)), while in the latter one the modifications become particularly evident in the side lobes with the main lobe appearing more pointed near the peak. The asymmetry of the angular pattern is due to the presence of the half-poles which induce a slight twisting of the trajectory.

4·1. *Effects of the* e*-beam parameter fluctuations on the spectrum of the fundamental harmonic.* – Let us consider for simplicity the far field relative to the horizontal plane ($n_{0x} = 0$) and to frequencies close to the fundamental harmonic. Under these assumptions the contribution of I_π is missing and the series of eqs. (43) and (44) reduces to the terms $n = 1$. On the other hand, the function $T(\nu - 1, s; 2N - 1, 1)$ is given by $2\pi N \exp[i2\pi N(\nu - 1)] \operatorname{sinc}(N - 1)(\nu - 1)$ (see eq. (46)). Accordingly, by neglecting the contribution of the two half-poles, we obtain

$$(51) \qquad I^2 \simeq \alpha^2\pi^2 N^2 \left\{R_0 + R_2 - 2\frac{R_1}{\alpha}(n_{0x} - \beta_{0x})\right\}^2 \operatorname{sinc}^2(N-1)(\nu-1) .$$

It is worth noting that, for n_{0x} and β_{0x} sufficiently small, the functions ν, R_0, R_1 and R_2 reduce, respectively, to

$$(52) \qquad \nu = \frac{\lambda_w}{\lambda}\left\{\frac{1}{2\gamma^2}\left(1 + \frac{K^2}{2}\right) + \frac{1}{2}\left[(n_{0x} - \beta_{0x})^2 + (n_{0y} - \beta_{0y})^2\right]\right\},$$

$$(53) \qquad R_0(p, q) \simeq J_0(q)J_0(p) \simeq J_0(q)(1 - \tfrac{1}{4}p^2) \underset{K\to 0}{\simeq} 1 - \tfrac{1}{4}p^2 ,$$

$$(54) \qquad R_1(p, q) \simeq [J_0(q) + J_1(q)]J_1(p) \simeq [J_0(q) + J_1(q)]\tfrac{1}{2}p \underset{K\to 0}{\simeq} \tfrac{1}{2}p ,$$

$$(55) \qquad R_2(p, q) \simeq -J_1(q)J_0(p) \simeq -J_1(q)(1 - \tfrac{1}{4}p^2) \underset{K\to 0}{\simeq} -\tfrac{1}{2}q(1 - \tfrac{1}{4}p^2) .$$

By inserting the limit expressions of R_i for $K \to 0$ into eq. (51), we shall obtain the expression of the intensity used by ALFEROV *et al.* in ref. (6) (cf. eq. (11) of their paper). For our undulator the factor q is equal to 0.46 and we cannot use their approximate expression of the spectrum, so that in the following we will refer directly to eq. (51) by omitting the inessential factor $\alpha^2\pi^2N^2$. On the other hand, since in our case the intensity is slightly affected by the fluctuation of the beam parameters, we shall calculate the average value of the intensity for given direction and frequency by approximating the fluctuations with the first- and second-order differentials of the intensity calculated with respect to the parameters ν, p and q. In particular, by indicating with $\langle\cdot\rangle$ the average with respect to the variables β_{0x}, β_{0y}, K and γ and with I_0^2 the value in the absence of fluctuations, we have for $u = K, \gamma$,

$$(56) \qquad \sigma_u^{-2} < I^2 - I_0^2 >_u = \frac{1}{2}\frac{\mathrm{d}^2}{\mathrm{d}u^2} I^2\Big|_{u=0} \propto Q^2N^2(\operatorname{sinc}'^2 + \operatorname{sinc}\operatorname{sinc}'')\nu_{,u}^2 +$$
$$+ 2NQ(Q_{,u}p_{,u} + Q_{,q}q_{,u})\operatorname{sinc}\operatorname{sinc}'\nu_{,u} +$$
$$+ [(Q_{,p}^2 + QQ_{,pp})p_{,u}^2 + (Q_{,q}^2 + QQ_{,qq})q_{,u}^2 + 2(Q_{,p}Q_{,q} + Q_{,pq})p_{,q}q_{,u}]\operatorname{sinc}^2 ,$$

having indicated with $a_{,u}$ the quantity $\mathrm{d}a/\mathrm{d}x$. The expressions of the derivatives and the symbols appearing in (56) are given in the appendix. For $u = \beta_{0x}$

we must include in the r.h.s. of (56) the following term:

$$(57)\qquad \left(\frac{4}{\alpha^2}R_1^2 - 4\,\frac{\omega}{\Omega}R_1Q_{,\nu}\right)\operatorname{sinc}^2 + N\,\frac{\omega}{\Omega}\left(Q^2 - 8\,\frac{n_{0\nu}}{\alpha}QR_1\right)\operatorname{sinc}\operatorname{sinc}'\,.$$

For what concerns the fluctuations of $\beta_{0\nu}$, we can show that

$$(58)\qquad \sigma_\nu'^{-2}\langle I^2 - I_0^2\rangle_{\beta_\nu} = N\,\frac{\omega}{\Omega}Q^2\operatorname{sinc}\operatorname{sinc}'\,.$$

In particular, along the undulator axis,

$$(59)\qquad \langle I^2\rangle(Q^2 + A_{\beta_x}\sigma_x'^2 + A_\gamma\sigma_y^2 + A_E\sigma_E^2)\operatorname{sinc}^2 + (B_{\beta_x}\sigma_x'^2 + B_{\beta_y}\sigma_y'^2 + B_\gamma\sigma_y^2 + B_E\sigma_E^2)\operatorname{sinc}\operatorname{sinc}' + (C_\gamma\sigma_y^2 + C_E\sigma_E^2)(\operatorname{sinc}^2 + \operatorname{sinc}\operatorname{sinc}')$$

with the meaning of the symbols defined in the appendix. In particular, note that the term $Q^2\operatorname{sinc}^2$ represents the intensity in the absence of fluctuations.

For the ADONE undulator the quantities σ_x', σ_y', σ_γ and σ_E are of the same order of magnitude (10^{-4}), so that the weight of the terms of (59) depends on the coefficients A, B, C. From the values reported in the appendix (see eqs. (A.18) through (A.25)) eq. (59) reduces to

$$(60)\qquad \begin{aligned}\langle I^2\rangle &= (Q^2 + A_{\beta_x}\sigma_x'^2)\operatorname{sinc}^2 + (\sigma_x'^2 + \sigma_y'^2)B_{\beta_{1,\nu}}\operatorname{sinc}\operatorname{sinc}' + \\ &+ \sigma_y^2 C_\gamma(\operatorname{sinc}'^2 + \operatorname{sinc}\operatorname{sinc}') = \\ &= (0.52 - 8.4\cdot10^4\sigma_x'^2)\operatorname{sinc}^2 + 2.8\cdot10^6(\sigma_x'^2 + \sigma_y'^2)\operatorname{sinc}\operatorname{sinc}'\,.\end{aligned}$$

The above expression confirms the slight variation of the intensity spectrum, so that we are allowed to neglect the fluctuations of the factors appearing inside eq. (51) with the exception of the $\beta_{0\nu}$ which multiplies the function R_1 and the term $(\beta_{0x}^2 + \beta_{0y}^2)/2$ which appears in the definition of ν.

4·2. *Angular pattern of the fundamental harmonic for the frequency relative to the maximum intensity along the axis.* – When we consider the frequency for which $\nu = 1$ along the axis, eq. (52) simplifies into

$$(61)\qquad \nu = 1 + (\xi - \bar\beta_x)^2 + \bar\beta_y^2$$

with $\xi = \gamma n_{0\nu}/(1 + K^2/2)^{\frac{1}{2}}$ and $\bar\beta_{x,y} = \gamma\beta_{0x,0y}/(1 + K^2/2)^{\frac{1}{2}}$. In addition, taking into account eqs. (53)-(55), we can write eq. (51) in the form

$$(62)\qquad I^2 \propto (J_0(q) - J_1(q))^2[1 - 2A(\xi - \bar\beta_x)^2]\operatorname{sinc}^2 N[(\xi - \bar\beta_x)^2 + \bar\beta_y^2]\,,$$

where $A = 2[J_0(q) + J_1(q)]/[J_0(q) - J_1(q)]$. Next, averaging with respect to $\bar\beta_x$ and $\bar\beta_y$ yields

$$(63)\qquad \frac{\langle I^2\rangle}{I^2_{(\xi=0)}} = (1 - 2A\xi^2)\operatorname{sinc}^2 N\xi^2 + 2\Delta\cdot\left\{-A + \frac{1}{4}(1 - 2A\xi^2)\,\frac{1}{\xi}\,\frac{\mathrm{d}}{\mathrm{d}\xi}\,\xi\,\frac{\mathrm{d}}{\mathrm{d}\xi} - 2\xi\,\frac{\mathrm{d}}{\mathrm{d}\xi}\right\}\operatorname{sinc}^2 N\xi^2 \equiv f(\xi) + 2\Delta g(\xi)\,,$$

where $\Delta = \sigma'^2\gamma^2/(1 + K^2/2)$.

The modification of the angular pattern can be evaluated by measuring the momenta of the distribution $f + 2\Delta g$ for $\xi > 0$. Since the intensity profile can be measured accurately only in the main lobe, we find convenient to analyse the quantities

$$(64)\qquad \langle\!\langle\xi^2\rangle\!\rangle \equiv \frac{\int_0^{1/\sqrt{N}}\xi^2(f + 2\Delta g)\,\mathrm{d}\xi}{\int_0^{1/\sqrt{N}}(f + 2\Delta g)\,\mathrm{d}\xi} = \frac{1}{N}\,\frac{NI_2 - 2AI_4 + 2\Delta\{-11ANI_2 + 12I_2 + \frac{1}{2}N^2I_0\}}{NI_0 - 2AI_2 + \Delta\{-3ANI_0 + 4NI_0 - 0.84N^2\}}\,,$$

$$(65)\qquad \langle\!\langle|\xi|\rangle\!\rangle = \frac{1}{N^{\frac{1}{2}}}\,\frac{NI_1 - 2AI_3 + 2\Delta\{-3NAI_1 + 6N^2I_3\}}{NI_0 - 2AI_2 + \Delta\{-3ANI_0 + 4NI_0 - 0.84N^2\}}\,,$$

where $I_n = \int_0^1 \eta^n \operatorname{sinc}^2\eta^2\,\mathrm{d}\eta$. In particular, $I_0 = 0.651$, $I_1 = 0.226$, $I_2 = 0.109$, $I_3 = 0.0617$, $I_4 = 0.0382$. In our case, $A = 3.24$, $\Delta = 8.6\cdot10^{-4}$ for $\sigma' = 8\cdot10^{-5}$ and $\gamma = 1300$, so that

$$(66)\qquad \begin{cases}\langle\!\langle\xi^2\rangle\!\rangle = 7.8\cdot10^{-3}(1 + 124\Delta)\,,\\ \langle\!\langle|\xi|\rangle\!\rangle = 7.5\cdot10^{-3}(1 + 28\Delta)\,,\\ \dfrac{[\langle\!\langle\xi^2\rangle\!\rangle - \langle\!\langle|\xi|\rangle\!\rangle^2]^{\frac{1}{2}}}{\langle\!\langle|\xi|\rangle\!\rangle} = 0.64(1 + 118\Delta)\,.\end{cases}$$

It is noteworthy that even for a so small beam divergence the standard deviation of the pattern aperture is about 10% larger than in the ideal case.

4·3. *Variation of the first harmonic central frequency with the angle.* – For calculating the frequency which maximizes the intensity for a given direction, we note preliminarly that for an electron entering axially the peak of the far field corresponds to the condition $\nu = 1$. In this case, if we indicate with $u = \lambda/\lambda_0$ the wave-length normalized to $\lambda_0 = \lambda_u(1 + K^2/2)/2\gamma^2$, at the cen-

tre of the spectrum u reads

$$u = 1 + \xi^2 . \tag{67}$$

For a divergent beam and a finite observation distance the above relation will be modified. However, we can expect that the corresponding value of ν will still be close to unity.

As a preliminary step let us note that the field can be written in the form

$$I_e \propto \{1 - A(\xi - \bar{\beta}_x)^2 + [1 - A(2\xi - \bar{\beta}_x)(\xi - \bar{\beta}_x)]\,\bar{D}\}\,T , \tag{68}$$

A being the same parameter introduced in eq. (62).

If we assume $s \ll 1$, take into account that in proximity of the peak $\nu \simeq 1$ and use the centre of the undulator as the origin of our co-ordinates, we can express the function T in the form

$$T \propto \int_{-\pi N}^{\pi N} \exp\left[i(\nu - 1)\zeta + is\zeta^2\right] d\zeta \simeq 2\pi N \left[1 - \frac{\pi^2 N^2}{6}(\nu - 1)^2 + i\frac{\pi N}{6}\frac{L_w}{R_e}\frac{\xi^2}{u}\right]. \tag{69}$$

Consequently, inserting the r.h.s. of eq. (69) into (68), we obtain

$$|I|^2 \propto -(\nu - 1)^2\left[1 - \frac{C^2}{12}\left(\frac{L_w}{R_e}\right)^2\right] + \frac{C}{6}\left(\frac{L_w}{R_e}\right)^2(\nu - 1) + \text{const} , \tag{70}$$

since $C = [1 - A(2\xi - \bar{\beta}_x)(\xi - \bar{\beta}_x)]/[1 - A(\xi - \bar{\beta}_x)^2]$.

Next, averaging $\nu = u^{-1}[1 + (\xi - \bar{\beta}_x)^2 + \bar{\beta}_y^2]$ and ν^2 with respect to $\bar{\beta}_x$ and $\bar{\beta}_y$, neglecting the fluctuations of C and equating to zero the derivative of the average intensity with respect to u, we finally obtain after some calculations

$$u = 1 - 2\Delta - \frac{C}{12}\left(\frac{L_w}{R_e}\right)^2 + \xi^2(1 + 8\Delta) . \tag{71}$$

Now, if we redefine u by replacing λ_e with the central frequency relative to the axis, the above equation becomes

$$u = 1 + \xi^2\left(1 + 10\Delta + \frac{C}{12}\left(\frac{L_w}{R_e}\right)^2\right). \tag{72}$$

Accordingly, the finite distance and the divergence induce a change of the central frequency which can be accounted for as being equivalent to an increase of the observation angle. For the ADONE undulator the variation is of the order of 8.10^{-3} and is due almost exclusively to the beam divergence.

5. – Influence of a deformed window on the radiation pattern.

As can be seen from fig. 1 special vacuum chambers have been fixed on the in-going bending magnets of the ring before and after the undulator with glass windows permitting the passage of the spontaneous radiation. Under the action of the external pressure the exit window warps and the relative normal displacement w reads [21]

$$w(\varrho) = -\frac{P}{8D}(a^2 - \varrho^2)\left(\frac{5 + \sigma}{1 + \sigma}a^2 - \varrho^2\right) \simeq \frac{1}{2R_w}\left(\varrho^2 - \frac{5 + \sigma}{6 + 2\sigma}a^2\right), \tag{73}$$

where a (cm) is the window radius, P (1000 g/cm^2) is the external pressure, $R_w = 4D(1 + \sigma)/a^2P(6 + 2\sigma)$ is the curvature radius at the window centre and

$$D = \frac{2}{3}\frac{Eh^3}{1 - \sigma^2} , \tag{74}$$

E being the Young modulus ($\simeq 7.45 \cdot 10^6$ g/cm^2 for glass), h (cm) the window thickness and σ the Poisson's ratio ($\simeq 0.2$ for glass).

For the presence of the deformed window the distance $R(t)$ appearing in eq. (14) must be redefined in order to include a small contribution due to the

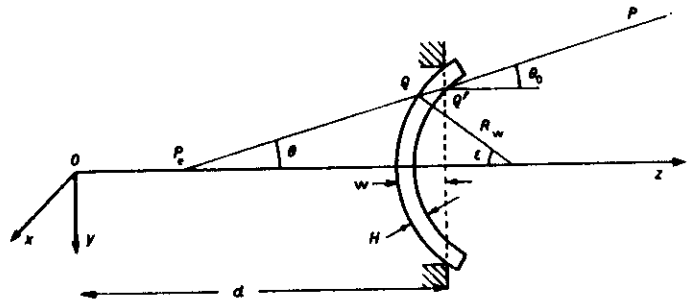

Fig. 5. – Schematic of the optical path $[P_eP]$ connecting the electron at P_e with the field point P through a deformed window.

additional delay produced by the window. This quantity can be easily calculated in the paraxial approximation. In fact, with reference to fig. 5 we can show that the optical path connecting a generic undulator point P_e with the field point P, supposed to be at infinity, is given, apart from an inessen-

[21] L. LANDAU and E. LIFCHITZ: *Théorie de l'elasticité* (Moscou, 1967).

tial additive constant, by

$$(75)\qquad [P_0P] = [P_0Q] + [QQ'] + [Q'P] = (d - z_0)\left(1 + \frac{\theta^2}{2} + \frac{d - z_0}{2R_w}\theta^2\right) + \\ + h n\left[1 + \frac{(\theta + \varepsilon)^2}{2n^2}\right] + \left\{R_0 - (d - z_0)\theta\theta_0 - \left(1 - \frac{\theta_0^2}{2}\right)\cdot \right. \\ \left. \cdot\left[d + \frac{(d - z_0)^2\theta^2}{2R_w} + \frac{h^2}{2R_w}\left[1 + \frac{1}{2}\left(\frac{\theta + \varepsilon}{n}\right)^2\right]^2\left[1 - \frac{1}{2}\left(\varepsilon - \frac{\theta + \varepsilon}{n}\right)^2\right]\right]\right\},$$

n being the refractive index of the window and $\varrho \simeq (d - z_0)\theta$ the distance of Q from the z-axis. The angles θ and ε are, respectively, given by

$$(76)\qquad \theta = \theta_0\left(1 - \frac{h}{R_w}\frac{R_w + d - z_0}{R_w}\right),$$

$$(77)\qquad \varepsilon = \frac{dw}{d\varrho} = \frac{\varrho}{R_w}\left(1 - \frac{2\varrho^2}{3a^2}\right)$$

with $\theta_0 = (n_{0x}^2 + n_{0y}^2)^{\frac{1}{2}}$. We observe that for glass $R_w/h \simeq 3.7 \cdot 10^4 (h/a)^2$, so that h/R_w is a so small quantity to make the difference between θ and θ_0 totally negligible (cf. eq. (76)). In addition, eq. (75) reduces to

$$(78)\qquad [P_0P] = -z_0\left[1 - \frac{\theta_0^2}{2}\left(1 - \frac{2h}{nR_w}\right)\right] + \text{additional terms}.$$

In accordance with the above expression the deformed window induces a small broadening of the angular pattern which can be taken into account by replacing θ_0 with $\theta_0' = \theta_0(1 - h/nR_w)$. In our case, $h \simeq 0.3$ cm, $a \simeq 5$ cm, so that the presence of the window is imperceptible.

6. – Experimental results.

As a preliminary test of the undulator performance the radiation pattern was observed at a distance of 14.5 m from the exit window. The regular circular shape of the iris was used as a reference for the fine alignment of the electron beam with respect to the undulator axis.

The radiation pattern was successively measured several times by placing a 0.24 m grating monochromator fitted with a 10 stages RCA 4832 photomultiplier, placed at a distance of 23 m from the centre of the undulator (see fig. 1). An achromatic microscope objective 10× was placed near the input slit of the monochromator for matching the almost collimated undulator beam to the monochromator numerical aperture, in such a way as to obtain a resolution of 10 Å. A diaphragm of 1 mm diameter was placed on the back side of the objective for obtaining an angular resolution of $5 \cdot 10^{-3}$ mrad.

The spectral response of the system monochromator+photomultiplier was measured by means of a calibrated tungsten lamp (Osram type 17/W, $T_{max} = 800$ °C) of known spectral radiant emittance and fed with a current generator stabilized to 10^{-3}. The reflectivity of the mirrors placed along the optical path was measured with a reflecting spectrophotometer in the range (400÷700) nm. The overall spectral response of the apparatus is plotted in fig. 6.

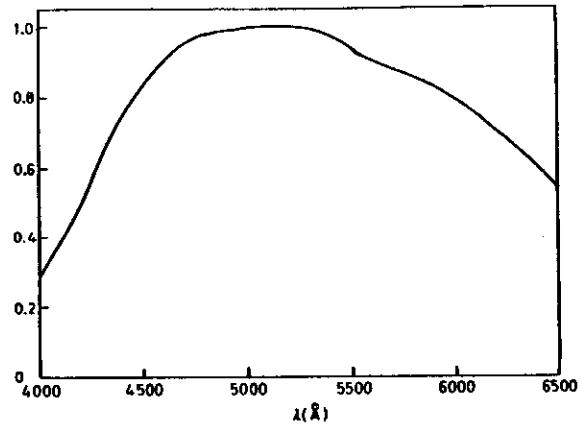

Fig. 6. – Overall transmittance of the apparatus used for measuring the spontaneous radiation. It includes the response of the photomultiplier, the monochromator efficiency and the mirror reflectance.

The anodic current of the photomultiplier was sent to the control and data acquisition PDP 11/40 computer, located in a remote control room, by converting the current signal into a frequency by means of Camac moduli. The nonlinearity of the system in the whole measurement range was found negligible.

The radiation was measured by translating the whole apparatus in steps of 0.125 mrad in the horizontal direction and 0.25 mrad vertically with a total excursion of (3×3) mrad[2]. For each direction the monochromator frequency was scanned from 400 to 650 nm in steps of 10 nm, for both the fundamental and the third harmonic. Altogether 7200 points (direction+frequency) were measured and recorded. All movements were actuated by means of stepping motors driven by a PDP computer through Camac circuits. A complete description of the control system will be published elsewhere ([22]).

([22]) M. CASTELLANO, N. CAVALLO, F. CEVENINI and P. PATTERI: *A remote control system for the LELA experiment* (submitted to *Nucl. Instrum. Methods*).

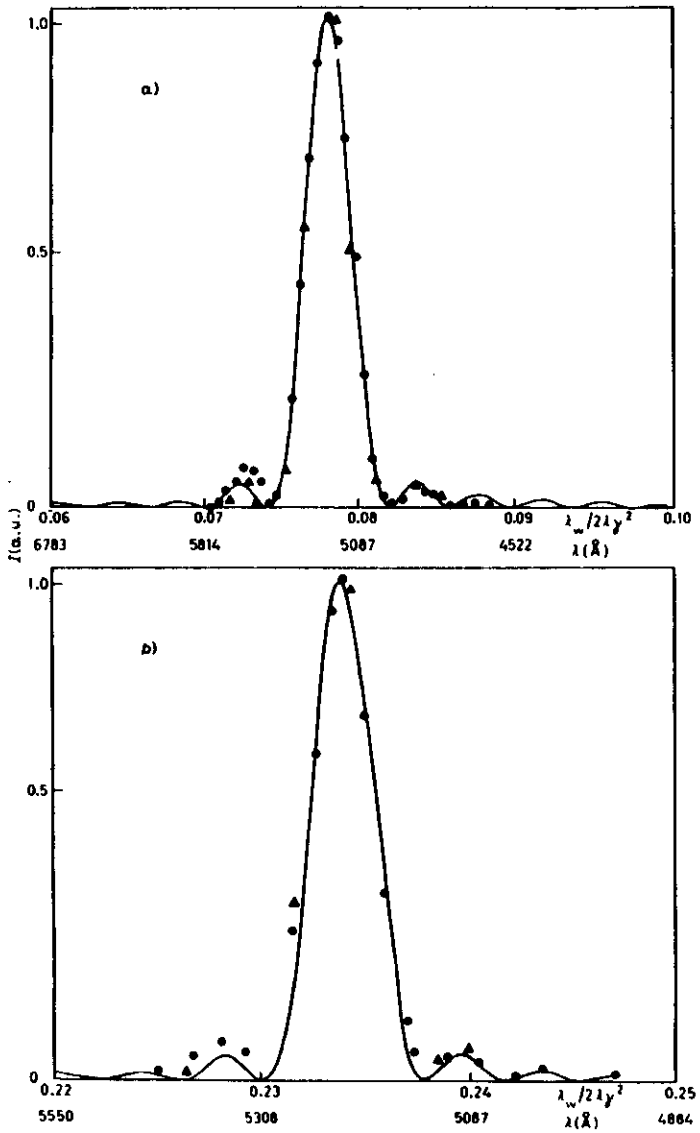

Fig. 7. – Spectrum of the light emitted in the forward direction by 620 MeV (curve *a*), fundamental harmonic) and 368 MeV (curve *b*), third harmonic) electrons. The experimental points are relative to the angular (▲) and spectral (●) scanning, respectively.

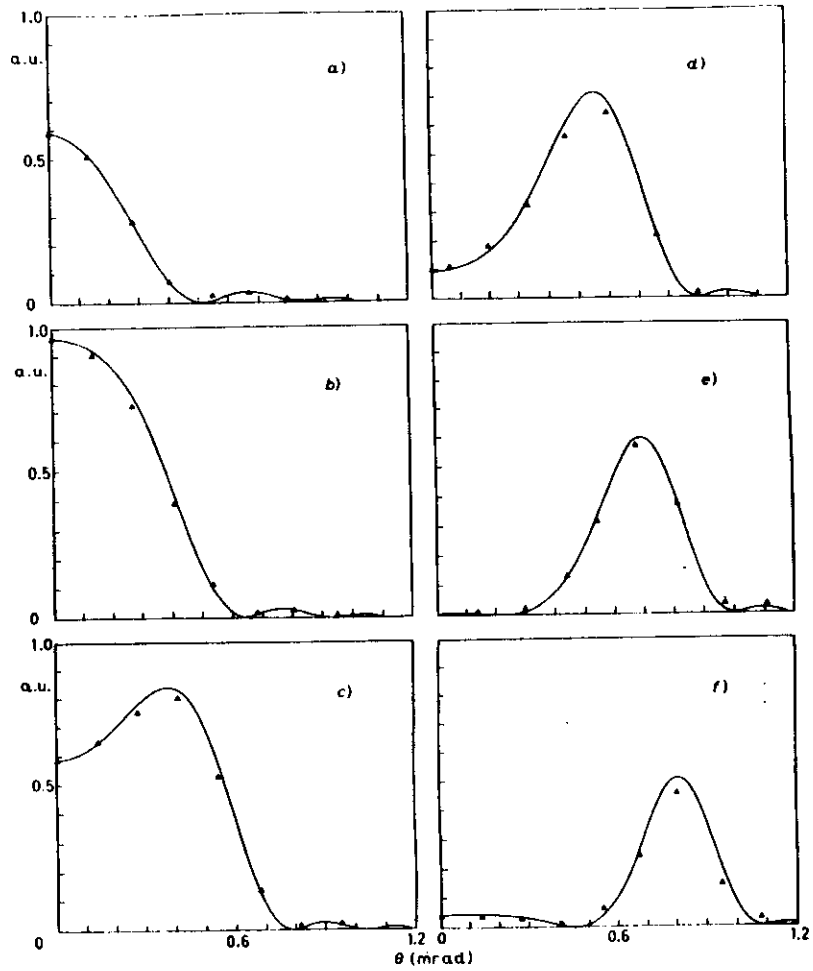

Fig. 8. – Angular distribution of the first harmonic on the horizontal plane for a beam of 620 MeV at several wave-lengths: *a*) $\lambda = 510$ nm, *b*) $\lambda = 520$ nm, *c*) $\lambda = 530$ nm, *d*) $\lambda = 540$ nm, *e*) $\lambda = 550$ nm, *f*) $\lambda = 560$ nm. Note that the pattern at 530 nm corresponds approximately to the condition of maximum gain of the undulator used as a FEL amplifier. In fact, the maximum gain is achieved at a wave-length $\lambda = \lambda_{res}(1 + 0.416/N)$, N being the number of periods and λ_{res} the central wave-length of the spontaneous radiation in the forward direction.

To reduce the noise, the signal relative to each point was integrated for 1 s. Consequently, the measurement of each harmonic lasted two hours and required the successive reinjection of the beam in the storage ring. The variation of the current in the ring was taken into account by normalizing the intensity to it. In addition, the data were taken by utilizing the ring current in the range 30 to 10 mA, that is no longer than the beam lifetime. The recorded

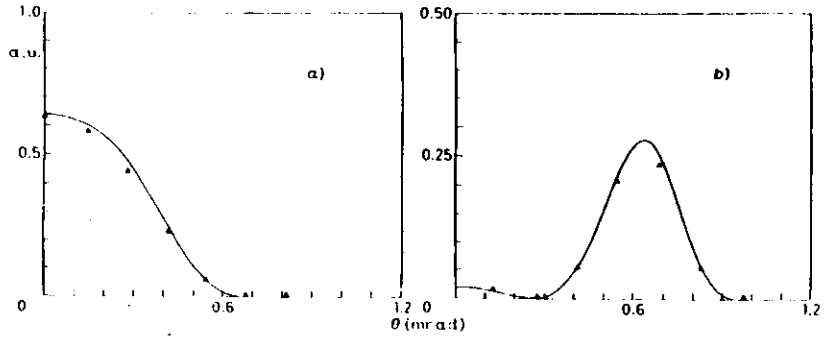

Fig. 9. – Angular distribution of the third harmonic on the horizontal plane for a beam of 358 MeV at the two wave-lengths: $\lambda = 520$ nm (a)) and $\lambda = 530$ nm (b)).

values of the intensity were divided by the transmittance curve of the apparatus and successively interpolated with a cubic spline algorythm, thus obtaining the tridimensional plots of fig. 10.

A beam energy of 620 MeV was used for the first harmonic, while the third-harmonic intensity was measured with a beam of 535 MeV, in order to obtain a frequency close to that of the fundamental one. No attempt was made for measuring the single s- and p-components of the polarization.

The axis of the radiation pattern was identified carefully by interpolating the central wave-lengths of the spectra taken on the horizontal plane with a parabola of the form $\lambda_i = A + B(i\Delta x - x_a)^2$, x_a being the axis co-ordinate in the generic reference system for the detector displacements. The same procedure was followed for the y-axis.

Eventually, the experimental points were compared with the computer-generated patterns and the relative distributions are presented in the set of diagrams of fig. 7 to 10. In particular, the half-pole contribution was calculated by using the limit form of eq. (46) for the function T and eliminating the ripples of the angular pattern due to the unphysical discontinuity of the first-order derivative of $B_\varphi(\zeta)$ implicit in the form (6) of the potential A_φ. The series of eqs. (43) and (44) included only three terms, while the operators L_1 and L_2 were truncated to the second term in consideration of the small value of L_w/R_0.

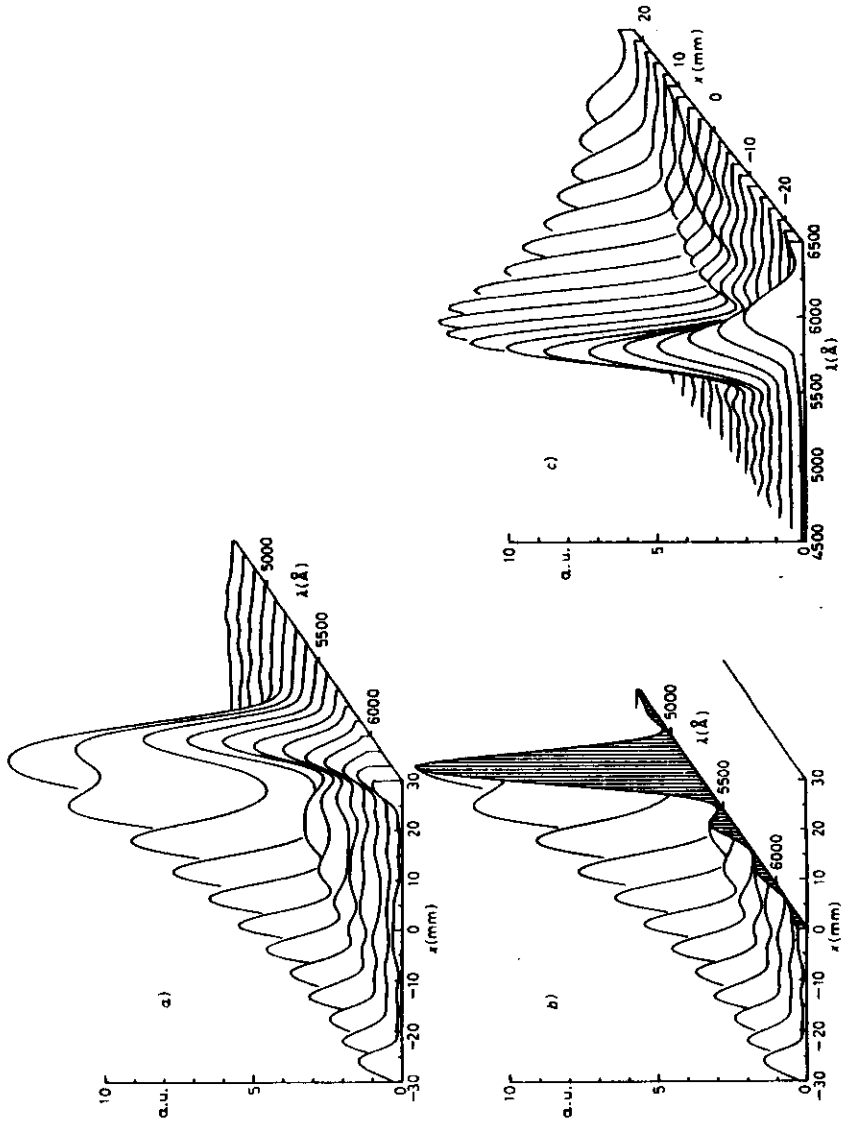

Fig. 10. – Tridimensional distribution of the measured intensity vs. the wave-length and the off-axis angle obtained by interpolating the experimental values with a cubic spline algorithm. Note that the angles are expressed by the distances of the photodetector from the axis.

7. – Conclusions.

The principal objective of the study described in this paper was to examine the mechanisms leading to a modification of the intensity radiated by the linear undulator installed on the ADONE storage ring. As a preliminary step we have considered the changes due to the variation of the distance of the observation point from the undulator. In this frame, we have introduced as a parameter the Fresnel number N_w of the undulator seen from the field point along the direction $\hat{n}$. For values of $N_w \gg 0.1$, the field must be expressed in terms of the complex Fresnel integral $F(x)$, while for $N_w \leqslant 0.1$ the more familiar sinc (x) function can be used. For what concerns the electron beam parameters, we have shown that the divergence is the main factor affecting the pattern, while minor roles are played in typical conditions by the energy spread and the beam envelope. The effect of the divergence on the average intensity is discussed analytically by capitalizing on the smallness of the pattern variation for the ADONE undulator. In this way, the spectrum on the axis, the angular pattern and the central frequency of the first harmonic as a function of the off-axis angle are expressed, respectively, as functions of the normalized divergence $\Delta \equiv \gamma^2\sigma'^2/(1 + K^2/2)$. From this analysis, we draw the conclusion that the undulator pattern is influenced by the fluctuations of the ADONE beam by no more than a few percent. This result has been confirmed by the close agreement of the measured intensity profiles with those calculated by ignoring the beam parameter fluctuations.

Finally, it should be remarked that these results have been obtained in a quite general way, so that they lend themselves to be used for linear undulators having any number of poles and field parameters K of any value.

* * *

The experimental work described in this paper was done in co-operation with the staff of the Accelerator Division of the INFN Adone Facility. Their co-operation and the guidance of S. TAZZARI are gratefully acknowledged.

Thanks are due to D. F. ALFEROV for calling our attention on the effects of the electron beam divergence on the undulator radiation, to C. MISIANO and his group of the Selenia SPA for having measured the reflectivity of the mirrors and G. PRISCO and S. DE NICOLA for the assistance in the preparation of the computer code.

APPENDIX

In view of the definition of ν, p and q reported in eqs. (30) and introducing the quantity $u \equiv \Omega 2\gamma^2/\omega(1 + K^2/2)$, we easily obtain

(A.1) $$\frac{\partial \nu}{\partial \gamma} \equiv \nu_{,\gamma} = -\frac{2}{\gamma}\frac{1}{u},$$

(A.2) $$\nu_{,\beta_{0x}} = -\frac{p}{\alpha},$$

(A.3) $$\nu_{,x} = \frac{K}{1 + K^2/2}\frac{1}{u},$$

(A.4) $$p_{,\gamma} = -\frac{2p}{\gamma},$$

(A.5) $$p_{,\beta_{0x}} = -2\gamma\frac{K}{1 + K^2/2}\frac{1}{u},$$

(A.6) $$p_{,x} = \frac{p}{K},$$

(A.7) $$q_{,\gamma} = -\frac{2q}{\gamma},$$

(A.8) $$q_{,\beta_{0x}} = 0,$$

(A.9) $$q_{,x} = \frac{2q}{K},$$

(A.10) $$Q = R_0 - 2\frac{n_{0x}}{\alpha}R_1 + I_1.$$

Next, using the identities

(A.11) $$R_{n,p} = \tfrac{1}{2}R_{n-1} - \tfrac{1}{2}R_{n+1},$$

(A.12) $$R_{n,q} = \tfrac{1}{2}R_{n+1} - \tfrac{1}{2}R_{n-1},$$

which can be easily proved by taking into account the definition of R_n given by eq. (32), we obtain

(A.13) $$2Q_{,p} = R_{-1} - 2\frac{n_{0x}}{\alpha}R_0 + 2\frac{n_{0x}}{\alpha}R_2 - R_2,$$

(A.14) $$2Q_{,q} = -R_{-2} + 2\frac{n_{0x}}{\alpha}R_{-1} - R_0 + R_2 - 2\frac{n_{0x}}{\alpha}R_3 + R_4,$$

(A.15) $$4Q_{,pp} = R_{-2} - 2\frac{n_{0x}}{\alpha}R_{-1} - R_0 + 4\frac{n_{0x}}{\alpha}R_1 - R_2 + R_4 - 2\frac{n_{0x}}{\alpha}R_3,$$

(A.16) $$4Q_{,qq} = -2\frac{n_{0x}}{\alpha}R_{-2} + R_{-2} - R_0 + 4\frac{n_{0x}}{\alpha}R_1 - R_2 + R_4 - 2\frac{n_{0x}}{\alpha}R_3,$$

(A.17) $$4Q_{,pq} = -R_{-2} + 2\frac{n_{0x}}{\alpha}R_{-2} - 2\frac{n_{0x}}{\alpha}R_0 + 2R_1 - 2\frac{n_{0x}}{\alpha}R_2 + 2\frac{n_{0x}}{\alpha}R_4 - R_3.$$

Taking into account eqs. (52)-(54) together with the above definitions, we obtain the following expressions for the coefficients of eq. (55):

$$\text{(A.18)} \qquad A_{\beta_{xx}} = -\left(\frac{4\gamma q}{K}\right)^2 (R_0 + R_2)(R_0 - R_4 + 2R_2) \qquad (= -8.45 \cdot 10^4),$$

$$\text{(A.19)} \qquad A_\gamma = -q^2(7R_0R_2 + R_0R_4 - 2R_2^2 - 5R_2R_4 - R_4^2) \qquad (= 0.324),$$

$$\text{(A.20)} \qquad A_E = -\frac{A_\gamma}{K^2} \qquad (= -0.014),$$

$$\text{(A.21)} \qquad B_{\beta_{xx}} = B_{\beta_{yy}} = 8Nq\left(\frac{\gamma}{K}\right)^2 (R_0 + R_2)^2 \qquad (= 2.8 \cdot 10^4),$$

$$\text{(A.22)} \qquad B_\gamma = \frac{N}{4q}\frac{K^2}{\gamma^2} A_\beta \qquad (= -12.6),$$

$$\text{(A.23)} \qquad B_E = \frac{1}{32}\frac{N}{\gamma^2} A_\beta \qquad (= -0.031),$$

$$\text{(A.24)} \qquad C_\gamma = 4N^2(R_0 + R_2)^2 \qquad (= 840),$$

$$\text{(A.25)} \qquad C_E = \frac{16}{K^2} N^2 q^2 (R_0 + R_2)^2 \qquad (= 30),$$

where the numbers in parenthesis represent the values relative to the ADONE undulator for $\gamma = 1300$. Note that along the axis $p = 0$, $q/4 = K^2/(1 + K^2/2) = 0.115$, while $R_0 = 0.948$, $-R_2 = R_{-2} = 0.224$, $-R_4 = R_{-4} = 0.026$, $R_{2m+1} = 0$.

● RIASSUNTO

Si espone lo studio sperimentale e teorico della radiazione emessa dall'ondulatore lineare, installato su una sezione dritta dell'anello di accumulazione ADONE. In particolare, si illustra la possibilità di esprimere il campo a distanza finita utilizzando l'integrale complesso di Fresnel. Sono inoltre presentate varie espressioni dell'intensità media in funzione della divergenza angolare del fascio e della differenza di energia fra gli elettroni. Queste formule sono utilizzate per analizzare il profilo spettrale ed angolare della radiazione, misurata ad una distanza di 20 m dell'ondulatore. L'eccellente qualità dell'ondulatore e l'influenza trascurabile che la divergenza del fascio ha sull'andamento dei parametri della radiazione sono confermate dal soddisfacente accordo fra le misure e le curve previste teoricamente.